Interaction Between Forming and Crashworthiness of Advanced High Strength Steel S-Rails

by

Rassin Grantab

A thesis
presented to the University of Waterloo
in fulfilment of the
thesis requirement for the degree of
Master of Applied Science
in
Mechanical Engineering

Waterloo, Ontario, Canada, 2006

I hereby declare that I am the sole author of this thesis. This is a true copy of the thesis, including any required final revisions, as accepted by my examiners.

I understand that my thesis may be made electronically available to the public.

ABSTRACT

This thesis presents the results of experimental and numerical investigations carried out to assess the effects of tube bending and hydroforming on the crash performance of s-rail structures manufactured from three different advanced high strength steels, namely DDQ, HSLA350, and DP600. The main impetus for this project is to reduce vehicle weight through material substitution and, in order to do so, the effects of material strength on crashworthiness, as well as the interaction between forming processes and crash response must be well understood. To this end, in the current research, s-rails were fabricated through tube bending and hydroforming experiments conducted on DDQ, HSLA350, and DP600 steels with a nominal wall thickness of 1.8mm, as well as HSLA350 steel with a nominal wall thickness of 1.5mm. Impact experiments were subsequently performed on non-hydroformed and hydroformed s-rails to examine the effects of the forming processes and material substitution on the crushing loads and levels of absorbed energy. All forming and crash experiments were simulated using numerical finite element methods which provide additional insight into various aspects of the crash response of these structures. In particular, crash simulations were used to show the effects of work-hardening, material thickness changes, and residual stresses incurred during the forming operations.

The numerical tube bending simulations accurately predict the results of the tube bending and hydroforming processes for all materials, particularly for the DP600; the predictions for the DDQ material are the least accurate. Both simulations and experiments show that material thinning occurs on the tensile side of the bend, and material thickening on the compressive side of the bend; the level of thickness change is unaffected by material strength or initial material thickness. The low-pressure hydroforming process does not greatly affect the thickness and strain distributions of s-rails.

The crash simulations provide predictions that are in excellent accord with the measured results, with a maximum error of ±10% in the peak loads and energies; simulations of DP600 s-rails are the most accurate, while simulations of DDQ s-rails are the least accurate. Through simulations and experiments, it is shown that material thickness has the greatest effect on the crash performance of s-rail structures, while material strength plays a secondary role. A 20% increase in the wall thickness of HSLA350 s-rails amounts to a 47% increase in energy absorption. Substituting HSLA350 and DP600 steels in place of DDQ steel leads to increases in energy absorption of 31% and 64%, respectively, for corresponding increases in strength of 30% and 76%. Neglecting material strain-rate effects in the numerical models lowers the predicted peak loads and energies by roughly 15%. By performing a numerical parametric study, it is determined that a weight reduction of 22% is possible by substituting thinner-gauge DP600 s-rails in place of DDQ s-rails while maintaining the energy absorption of the structures.

ACKNOWLEDGEMENTS

I would like to thank my supervisor, Prof. Michael J. Worswick, for providing me with the opportunity to work on this project, for his guidance throughout the entire process, as well as important discussions regarding single malts. This research project was made possible through collaboration with General Motors of Canada and Dofasco. I would like to thank Dr. Robert Mayer of General Motors for conducting the crash tests presented in this thesis and for many helpful discussions. I would also like to thank Isadora van Riemsdijk and Bruce Farrand of Dofasco for their help during the course of this project. I would also like to thank Tycos Tool and Die for providing the hydroforming die used in my experiments.

I am indebted to Ekhard Budziarack, Howard Barker, and Richard Gordon for their tireless help in the lab over the past two years. I would also like to thank Dino Oliveira and Bruce Williams for their substantial assistance with the tube bending and hydroforming experiments. Many thanks to my office-mates José, Alex, and Rafal (when he was still around) for maintaining a cheerful and sane working environment. Thanks to Dino for all his help on the project and for venting sessions. Thanks to Alan Thompson for providing the high-strain rate data, and for numerous non-work-related discussions that lighten the mood when frustration levels are high. Thanks to Hari for his continual help in a number of different areas pertinent to this thesis, as well as his incessant imparting of ‘wisdom’ regarding all facets of life. Thanks to Chris and Blake for computer and Dyna related help, and an additional thank you to Blake for showing me that I don’t have to do work *everyday*. Thanks to Mikhail for sharing music, to Oleg for valuable gym discussions, to Sooky for providing a female perspective on matters in an otherwise all-male office group, and last but not least, to the departed ‘Godfather’, Javad.

Outside the University, I must thank my family and friends, without your support I would have had a much tougher time during the past two years. Thanks in particular to my parents, who were always proud and supportive even when it was unmerited, and to my sister for being supportive and listening to numerous incoherent rants. Lastly, I would like to thank all of my friends for providing the outlet for me to get my mind completely off work; in particular, thanks to Nubs, Asselin, KGB, Nik, Pouz, and Quinlan.

To my family

TABLE OF CONTENTS

LIST OF FIGURES

LIST OF TABLES

Chapter 1

Introduction

The motivation towards vehicle weight reduction within the automotive sector has created a need for the replacement of mild steels with thinner gauge high strength steels and lightweight aluminum alloys. The impetus for weight reduction is to boost vehicle performance, and most importantly, to increase fuel economy and lower greenhouse gases; it has been reported that a 15% reduction of the weight of all vehicles in North America and Europe is equivalent to a savings of 800 million liters of fuel annually (Mohanty *et al.*, 2004). A substitution towards thinner gauge high strength steels presents several challenges. The first challenge involves structural stiffness; since the modulus of elasticity is essentially a constant, provisions are necessary to ensure adequate structural stiffness of the components made from thinner gauge materials (Schneider *et al.*, 2004). The formability and weldability of these new materials are additional challenges that must also be addressed. The final challenge is to ensure that the crashworthiness of automobiles is not degraded as a result of the substitution (Schneider *et al.*, 2004, Oliveira *et al.*, 2006). In order to overcome the latter obstacle, extensive research into the manufacturing processes involved in fabricating crush structures and their effects on the crashworthiness of the structures is imperative.

The two main types of energy absorption structures used on automobiles are so-called s-rail and axial crush structures. The s-rail structure represents the part of the frame that sweeps over the front wheels, and in some cases the s-rail refers to a side rail of the frame, as shown in Figure 1a (Asnafi, 2003). Figure 1b shows the idealized s-rail structure that is investigated in this research project. In a

crash event, s-rails undergo a bending collapse mode of failure by forming three plastic hinges. Axial crush structures are straight sections of the automotive frame that are designed to collapse through an accordion-like folding pattern of the structure's side walls. Typically, axial crush structures are welded or incorporated within the front of s-rail structures. In addition, there are often other supports attached to the s-rail on an automotive frame that also affect its energy absorption characteristics. In the current research, s-rail structures are treated in isolation in order to gain a better understanding of the effects of manufacturing processes on crashworthiness without involving other variables.

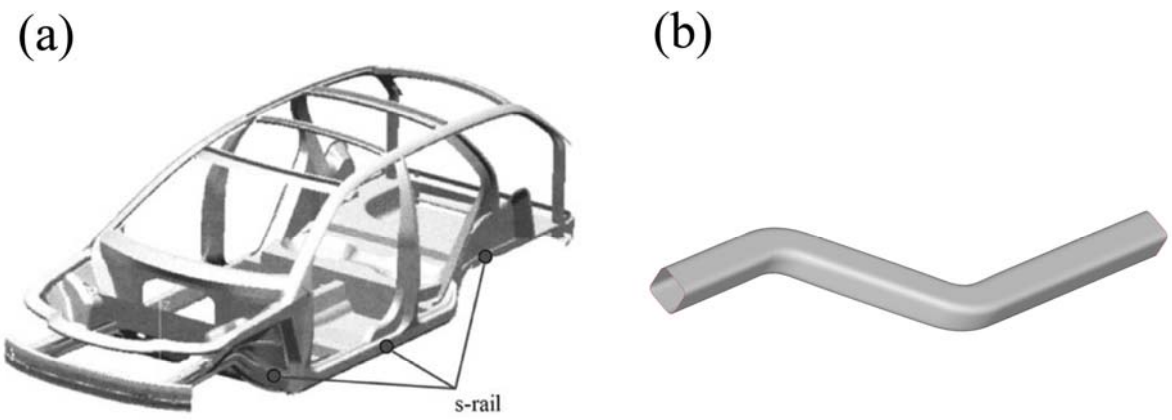

Figure 1: (a) S-Rails in automotive frames (Asnafi, 2003) (b) Idealized s-rail structure

Tube bending and hydroforming are the main manufacturing processes that are used to create s-rail structures. In the past, s-rails have been manufactured by welding two or more stamped sheet metal components together (Ahmetoglu *et al.*, 2000). Although this method provides parts with the correct sectional properties, there is a considerable amount of extra material that is needed to create areas (such as flanges) for welding; this, in addition to the weld metal itself, increases the weight of the structures. Tube hydroforming allows the forming of closed-sections, thereby eliminating the need for extra material and additional welding operations (Ahmetoglu *et al.*, 2000). This not only reduces the weight of the vehicle, but also reduces manufacturing costs since fewer operations are needed to create a component. The major drawbacks of hydroforming are the slow cycle times and the high capital cost of the tooling (Ahmetoglu *et al.*, 2000).

Due to the complex shapes of automotive structural components such as s-rails, pre-forming operations such as tube bending are often needed. Mandrel rotary-draw tube bending is the most commonly used of all pre-forming bending processes due to its accuracy and repeatability (Asnafi *et*

al., 2003). A typical structural part such as an s-rail consists of two or more bends that are created on a mandrel rotary-draw tube bender prior to hydroforming.

This research project aims to study the effects of the manufacturing processes used to fabricate high strength steel s-rails on their subsequent crash properties. Three different steels with a wide range of strength are considered, and an experimental approach is adopted in which s-rails are bent using a mandrel rotary-draw tube bender, hydroformed, and then exposed to a crash scenario. In addition to experiments, extensive numerical models of the tube bending, hydroforming, and crash events are developed in order to gain a better understanding of the relationship between forming and crashworthiness.

A review of the basic principles and available literature on tube bending, hydroforming, and crash are presented in the remainder of this chapter. The majority of the literature review focuses on crashworthiness, with special emphasis on s-rail structures, the use of high strength steels in automotive crash structures, and the effects of forming on crashworthiness.

1.1 Tube bending

Mandrel rotary-draw tube bending utilizes five major tools, as shown in Figure 2. At the start of the bend, the bend die, clamp die, pressure die, and mandrel are parallel to the tube. The wiper die is positioned with a small angle relative to the tube that minimizes frictional drag while preventing wrinkling; an excessively large wiper angle can reduce its efficacy in preventing wrinkling. The mandrel fits inside the tube and prevents the cross-section of the tube from ovalizing and collapsing during bending. Most mandrels incorporate one or more balls attached to a solid cylindrical post via flexible links (Figure 2 shows a two-ball mandrel). The wiper die is lubricated in order to further reduce friction, while the clamp die, pressure die and bend die are kept dry in order to maximize friction and minimize slip during bending. The inside surface of the tube is lubricated via holes in the mandrel in order to reduce friction with the mandrel during bending, which in turn reduces the torque required to complete the bend.

The bending process begins by closing the clamp die, which presses the tube tightly against the clamp and bend dies and allows the tube to be pulled around the bend die during the bend. Next, the pressure die is closed under load control and maintains a constant load perpendicular to the axis of the tube (referred to as the pressure die clamp load) for the duration of the bend. The pressure die clamp load is reacted by the wiper die and mandrel that serve to eliminate wrinkling on the inside region of the tube, which undergoes compression during bending. Once the appropriate clamping loads have been applied, the bend die and clamp die rotate simultaneously about the central axis of the bend die

and bend the tube. The pressure die is synchronized to translate by a distance that is equal to the arc-length of the bend, and apply a force parallel to the tube (referred to as the pressure die feed load). This pushes material into the bend and assists in completing the bend by supplying additional torque (since the load is applied with an offset from the central axis of the bend die). In some cases, the pressure die translates a distance that is different from the arc length of the bend, and a so-called 'bending boost' is applied (Bardelcik *et al.*, 2005a). When the pressure die displacement is smaller than the arc length of the bend, a negative or tensile boost load is applied, and when the pressure die displacement is greater than the arc length of the bend, a positive or compressive boost load is applied (Bardelcik *et al.*, 2005a). The mandrel remains stationary throughout the bend, however, often times it is beneficial to retract the mandrel backwards (to the right in Figure 2) near the end of the bend in order to flatten any small wrinkles that may have formed during the operation. The force required to maintain the position of the mandrel during bending is referred to as the mandrel load. The directions of the tooling loads are summarized in Figure 2. For a more thorough description of the mandrel rotary-draw tube bending process, refer to Dyment (2004).

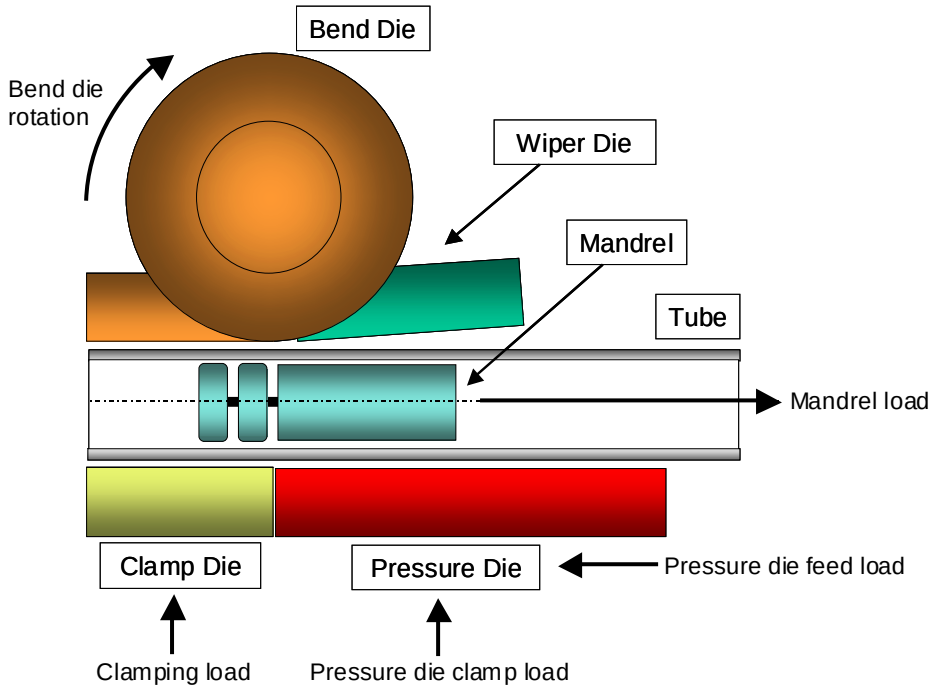

Figure 2: Schematic of the tools used in mandrel-rotary draw tube bending along with the directions of tooling loads (Oliveira, 2006a)

The radius of the bend is quantified by specifying the center-line-radius (CLR), which is the linear distance from the rotation axis of the bend die to the centerline of the tube (Dyment, 2004). The

bend severity is usually characterized in terms of the R/D ratio, where R is the CLR and D is the outer diameter of the tube.

1.1.1 Work hardening in tube bending

In order to quantify the level of plastic strain and work hardening after tube bending, Dyment *et al.* (2003), Gholipour *et al.* (2004), and Oliveira *et al.* (2006) have performed strain measurements on steel and aluminum tubes after mandrel rotary draw bending at three different R/D ratios. All these researchers found that the axial strains in bent tubes increase with decreasing R/D ratios. The hoop strains, however, were not observed to vary appreciably with changes in R/D ratio. Thickness measurements were also performed and they observed that decreased R/D ratio led to increased thinning on the outside of the bend and increased material thickening on the inside of the bend. Inoue *et al.* (1979) performed similar experiments on stainless steel tubes after radial-draw bending and came to similar conclusions.

The effects of boost on the strains and thickness distributions of bent steel tubes have been investigated by Dyment *et al.* (2003) and Bardelcik *et al.* (2005a). They studied three levels of boost displacement – 95%, 100%, and 103% of the bend arc length – and found that increasing levels of boost reduced the degree of thinning, decreased the tensile strains on the outside of the bend and increased the compressive strains on the inside of the bend.

1.1.2 Lubrication in tube bending

Oliveira *et al.* (2005) performed a study of the effects of lubricant on the bending of DQAK steel and AlMg3.5Mn aluminum alloy tubes. They used three different lubricants (the lubricants were applied to the mandrel and wiper prior to each bend) for bending DQAK and four different lubricants for bending AlMg3.5Mn. For the steel tubes, the solid film lubricant increased the torque and mandrel load due to the reduced clearance between the mandrel and tube. HydroDraw 615 was the superior lubricant for bending steel, however, when used for bending aluminum it performed poorly. Drawsol Al20 and the solid film AL 070 lubricants were found to be the best lubricants for bending the AlMg3.5Mn aluminum alloy.

Inoue *et al.* (1979) performed radial draw bending of stainless steel tubes using three different lubricants. They observed that mandrel loads could be reduced by as much as 40% by changing the lubricant. The reported mandrel loads were over five times higher when lubrication was not used at all. Improving the lubrication conditions reduced the amount of tube wall thinning by almost 20%.

1.1.3 Process variables during bending

Several researchers have monitored the loads on the tooling during bending. Inoue *et al.* (1979) monitored the torque and mandrel load during radial-draw bending of stainless steel tubes. Both types of loads were used as a measure of assessing the efficacy of a lubricant during bending.

Dwyer *et al.* (2002), Dyment *et al.* (2003), and Oliveira *et al.* (2005, 2006) have used an instrumented mandrel rotary-draw tube bender to monitor load and displacement of the tools during bending. The process variables were observed to be sensitive to R/D ratio, pressure die clamp load, lubrication conditions, tube thickness, and tube material.

1.1.4 Numerical and analytical modeling of tube bending

A great deal of research has been performed on the subject of numerical modeling of the tube bending process by the following researchers: Welo *et al.* (1994), Paulsen *et al.* (1996), Wu *et al.* (1996), Yang *et al.* (2001), Dwyer *et al.* (2002), Trana (2002), Zhan *et al.* (2002), Dyment *et al.* (2003), Gao *et al.* (2004), Gantner *et al.* (2004), Gholipour *et al.* (2004), Bardelcik *et al.* (2005a, 2005b), and Oliveira *et al.* (2006). In all cases, finite element simulations were used to predict the final part shape, thickness and strain distributions. Most of these researchers have validated their finite element models by comparing their predictions to experimental measurements of strain, thickness, and process variables.

Normani (2004) developed an analytical model that can predict the thickness, strain, and stress distributions resulting from tube bending operations. This model was useful due to its efficiency, since predictions could be obtained in minutes as opposed to finite element models that require hours to complete the same calculation; however, the predicted results were not as accurate as corresponding finite element models.

Al-Qureshi (1999) has developed a theoretical analysis of tube bending focusing mostly on quantifying springback. The theory agrees well with experimental results based on aluminum and stainless steel tubes. He also derives expressions for bending loads that are also in good agreement with experiments. Tang (2000) performed a plastic deformation analysis of tube bending and presented equations to predict thickness, circumferential shrinking, neutral axis deviation, and bending torque.

1.2 Hydroforming

A typical tubular hydroforming process sequence is shown in Figure 3 (Dohmann *et al.*, 2004). The process begins with the insertion of the tube between the two die halves (Figure 3a). The dies are

then closed and the seals are inserted at the two ends of the tube to contain the internal pressure during hydroforming (Figure 3b). The tube is internally pressurized to force the material to conform to the die surface (Figure 3c). During pressurization, axial loads (denoted as F_a) are applied at the ends of the tube to increase formability (Dohmann *et al.*, 2004; Bardelcik *et al.*, 2005b). High pressures, ranging from 207 MPa (30 000 psi) up to 1 034 MPa (150 000 psi), are required to fully form small radii in a hydroformed part (Koç *et al.*, 2001).

Some of the most common applications of tube hydroforming are seen in the automotive industry; parts such as roof pillars, frame rails, engine cradles, rear axles, and exhaust manifolds are widely manufactured using tube hydroforming techniques (Ahmetoglu *et al.*, 2000; Koç *et al.*, 2001). Non-automotive applications include T-connections for plumbing applications, faucets, and parts for the aerospace industry (Dohmann *et al.*, 1997). In comparison to traditional stamped and welded parts, tube hydroforming offers several advantages such as: part consolidation (instead of welding two or more parts together, a single part can be made through hydroforming); weight reduction through efficient section design; lower tooling and manufacturing costs due to a reduction in the number of parts; tight dimensional tolerances and minimal springback; reduced scrap (Ahmetoglu *et al.*, 2000).

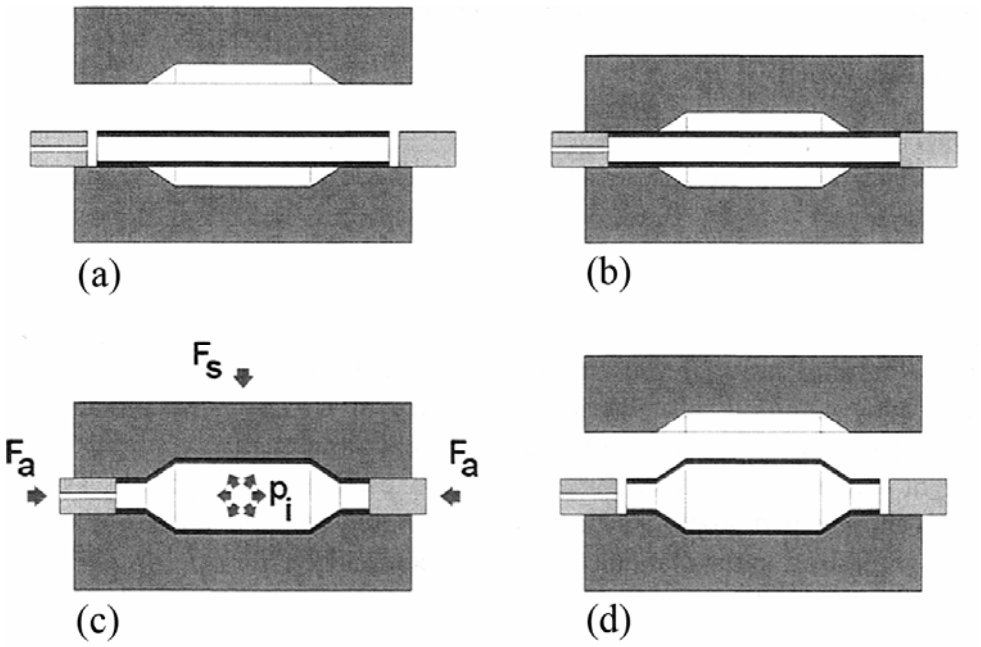

Figure 3: Schematic of the hydroforming process (a) Insertion of the tube (b) Die closure (c) Hydroforming and endfeeding (d) Removal of the part (Dohmann *et al.*, 2004)

1.2.1 Low-pressure hydroforming

Traditional tubular hydroforming processes require high internal pressures to circumferentially expand the tube material to fill the die cavity; this is generally referred to as high-pressure hydroforming (shown in Figure 3). Low-pressure, or pressure-sequence hydroforming, is a method of hydroforming wherein the tube is partially formed during die closure, and then fully formed by using substantially lower pressures (roughly 10% of the maximum pressures used in high-pressure hydroforming) (Morphy, 2001; Singh, 2003). A schematic of the low-pressure hydroforming process is shown in Figure 4 (Morphy, 2001). The perimeter of the die cavity is designed to be nearly the same as the perimeter of the tube prior to hydroforming (Figure 4a). During die closure, the tube wall is forced into the corners of the die cavity while a low fluid pressure is maintained inside the tube to prevent the section from collapsing while it is being crush-formed (Figure 4b). Once the dies are fully closed, the internal pressure is increased to fully form small radii in the part (Figure 4c). This second stage of pressurization is often referred to as the calibration phase, and pressures at this stage rarely exceed 83 MPa (12 000 psi) (Ahmetoglu *et al.*, 2000; Morphy, 2001).

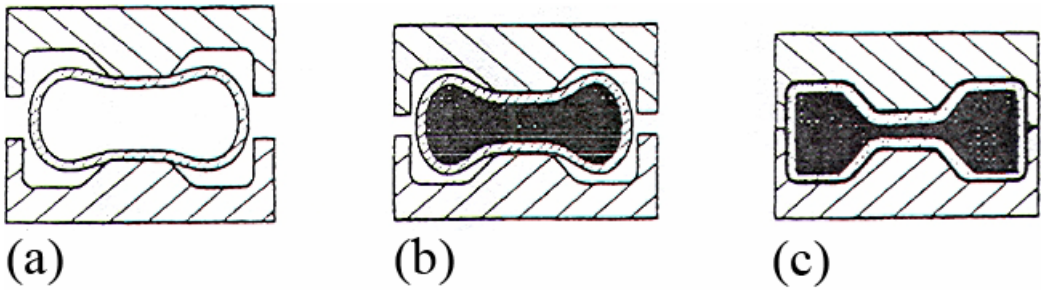

Figure 4: Schematic of the low-pressure hydroforming process (a) Before pressurization (die open) (b) First pressurization stage (die closure) (c) Calibration phase (die closed) (Morphy, 2001)

In contrast to high-pressure hydroforming processes that place the material in a tensile state of deformation, low-pressure hydroforming deforms the material in circumferential bending, thereby drastically reducing the degree of material thinning. The resulting tube wall thickness varies by only 3 – 5% using low-pressure hydroforming, as opposed to a 15 – 20% variation when using high-pressure hydroforming (Dohmann, 1997). Since tube deformation occurs mostly under bending, this process is very attractive for hydroforming low-formability materials such as high strength steels (Morphy, 2001).

1.2.2 Effects of tube bending on hydroforming

Nearly all complex hydroformed parts require a tube bending operation prior to hydroforming. Tube bending often strains the material to a greater degree than the subsequent hydroforming operation, therefore much of the material's ductility is exhausted during tube bending (Dwyer *et al.*, 2002). Consequently, in order to maximize material formability during hydroforming, the relationship between the tube bending and hydroforming operations must be clearly understood.

Asnafi *et al.* (2003) and Yang *et al.* (2001) have observed that rotary draw bending was the best method for pre-bending tubes prior to hydroforming. Through the use of finite element simulations of the bending and hydroforming processes, Trana (2002) found a substantial improvement in the hydroformability of pre-bent tubes when using a four-ball mandrel as opposed to a cylindrical mandrel (a ball-less mandrel).

Several researchers (Wu *et al.*, 1996; Dwyer *et al.*, 2002; Dyment *et al.*, 2003; Dyment, 2004; Gao *et al.*, 2004) have investigated the effects of bending and hydroforming through numerical simulations. Gao *et al.* (2004) and Dyment (2004) observed that larger bend radii in the bending process resulted in reduced material thinning and strain levels, which lead to improved formability during the subsequent hydroforming operation. Positive boost during tube bending has been shown to decrease material thinning (Wu *et al.*, 1996; Dyment *et al.*, 2003; Dyment, 2004; Bardelcik, 2005a) thereby increasing the formability of pre-bent tubes during hydroforming.

Finite element simulations of the tube bending and hydroforming processes have been conducted using different failure criteria in order to predict the onset of necking during hydroforming. A damage-based constitutive softening model was implemented in LS-Dyna by Gholipour *et al.* (2004) to predict failure of pre-bent aluminum alloy tubes; the predicted failure locations were in close agreement with experiments.

The application of a strain-based forming limit diagram (FLD) towards failure prediction during hydroforming of pre-bent tubes is not appropriate since the strain paths in tube bending and hydroforming are drastically different (Dwyer *et al.*, 2002; Trana 2002). Stoughton (2000) has proposed a two-dimensional stress-based FLD that can be used in favor of strain-based FLDs when analyzing problems with non-linear strain paths. Simha *et al.* (2005) have extrapolated this idea to a three-dimensional extended stress-based forming limit curve (XSFLC), and applied the problem to predicting failure during hydroforming of pre-bent DP600 steel tubes. The predicted necking pressures were within 10% of the experimental burst pressures, and the predicted failure locations were in excellent agreement with experiments. Bardelcik *et al.* (2005b) have applied the XSFLC to predicting failure during hydroforming of DP600 steel tubes with endfeed. The analysis closely predicted the

necking pressure for the case without endfeed, however, the accuracy of the predictions diminished when endfeed was applied during the hydroforming process.

1.2.3 Material characterization for hydroforming simulations

In order to simulate the tube bending and hydroforming processes using FEM, accurate tube material properties are required. The most common method of determining material properties is by performing tensile tests on flat specimens cut from sheet metal before it is rolled into a tube; however, the material properties change due to work hardening during the tube rolling process (Ahmetoglu, 2000). Consequently, it is imperative that the material properties used in tube bending and hydroforming simulations are derived from the tube itself, and not from the sheet that was used to fabricate the tube. Bardelcik *et al.* (2005b) and Oliveira *et al.* (2006) have circumvented this problem by performing tensile tests on specimens cut from the longitudinal direction of the tubes used in the bending and hydroforming experiments.

Kulukuru *et al.* (2002) have proposed a different approach; they argue that since hydroforming exposes the material to a biaxial stress state, a uniaxial tensile test cannot provide accurate material models. Their approach utilizes a hydraulic tube bulge test that places the material in a biaxial stress state that reflects the hydroforming process.

Levy *et al.* (2004) present yet another method of determining the tube material properties. They studied two types of steel, AKDQ and HSLA, and developed equations to calculate the effective strains due to the tubing process. Given the tubing strains and the average material properties of the virgin sheet, their approach can be used to determine the longitudinal tube material properties.

1.3 Structural crashworthiness

Automotive crash structures are designed as to function as sacrificial entities during a crash. The main goal of engineers is to develop crash structures that absorb impact energy while keeping the passenger compartment intact, and the deceleration loads experienced by the occupants below certain particular levels. In addition to this impact performance criteria, new environmental demands have forced the automotive industry to design lighter, more fuel efficient vehicles, thus creating an additional requirement criterion to minimize the weight of crash structures. The ability of engineers to accurately predict the crash performance of automotive structures is paramount when designing lighter automobiles (Jones, 1998). Prior to the advent of powerful computers and numerical methods, analytical methods were the only means by which a design engineer could predict the performance of

crash structures. With advances in computer and FEM technology, engineers now have additional tools to improve their predictive capabilities.

The following presents a review of some seminal research in the field of crashworthiness. Although most of the research efforts in the past have been committed to axial structures, more research is now being performed on bending collapse of structures, as well as the use of high strength steels for crashworthiness applications.

1.3.1 Axial crush structures

The first studies on the dynamic inelastic response of structures were conducted by Lee *et al.* (1952) by using a rigid-plastic approximation to analyze beams under transverse impact. This approach was first utilized to develop analytical models of axial crushing of thin-walled structures by Alexander (1960), and more elaborate analytical schemes were later derived by Wierzbicki *et al.* (1983). Abramowicz *et al.* (1984) compared theoretical predictions with dynamic drop tower experiments considering thin-walled square steel tubes and found a reasonable level of agreement. More recently, Jones (2003) has investigated the dynamic plastic buckling of cylindrical shells and square tubes. Jones (2003) claims that these new analyses are crucial for accurate predictions at high impact velocities. Other studies on the crushing of thin-walled structures have been conducted by Abramowicz (2003) who uses a kinematic approach to describe crushing mechanics.

1.3.2 Bending of box section columns

Analytical analysis methods similar to those used in the study of axial crushing have been applied to investigate the crushing mechanics of box section columns under bending. One of the earliest efforts in this field was a study performed by Kecman (1983). By examining kinematic continuity conditions at the folds, equations were developed for energy absorption assuming that all of the energy is absorbed by plastic deformation. The theory matched experimental quasi-static results quite well. Kecman (1983) states that the proposed theory can predict bending response under quasi-static as well as dynamic conditions; if a dynamic analysis is desired, high strain rate material properties must be used in place of quasi-static material data. A similar study was performed by Brown *et al.* (1983) using thick-walled theory predictions.

Kim *et al.* (2000) investigated deep biaxial bending collapse of thin-walled sections using numerical and analytical methods. Square and rectangular section beams were subjected to cantilever bending with rotations up to 40°. Results were generated using FEM and compared to analytical

predictions; this comparison showed close agreement between the results, thereby validating the analytical model.

Kim *et al.* (2001a) examined the crushing response of thin-walled prismatic columns under combined compression and bending. They developed an analytical model for this crushing condition by using a non-linear spring to model the plastic hinge. They compared their analytical predictions to FEM predictions and found close agreement.

1.3.3 S-Rail structures

The logical progression of prior research on axial crushing and bending of box columns is the study of bending collapse in s-rail structures. Prior to the prominence of sophisticated FEM codes, Ni (1976) used a numerical approach in implementing a lumped-mass model for predicting the impact response of aluminum and steel s-rails. An empirical formula was used to relate the changes of crush distance and bending angle to the cross-sectional changes of the s-rail within the plastic hinge regions. The strain hardening and high strain rate material properties were accounted for in the model, and comparisons with experiments showed excellent agreement.

Abe *et al.* (1990) have used the method of plastic hinges in an elastic-plastic analysis to predict the quasi-static crushing response of welded top-hat section steel s-rails. The s-rails had different section sizes (ranging in width from 50 to 70 mm), different bend angles (ranging from 15° to 45°), and different thicknesses (ranging from 0.8 to 1.4 mm). The analytical model was shown to match the experiments closely.

The analytical model presented by Abe *et al.* (1990) considered two-dimensional s-rails (the two bends of the s-rail are in the same plane); Kim *et al.* (2004) have developed an analytical quasi-static crushing model for three-dimensional s-rails, which are more representative of an actual automotive structure, and compared their predictions with those obtained from FEM analyses. In this study, four different cross-sectional aspect ratios (1.0, 1.3, 1.4, 2.0) and two thicknesses (1.6mm and 2.4mm) were considered, along with a material model similar in strength to a typical 5XXX aluminum alloy. It was shown that for a square section s-rail (aspect ratio equal to unity), the peak load during crushing is roughly 1.7 times higher for the 2.4 mm wall thickness s-rail as opposed to the 1.6 mm wall thickness s-rail. The analytical predictions were nearly identical to the FEM solutions.

Kim *et al.* (2001b) have also performed analytical and numerical studies on the effect of cross-sectional shape on the crash performance of welded hat-section steel s-rails. They investigated 21 different cross-sectional designs, most with internal stiffening members; foam filling was also used as one of the variations. Two of the designs were found to increase specific energy absorption (SEA, calculated by dividing the absorbed energy by the weight of the structure) drastically: A design with a

diagonally positioned internal stiffener and suitable triggering dents absorbed roughly 200% more energy than the baseline double hat cross-section, and SEA increased by a factor of 3 times; By using foam filling, SEA increased by 2.84 times.

The analytical s-rail crushing model proposed by Kim *et al.* (2004) has been used by Zheng *et al.* (2004) to predict the crushing response of aluminum s-rails for comparison to experiment. Two aluminum s-rails were bent from roll-formed AA5754 aluminum alloy tube and crushed quasi-statically. In addition to the experiment and the analytical model, an FEM analysis was also performed. The analytical model matched the experimental results very closely, while the FEM model underpredicted the crushing loads by as much as 27%, however, there are two caveats to this result. Firstly, the test fixture used during crushing deformed in bending since it was not stiff enough to tolerate the large bending moments generated by the crushing of the s-rails; the analytical models, however, did not take this matter into consideration. Secondly, the analytical and FEM predictions did not consider the forming history (strains, stresses, and material thickness changes) of the s-rail; neglecting the forming history of s-rails can decrease the predicted crushing loads by as much as 30% under dynamic impact, as shown by Oliveira *et al.* (2006). The numerical impact simulations performed by Oliveira *et al.* (2006) showed excellent agreement with experiments since they included the forming history of the s-rails in the simulations. The validity of the analytical solution presented by Kim *et al.* (2004) for predicting the dynamic response of s-rails has been refuted by Oliveira *et al.* (2006), who have shown that the analytical solution overpredicts the experimentally measured forces by as much as 28%.

Reid (1996a, 1996b) performed FEM crush simulations of a midrail from a General Motors vehicle and parametrically varied the strength of the material used in the rail, as well as the thickness of the sheet metal. He started with a baseline HSLA350 steel with a thickness of 1.5 mm. The thickness was varied parametrically from –30% to +30% in 10% increments, and the stress-strain curve was varied from –30% to +10% by multiplying all the stress values in the curve by the appropriate scaling factor. The first conclusion of the study was that for a given thickness, a 10% change in stress-strain response results in a 7% change in energy absorption. The second conclusion was that for a given material, a 10% change in thickness results in a 14% change in energy absorption. Oliveira *et al.* (2006) found a three-fold increase in energy absorption when increasing the wall thickness of aluminum s-rails from 2.0 mm to 3.5 mm. These results indicate that Reid's (1996a, 1996b) conclusions are either geometry dependent (since Reid used an actual automotive part, as opposed to the idealized s-rail used by Oliveira *et al.*), material dependent, or they do not apply beyond the ±30% thickness range used in the study.

1.3.4 Application of high strength steels to crash structures

As part of an Ultra-Light Steel Auto Body (ULSAB) project, a consortium of 35 steel companies around the world collaborated to create an automobile body that was 25% lighter, 80% stiffer in torsion, and 52% stiffer in bending than the baseline model by the extensive introduction of advanced high-strength steels (AHSS) into the body structure. The weight reduction was achieved through the use of dual-phase (DP) and transformation-induced plasticity (TRIP) steels for about 90% of the body-in-white, along with laser-welded blanks and various hydroforming techniques (Mohanty *et al.*, 2004).

During their initial development stages in the 1970s, DP steels contained roughly 20% hard martensite within a ductile ferrite matrix; current DP steels contain martensite and bainite phases alongside ferrite in various concentrations (Mohanty *et al.*, 2004). The microstructure of TRIP steels contains 10-30% retained austenite that can undergo a martensitic transformation upon subsequent deformation, such as during press-forming or a crash event. This transformation induces a volume change that leads to improved ductility (Samek *et al.*, 2004).

Sperle *et al.* (1984) have investigated the application of DP steels – with ultimate tensile strengths of 600, 800, and 1000 MPa, and thicknesses ranging from 0.7 to 1.5 mm – to square-section axial crush members; axial members made of mild steel were also tested as a baseline material. For the same wall thickness (hence equal mass), comparisons with mild steel showed that energy absorption increased by 41%, 64% and 82% for the DP600, 800, and 1000 alloys, respectively. By reducing the thickness of the higher strength steels and maintaining the same level of energy absorption as the mild steel axial member, the weight of the structures was reduced by 21%, 28%, and 33% for the DP600, 800, and 1000 alloys, respectively.

Axial crush members made from DP steels have also been studied by Tarigopula *et al.* (2006). The study involved experimental and numerical investigations on quasi-static and dynamic crushing of square-section and top-hat section axial tubes made of DP 800 steel. Three different impact velocities were used for the dynamic tests (5, 10, and 15 m/s), and the peak and mean loads recorded from the experiments were found to increase with impact velocity. A large difference was observed between quasi-static and dynamic tests, which was attributed to strain-rate sensitivity and inertia effects. The simulations showed that as the impact velocity increased, inertia effects dominated the force-displacement response, while strain-rate effects dominated the low velocity impacts. FEM models accounting for the high-rate properties of the steel provided predictions that matched the experimental results quite well. A parametric study varying the wall thickness and material yield strength of the tubes

was performed numerically; the energy absorption increased linearly with yield strength, which is consistent with theory, and mass-specific energy absorption increased with sheet thickness.

Peixinho *et al.* (2003) conducted experiments with top-hat section and hexagonal-section axial tubes made from DP600 and TRIP 600 steels. Numerical models accounting for the high-rate material properties of the two steels predicted deformations and load versus time curves that matched experiments very well. A similar experimental and numerical investigation of axial crushing of square-section TRIP steel tubes was performed by Huh *et al.* (2002).

Geoffroy *et al.* (1993) have experimentally examined the difference in the static and dynamic crush response of axial members made from mild steel (AKDQ), high-strength low-alloy steel (HSLA), and DP steel. The highest energy absorption was realized by using the DP steel, followed by the HSLA steel. A similar experimental study was performed by Schneider *et al.* (2004) using HSLA steel, high-strength interstitial-free steel (IFHS), and a mild steel. The axial members made from HSLA steel exhibited the greatest energy absorption and average crushing load (referred to as mean crush load), followed by the IFHS steel tubes. Hsu *et al.* (2004) have experimentally investigated the quasi-static and dynamic axial crush response of stainless steel, mild steel, and aluminum alloy circular tubes. The stainless steel tubes exhibited the highest energy absorption, while the aluminum tubes displayed the lowest energy absorption.

The previously mentioned studies investigated the effects of high-strength steels on the impact response of axial crush members only. Li *et al.* (2003) and Zhang *et al.* (2006) have performed full vehicle crash simulations of automobiles with several structural parts made from high-strength steels and found that the overall energy absorption could be maintained while reducing total vehicle mass by as much as 22 kg. Huh *et al.* (2003) numerically investigated the side-impact response of a vehicle with side members made from TRIP steel and observed that side-impact energy absorption increased without any increase in overall vehicle mass.

1.3.5 Effects of forming on crashworthiness

The importance of the effects of forming operations on the crash response of automotive structures has been studied by several researchers (Kaufman *et al.*, 1998; Kellicut *et al.*, 1999; Williams *et al.*, 2005; Oliveira *et al.*, 2006). Kellicut *et al.* (1999) and Dutton *et al.* (1999) have developed numerical bending and hydroforming models to include forming results into crash simulations. In order to isolate the effects of material thickness changes, as well as forming stresses and strains on the crash response of an s-rail, six different crash simulations were performed with the following forming considerations: 1) no forming history 2) thickness changes only 3) pre-springback residual stresses only 4) post-springback residual stresses only 5) plastic strains only 6) all forming histories. Simulations

incorporating considerations 1 through 4 resulted in similar predictions, around 380 mm of crush displacement. Incorporating considerations 5 and 6, however, greatly affected the simulation results; the predicted crush displacement for these two cases was roughly 210 mm. This indicates that plastic strains and the associated work hardening due to forming have a much greater effect on the crash response of hydroformed s-rails than the forming stresses and thickness changes.

Oliveira *et al.* (2006) studied the effects of tube bending on the subsequent crash response of AA5754 aluminum alloy s-rails through experiments and numerical simulations. S-rails were bent at two different R/D ratios (refer to Section 1.1), and the s-rails bent at an R/D of 2.5 exhibited slightly higher peak loads during impact when compared to the s-rails bent at an R/D of 2.0. Oliveira *et al.* (2006) used an approach similar to Kellicut *et al.* (1999) and Dutton *et al.* (1999) in order gain insight into the magnitude of error that arises from neglecting forming histories in impact simulations and observed that peak load predictions were 25-30% lower, and energy absorption was 18% lower when forming histories were not considered.

The effects of hydroforming on the subsequent crashworthiness of aluminum alloy axial crush tubes has been studied theoretically by Mayer (2004), and numerically by Williams *et al.* (2005). Mayer (2004) found that the mean crush loads predicted by theoretical calculations were as much as 25% lower if forming effects were not considered. Williams *et al.* (2005) simulated the high-pressure and low-pressure hydroforming processes, and carried the resulting strains, stresses, and material thickness values forward to the crash simulations. The numerical crash predictions revealed that mean crush loads decrease as the corner radius of the hydroformed axial crush structure is reduced.

Ryou *et al.* (2005) have developed a technique for incorporating forming stresses and strains into impact simulations by using an ideal forming solution and a hybrid membrane/shell method. The technique consists of calculating mid surface solutions for shell elements using the ideal forming code, then generating through-thickness stresses and strains using the hybrid membrane/shell method; these stresses were then transferred to the FEM crash models. For comparison purposes, full forming simulations were also performed using FEM. These methods were applied to crash simulations of stamped I-rails (axial members) and stamped s-rails, and the crash simulation results showed that the maximum deceleration values (and consequently the crash loads) were larger when the sheet forming histories were included for both geometries. The predictions from the hybrid membrane/shell technique were quite similar to those obtained from full FEM forming simulations, however, computation times were drastically reduced by using their proposed method.

1.3.6 High strain rate material characterization

Numerous researches have noted the importance of including high-rate material properties in crash simulations of steel structures (Geoffroy *et al.*, 1993; Langrand *et al.* 1999; Huh *et al.*, 2002; Peixinho *et al.*, 2003; Shkolnikov, 2004; Tarigopula *et al.*, 2006). Huh *et al.* (2002) quantified the significance of high-rate properties by observing that predictions from axial crush simulations incorporating high-rate material properties matched experiments closely, while simulations that neglected these properties under-predicted energy absorption by 20-40%.

The most widely accepted method for testing materials under high-strain rates is the so-called Hopkinson (or Kolsky) bar; interested parties are referred to Meyers (1994) for detailed information on this test method. Results from Hopkinson bar tests can be curve-fit to several different constitutive equations, the two most common being the Johnson-Cook (Johnson *et al.*, 1983) and Zerilli-Armstrong (Zerilli *et al.*, 1987) models. Two other high-rate constitutive equations are the Cowper-Symonds (Cowper *et al.*, 1957) and the Moudlin-Davidson-Henninger (Moudlin *et al.*, 1990) models, although they are less widely used.

1.3.7 Present research

The literature review presented hitherto has uncovered a great deal of research in the application of AHSS within automotive crash structures, however, all of the studies have either dealt with axial structures or full vehicle analyses; researchers have not examined the application of HSLA and DP steels to s-rail structures. The two major goals of this research project are to study the effects material substitution through the use of DDQ (a type of mild steel), HSLA350, and DP600 steels in s-rail structures, and to investigate the effects of the tube bending and hydroforming operations on the crash response of AHSS s-rails. Another aim of this research project is to develop numerical models that can accurately model the forming processes and crash scenarios to which the s-rails are subjected in experiments. This is assessed through meticulous model validation based on forming process variables, forming-induced strains, material thickness changes, and energy absorption response during impact.

The present research is part of a large collaborative project between the University of Waterloo, General Motors of Canada, and Dofasco, in which the application of high strength steels to s-rail and axial crush structures is examined, along with high-strain rate testing of the alloys considered. The focus of this thesis is the effect of material substitution and forming processes on s-rail structures.

The following chapters present detailed descriptions of all aspects of the current project. Chapters 2 and 3 outline the experimental and numerical methods, respectively, while Chapters 4 and 5

present the experimental and numerical results, respectively. A discussion of the results is given in Chapter 6, and conclusions and recommendations for future work are provided in Chapter 7.

Chapter 2

Experimental methods and procedures

This chapter outlines the equipment, processes and procedures utilized for the experimental portion of this research project. All s-rails were fabricated from 76.2 mm (3 inch) outer diameter induction seam-welded steel tubes. Three different high-strength steels were examined in this project: DDQ, a draw-quality mild steel with yield and tensile strengths of roughly 260 and 350 MPa, respectively; HSLA350, a high-strength low-alloy steel with yield and tensile strengths of roughly 400 and 460 MPa, respectively; and DP600, a dual-phase steel with yield and tensile strengths of roughly 500 and 630 MPa, respectively. Detailed quasi-static and high-rate material data for all of the alloys is presented in Chapter 3. The DP600 and the two gauges of HSLA350 steel are cold-rolled and Galvannealed materials, whereas the DDQ steel is hot-rolled without any galvanizing treatments.

Table 1 shows a detailed forming and impact-testing plan outlining the different materials, geometries, thicknesses, and bend radii examined. For each of the three materials, s-rails were bent to different R/D ratios (refer to Section 1.1), and both hydroformed and non-hydroformed s-rails were impacted in order to gain insight into the effects of hydroforming on crashworthiness. A tube wall thickness of 1.5 mm was considered in addition to the 1.8 mm wall thickness for the HSLA350 steel only. For each case (with the exception of two cases), four s-rails were fabricated for impact testing along with extra s-rails for setup purposes (the extra s-rails have not been documented). Four additional HSLA350 1.8mm s-rails were bent at an R/D ratio of 1.5 in preparation for two ancillary crash tests conducted at higher impact velocities in order to observe the effects of impact velocity on the crash response of s-rails.

The s-rails examined in this project consist of two 45° bends as shown in Figure 5. The s-rails are divided into five distinct sections, labeled A through E in Figure 5. The dimensions of sections A, C, and E change with different R/D ratio as documented in Table 2 (dimensions in millimeters), however, the overall length and axial offset remain constant at 976.2 and 250 mm, respectively, for all R/D ratios. The cross-sectional outer dimensions of the hydroformed s-rails are shown in Figure 6 (dimensions in millimeters). The outer perimeter of the hydroformed section is virtually equal to the outer circumference of the original tube in order to eliminate any circumferential expansion during the low-pressure hydroforming operation. All s-rail dimensions were chosen to reflect those of an actual part in a small-sized automobile.

Table 1: Testing plan

Material	Hydroformed or Non-Hydroformed	Thickness (mm)	R/D	# of s-rails	Impact velocity (m/s)
DDQ	NH	1.8	2.0	4	4.57
	H	1.8	2.0	4	4.57
	H	1.8	1.5	4	4.57
HSLA350	NH	1.5	2.0	4	4.57
	H	1.5	2.0	4	4.57
	NH	1.8	2.0	4	4.57
	NH	1.8	1.5	4	4.57
	NH	1.8	1.5	2	6.46
	H	1.8	2.0	4	4.57
	H	1.8	1.5	4	4.57
	H	1.8	1.5	2	8.06
DP600	NH	1.8	2.5	4	4.57
	NH	1.8	2.0	4	4.57
	NH	1.8	1.5	4	4.57
	H	1.8	2.5	4	4.57
	H	1.8	2.0	4	4.57
	H	1.8	1.5	4	4.57

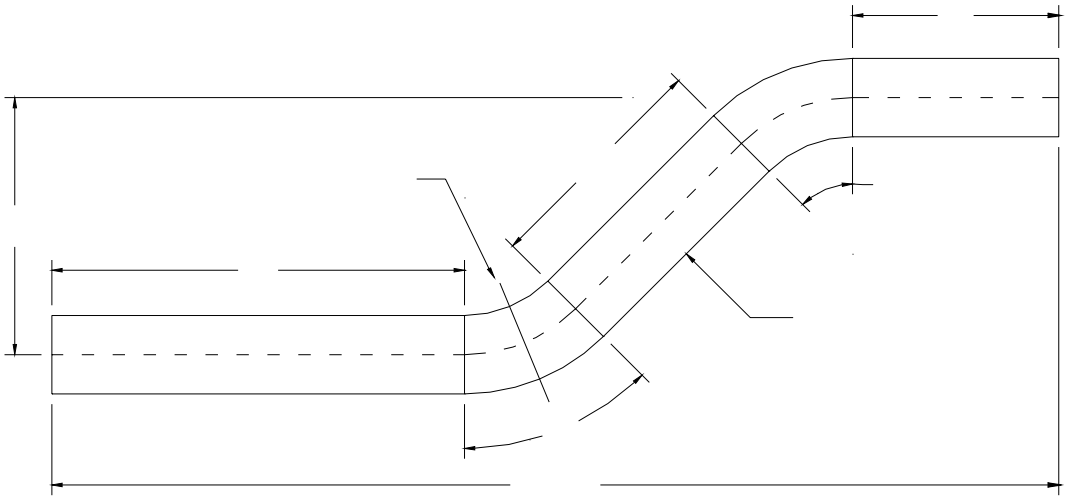

Figure 5: Schematic of s-rail structure (units in millimetres)

Table 2: S-Rail dimensions (units in millimetres)

	Sections		
R/D ratio	**A**	**C**	**E**
1.5 (CLR = 114.3)	415.8	258.9	215.8
2.0 (CLR = 152.4)	400.0	227.3	200.0
2.5 (CLR = 190.5)	384.2	195.7	184.2

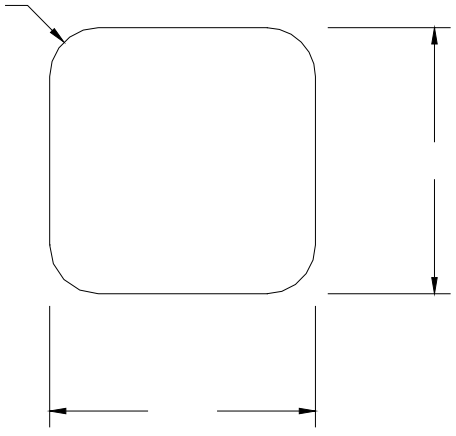

Figure 6: Cross-sectional outer dimensions of hydroformed s-rail (units in millimetres)

2.1 Tube bending experiments

The tube bending experiments were performed on an Eagle Precision Technologies EPT-75 mandrel rotary-draw tube bender, shown in Figure 7. This particular tube bender has been fully instrumented, with load-cells monitoring the pressure die clamp load, pressure die feed load, mandrel load, and bend die torque; provisions have also been added to the bender to monitor the pressure die clamp displacement, pressure die feed displacement, mandrel displacement, and bend die rotation angle. A Labview-based software program is used to control data acquisition and to provide program signal inputs to servo-hydraulic controllers. The software communicates with a digital-to-analog output card to generate control signals to PID controllers that send the signals to servo-hydraulic actuators on the tube bender in a closed loop manner. Displacement and load sensors on the tube bender tooling provide process data that is input to an analog-to-digital converter and fed to the computer software for running the closed loop control system, and for data collection purposes. The pressure die clamp is operated under load control, while the pressure die feed, bend die rotation, and mandrel position are operated under displacement control. Dyment (2004) provides more detailed information on the tube bender.

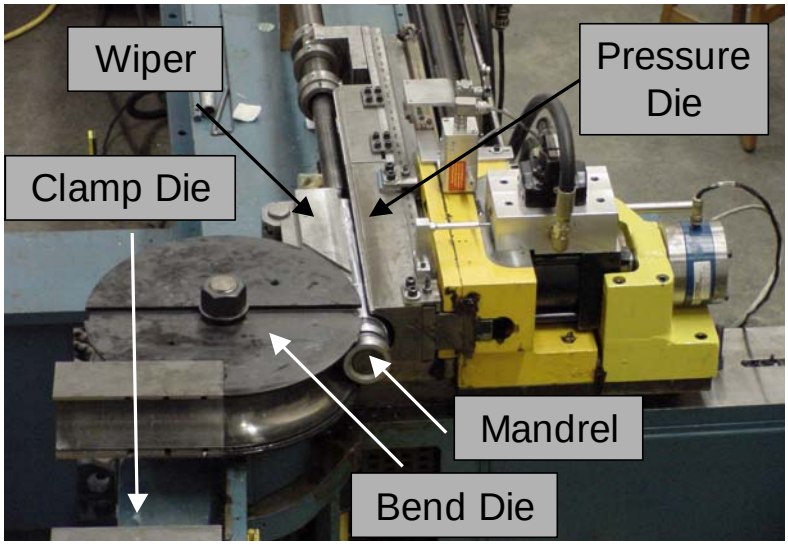

Figure 7: Eagle EPT-75 mandrel rotary-draw tube bender

Each tube was placed over the mandrel with the weld seem positioned vertically so it would lie on the neutral axis of the bend; this ensures that the weld properties have minimal effect during the bending process. D.A. Stuart Hydrodraw 615 lubricant was applied to the inside of the tube via the mandrel, and applied to the wiper die prior to each bend as outlined by Oliveira *et al.* (2005); the tube

was then bent, as described in Section 1.1. Upon completion of the first bend, the tube was advanced by the distance corresponding to the length of section C of the s-rail (refer to Table 2), and rotated by 180° about the mandrel; at this point, the tube was in position to commence the second bend. Once the second bend had been completed, the s-rail was trimmed to the proper length using a cut-off saw.

2.1.1 Process parameters

The process parameters for the DDQ, HSLA350 (1.5 and 1.8 mm wall thicknesses), and DP600 steels under the different bend conditions are shown in Table 3, Table 4, and Table 5, respectively. An attempt was made to apply the same pressure die clamp load for all the bending cases, however, under a 65 kN pressure die clamp load, the DP600 tubes could not be bent to an R/D ratio of 1.5 without wrinkling, and a load of 75 kN was used instead. The HSLA350 tubes with a wall thickness of 1.5 mm also wrinkled under a pressure die clamp load of 65 kN, therefore a load of 75 kN was applied for this case as well. The listed wiper angles were set through trial and error in order to obtain wrinkle-free bends. All bends were completed over a 4 second span.

Table 3: Bending process parameters for DDQ steel

	R/D ratio	
Process parameter	**1.5 (CLR = 114.3)**	**2.0 (CLR = 152.4)**
Actual bend die radius (mm)	113.7	150.4
Prescribed bend angle (°)	45.5	45.3
Pressure die clamp load (kN)	65.0	65.0
Wiper angle (°)	0.5	0.5
Mandrel post radius (mm)	35.75	35.75
Mandrel ball radius (mm)	35.79	35.79

Table 4: Bending process parameters for HSLA350 steel

	1.5 mm wall thickness	**1.8 mm wall thickness**	
Process parameter	**R/D = 2.0 (CLR = 152.4)**	**R/D = 1.5 (CLR = 114.3)**	**R/D = 2.0 (CLR = 152.4)**
Actual bend die radius (mm)	150.4	113.7	150.4
Prescribed bend angle (°)	46.2	46.3	45.5
Pressure die clamp load (kN)	75.0	65.0	65.0
Wiper angle (°)	0.5	0.4	0.5
Mandrel post radius (mm)	36.28	35.75	35.75
Mandrel ball radius (mm)	36.18	35.79	35.79

Table 5: Bending process parameters for DP600 steel

Process parameter	R/D ratio		
	1.5 (CLR = 114.3)	**2.0 (CLR = 152.4)**	**2.5 (CLR = 190.5)**
Actual bend die radius (mm)	113.7	150.4	188.6
Prescribed bend angle (°)	46.7	46.6	46.6
Pressure die clamp load (kN)	75.0	65.0	65.0
Wiper angle (°)	0.3	0.5	0.6
Mandrel post radius (mm)	35.75	35.75	35.75
Mandrel ball radius (mm)	35.79	35.79	35.79

All tubes were bent to an angle slightly larger than 45° in order to compensate for angular springback after the bend. In addition to angular springback, there is a degree of radial springback (Dyment, 2004), and in order to obtain the correct post-bending center-line radii, the three bend dies were radially smaller than the desired final dimensions. The exact bend angles, as well as the actual center-line radii of the three bend dies, are listed in Table 3 through Table 5. As a general trend, the angular springback increases with decreasing R/D ratio for a given material. The amount of springback also increases with the strength of the tube since higher stresses will be induced in the material for a given strain level, resulting in a greater degree of elastic springback.

All tube bending experiments utilized a mandrel with two balls; the outer radii of the mandrel balls and posts are listed in Table 3 through Table 5. For each of the bends, the mandrel was retracted 55 mm once the bend angle reached 42° in order to create a smooth bend by flattening any of the bumps caused by the material stretching over the mandrel balls during bending.

The DP600 tubes proved exceedingly difficult to bend due to their high-strength, and the torque capacity of the tube bender was exhausted for the R/D ratio of 1.5. The only viable solution was to reduce the amount of sliding between the pressure die and the tube during bending in order to increase the pressure die feed load; since the pressure die is offset from the rotation axis of the bend die, any increase in the pressure die feed load will create additional torque to bend the tube. In order to increase the coefficient of friction between the pressure die and tube, pine tar powder was applied to the pressure die prior to every bend for the DP600 tubes at R/D ratios of 1.5 and 2.5. Measurements taken at the tail ends of the tubes indicated a reduction in slip from an average of 13 mm for unassisted friction, to an average of only 3 mm by using the pine tar. Despite the difficulty in doing so, bending of the DP600 tubes at an R/D ratio of 2.0 was performed without the use of pine tar in order to allow comparison of the process variables for all the different steels at that R/D ratio, since using pine tar increases the pressure die feed load, and decreases the bend die torque as a result. Pine tar was used for

bending at an R/D ratio of 2.5 in order to allow comparison of process variables between the R/D ratio of 1.5 and 2.5 for the DP600 steel.

2.1.2 Sample preparation and measurements

In preparation for bending, tubes were cut to a length of 1.5 m and de-burred. Roughly one-quarter of the tubes were electrochemically etched with circle grids of 2.54 mm (0.1 in) diameter for post-forming strain measurements, as described by Dyment (2004). In addition to the strain measurements, thickness measurements were conducted using an ultrasonic thickness measurement probe. The strain and thickness measurements were conducted along the lower path of the s-rail and around the circumference of section B (the first bend) of the s-rail, as shown in Figure 5; the circumferential measurement was conducted halfway (at the 22.5° location) along the first bend. Measurements along the upper path of the s-rail and around the circumference of section D (the second bend) have been shown to be redundant by Oliveira *et al.* (2006), since no difference was observed between the first and second bends of the s-rail. Two s-rails were measured for each condition listed in Table 1 after bending and after hydroforming; measurements were conducted along the lower path and around the circumference after bending, and only around the circumference after hydroforming.

2.2 Hydroforming experiments

The hydroforming die-set used to fabricate the s-rails is shown in Figure 8; the die-set was donated courtesy of Tycos Tool and Die. In order to hydroform tubes with different R/D ratios without manufacturing three different dies, a single die body was used with three sets of inserts for the bend regions; Figure 8a shows an exploded view of the inserts and the die body. The die had a square cross-section corresponding to the final desired cross-section of the hydroformed s-rail shown in Figure 6. The ends of the die had 100 mm long circular sections in order to accommodate the endseals; a 50 mm long region provided a gradual transition from the square section to the circular section. Mating and alignment of the upper and lower dies was achieved through the use of four bosses at the corners of the bottom die (Figure 8a); the bosses also serve to react the lateral loads during hydroforming.

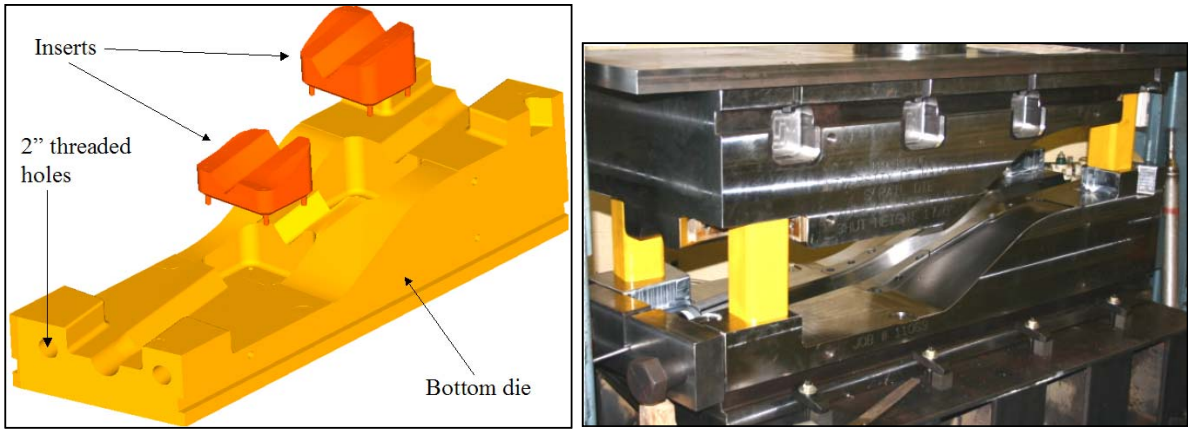

Figure 8: S-Rail hydroforming dies (a) Exploded drawing of the bottom die body with inserts (b) Upper and lower dies positioned in the press

The hydroforming experiments were conducted on a Macrodyne 1000-tonne hydroforming press that is shown in Figure 9. A Labview-based computer-manipulated control system functioning in a similar manner to the one used for the tube bender was used to lower and raise the press in synchronization with the tube’s internal pressure. Pressurized water was fed to the tube using a high-pressure intensifier, while the pressure was contained using Parker Polypak elastomer endseals shown in Figure 10. The endseals were inserted at both ends of the tube prior to hydroforming, with one endseal being capped while the other was connected to the pressure intensifier. The pressure acting on the endseals was reacted by 50 mm thick (2 inch) plates bolted to both ends of the bottom s-rail die via 50 mm bolts, as shown in Figure 8b.

Figure 9: Macrodyne 1000-tonne hydroforming press (note that the picture does not show the s-rail die in the press)

The tubes were trimmed to the correct length (the lengths specified in Table 2 plus an extra 150 mm on each end to accommodate the endseals) and coated with D.A. Stuart Hydrodraw 625 solid film lubricant prior to hydroforming. With the endseals inserted in the tube and connected to the pressure intensifier, the upper die was lowered until contact was made with the tube, at which point the tube was completely filled with water; a schematic of this starting position is shown in Figure 11a. During die closure, water must flow out of the tube under control, since a change from a circular cross-section induces a reduction in volume, and would result in a large increase in the pressure due to the high bulk modulus of water. As a result, the control system continually bled water from the tube during die closure in order to maintain an internal pressure below 6.89 MPa (1000 psi); if this pressure was exceeded, the motion of the upper die was halted until the pressure reduced to 4.48 MPa (650 psi), at which point die closure resumed. Once the dies were fully closed, the internal pressure of the tube was increased above 68.9 MPa (10 000 psi) in order to calibrate the tube, as shown schematically in Figure 11b. The hydroformed s-rails were trimmed to the lengths specified in Table 2.

Figure 10: Parker Polypak endseals

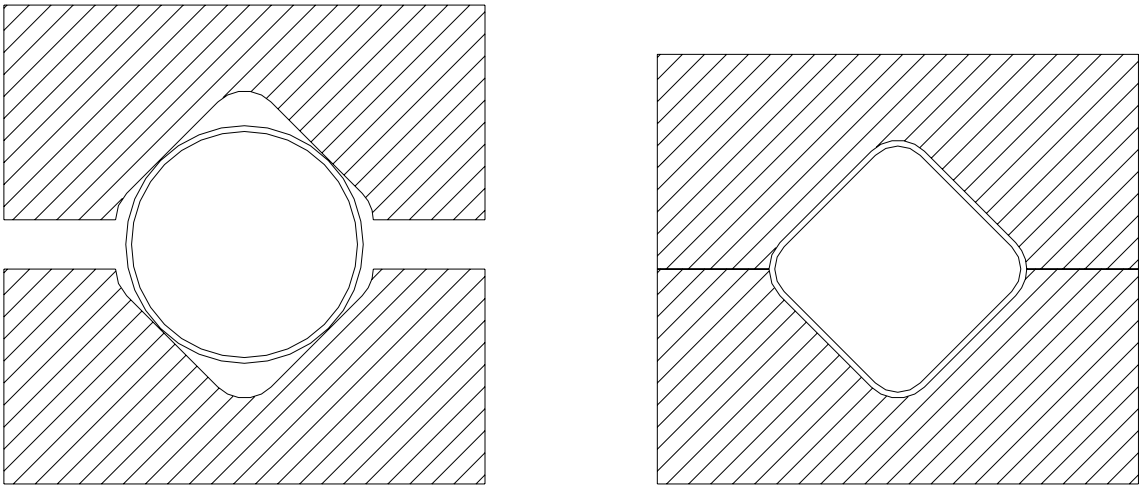

Figure 11: Schematic of low-pressure hydroforming (a) Starting position for hydroforming (b) Final position during calibration

2.2.1 Process parameters

The calibration pressures used for the DDQ, HSLA350, and DP600 steel tubes are shown in Table 6. Upon closure of the dies, the internal pressure was increased linearly from the range of die closure pressure to the calibration pressure over a period of 90 seconds. The calibration pressure of 93.08 MPa represents the maximum allowable pressure due to constraints on the hydraulic system of the press.

Table 6: Hydroforming calibration pressures

Material	Die closure pressure (MPa)	Calibration pressure (MPa)
DDQ	2.07 - 6.89	68.95
HSLA350 1.5 mm	2.07 - 6.89	89.63
HSLA350 1.8 mm	2.07 - 6.89	89.63
DP600	2.07 - 6.89	93.08

2.3 Crash experiments

The impact experiments were performed on a deceleration sled test at the GM Technical Center in Warren Michigan. Two s-rails were mounted in an opposing fashion in the horizontal plane and tested simultaneously, as shown in the schematic of the test setup in Figure 12 (Mayer, 2006). The s-rails were mounted on steel plates at both ends using solid steel internal bosses and external clamps with a height of 50.8 mm (2 inches); the clamps and bosses for the non-hydroformed and hydroformed s-rails are shown in Figure 13. The clamps were grooved on the clamping surface in order to minimize the slip of the tube over the bosses. The bosses and clamps shown in Figure 13 were mounted to the impacted plate. In order to eliminate steel-on-steel impact, thus minimizing the ringing in the system, a layer of plywood and rubber was placed on the impacted plate. Four 100 kN load cells were placed at the base of each s-rail in order to record the load during impact. A hydraulic ‘snubber’ covered with an aluminum honey-comb material (referred to as Hexcel) was implemented to contact the moving sled after 250 mm of crush displacement (a typical degree of crushing during automotive crash scenarios) and fully halt its motion; additional Hexcel stoppers were mounted on both sides of the s-rails in the event that the ‘snubber’ could not fully stop the moving sled.

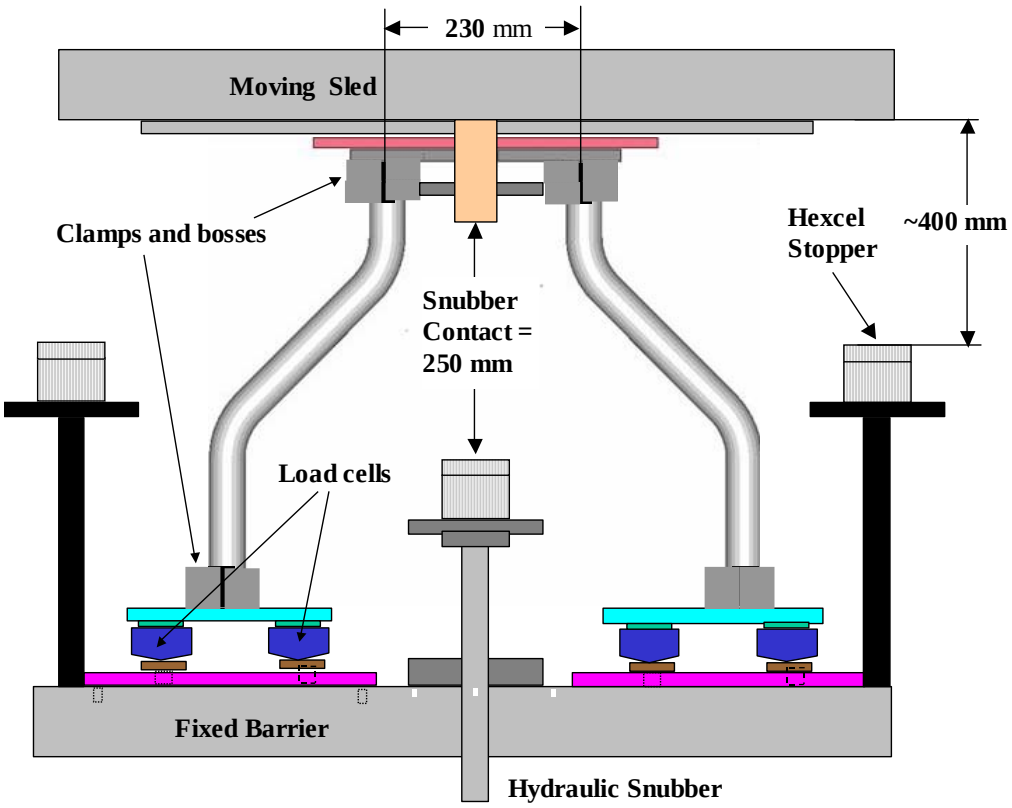

Figure 12: Schematic of impact test setup (Mayer, 2006a)

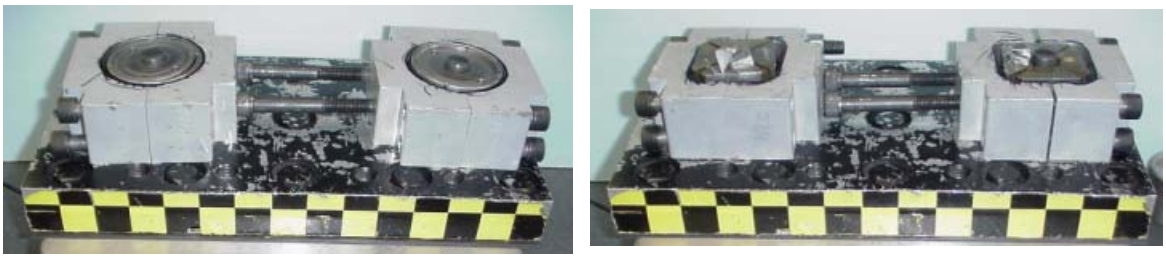

Figure 13: Clamps and bosses for (a) non-hydroformed s-rails (b) hydroformed s-rails (Mayer, 2006) (impacted end shown)

2.3.1 Impact parameters

All impact experiments (except for two test) were performed by accelerating the sled to a velocity of 4.57 m/s using compressed gas. The impact velocity was determined through numerical simulations such that the desired level of deformation could be achieved for s-rails made from all three materials. The two high-velocity tests were performed at impact velocities of 6.46 and 8.06 m/s (refer to Table 1). The sled mass was 1145.0 kg for all tests, while the impacted plate mass was 14.4 and 13.8 kg for the non-hydroformed and hydroformed s-rails, respectively.

Chapter 3

Numerical simulations

Finite element simulations of the tube bending, hydroforming, and crash scenarios presented in Table 1 were performed using the dynamic-explicit code LS-Dyna version 970 (Hallquist, 2003). Seven separate analyses were performed for each case in order to carry over stress, strain, and thickness results from one analysis to another. The sequence of analyses was as follows: First bend; Implicit springback; Second bend; Implicit springback; Hydroforming; Implicit springback; Crash. This chapter outlines the procedures used for the numerical analyses. For an overview of the LS-Dyna code, the reader is referred to Hallquist (2003).

3.1 Material characterization

Quasi-static material properties for the three different steels were assigned to the tubes in the numerical forming models using a power law curve-fit of the following form:

$$\sigma = K\bar{\varepsilon}^{p^n} \qquad (1)$$

where σ is the flow stress, K is the strength coefficient, $\bar{\varepsilon}^{p}$ is the effective plastic strain, and n is the hardening exponent.

High-rate material properties derived from tensile split-Hopkinson bar testing performed by Thompson (2006) were assigned to the three different tube materials in the numerical crash models using a Johnson-Cook equation (Johnson *et al.*, 1983) of the following form:

$$\sigma = (A + B\bar{\varepsilon}^{p^n})(1 + c\ln(\dot{\varepsilon}^*))(1 - T^{*m}) \quad (2)$$

where A, B, n, c, and m are experimentally derived constants. $\dot{\varepsilon}^*$ is a dimensionless strain rate of the form:

$$\dot{\varepsilon}^* = \frac{\dot{\bar{\varepsilon}}^p}{\dot{\varepsilon}_o} \quad (3)$$

where $\dot{\bar{\varepsilon}}^p$ is the effective plastic strain rate, and $\dot{\varepsilon}_o$ is the reference strain rate (1 strain/second for all of the data presented in this thesis). The homologous temperature is defined as:

$$T^* = \frac{T - T_{room}}{T_{melt} - T_{room}} \quad (4)$$

where T is the current temperature of the material, T_{room} is the room temperature, and T_{melt} is the melting temperature of the steel.

The first term in parentheses in Equation 2 represents the flow stress of the material at the reference strain rate; Simha (2006) has developed a modified Johnson-Cook constitutive equation by replacing the power-law-type hardening behavior contained in the first set of parentheses by a Voce-type hardening model (Voce, 1948), resulting in the following constitutive equation:

$$\sigma = \left[A + (B - A)(1 - e^{-n\bar{\varepsilon}^p}) \right](1 + c\ln(\dot{\varepsilon}^*))(1 - T^{*m}) \quad (5)$$

where A, B, n, c, and m are experimentally derived constants (A, B, and n differ from the terms in Equation 2). The modified Johnson-Cook constitutive equation was developed in order to rectify the problem of continual increase of flow stress with increasing plastic strain when curve-fitting stress-strain data to a power-law equation. By using the modified Johnson-Cook equation, the flow stress saturates at the value of the constant 'B' when the material is deformed at the reference strain rate and temperature.

In addition to the two different Johnson-Cook constitutive equations, the data derived from tensile split-Hopkinson bar testing was also fit to a Zerilli-Armstrong (Zerilli *et al.*, 1987) constitutive equation of the following form:

$$\sigma = C_1 + C_2 e^{(-C_3 + C_4 \ln(\dot{\varepsilon}^*))T} + C_5 \bar{\varepsilon}^{p^n} + C_6 \quad (6)$$

where C_1, C_2, C_3, C_4, C_5, C_6, and n are experimentally derived constants.

The rolling operations used to manufacture a tube induce varying levels of work hardening around the circumference of the tube, hence there exists a variation in the strength of the as-received tube around its circumference. In order to account for this variation in strength, samples were cut from the 3 o'clock, 6 o'clock, and 9 o'clock locations around the circumference of the tubes, as shown in Figure 14, and tested in uniaxial tension. The arithmetic mean of the stress-strain response from the

three locations was curve-fit to a power-law model (within a range of 5 to 20% strain) and used in the numerical simulations. A similar procedure was performed by Thompson (2006) for obtaining average tube material properties under high rates of strain. It should be noted that the HSLA350 1.5 mm material was not tested under high-strain rates; the high-rate properties corresponding to the HSLA350 1.8 mm material were also used for the HSLA350 1.5 mm material.

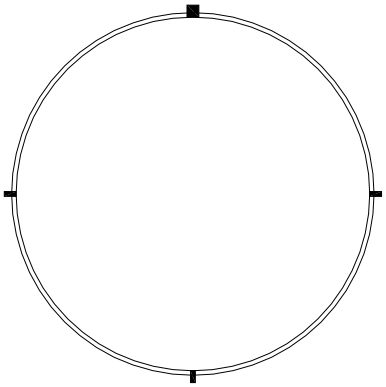

Figure 14: Tube positions

The results of the three quasi-static uniaxial tensile tests, as well as the quasi-static power-law models for the DDQ, HSLA350 1.5mm, HSLA350 1.8 mm, and DP600 steels are shown in Figure 15. The power law curves match the experimentally measured data very closely, especially for the DDQ and DP600 materials. The power law fits for all four materials are plotted in Figure 16 in order to show their relative strengths. As expected, DP600 is the strongest of the four materials, and is almost double the strength of the DDQ, which is the weakest material; the two HSLA350 materials lie in between these two extremes. The HSLA350 1.5mm material is slightly stronger than the HSLA350 1.8mm material.

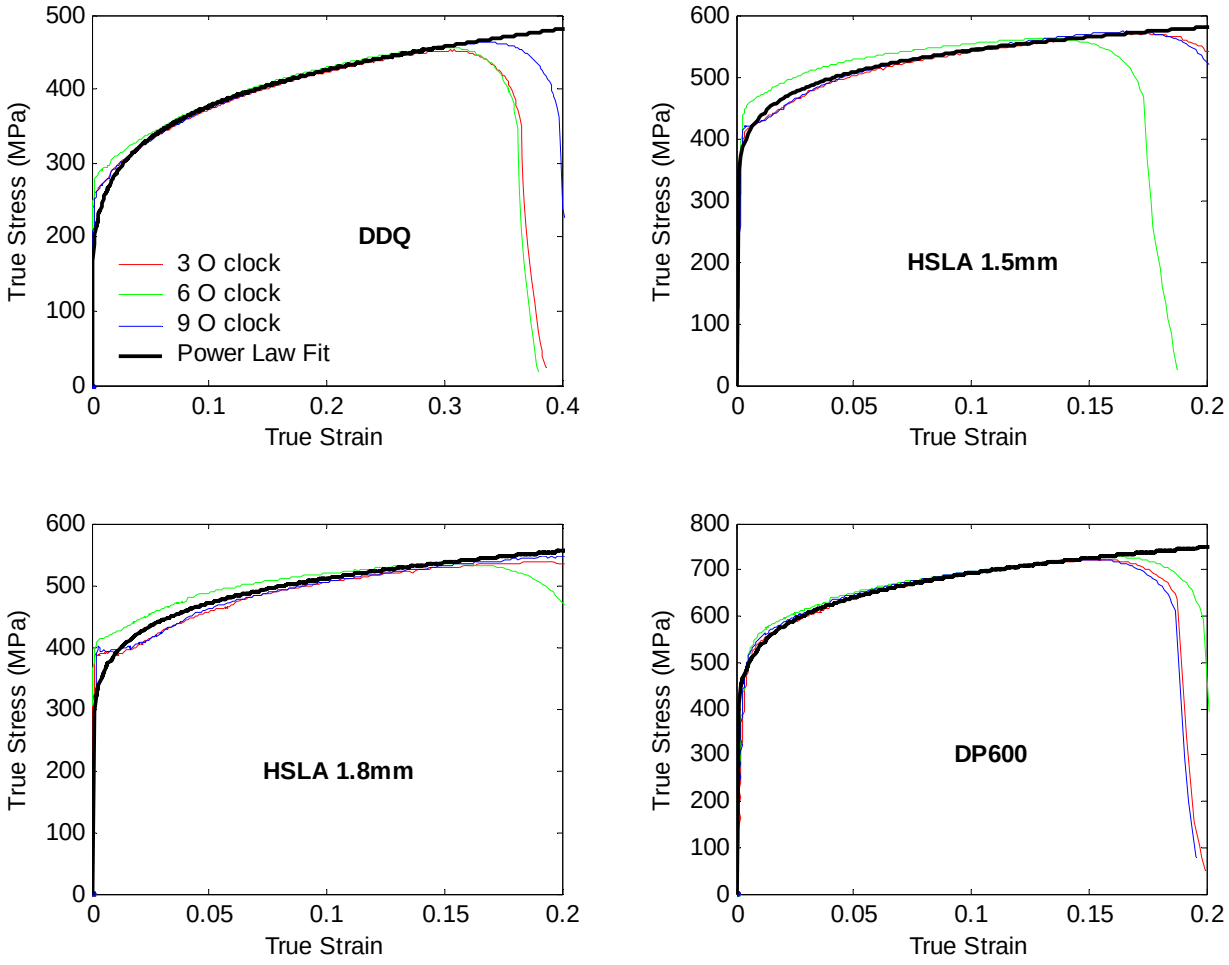

Figure 15: Measured and curve-fit quasi-static material responses for all four alloys

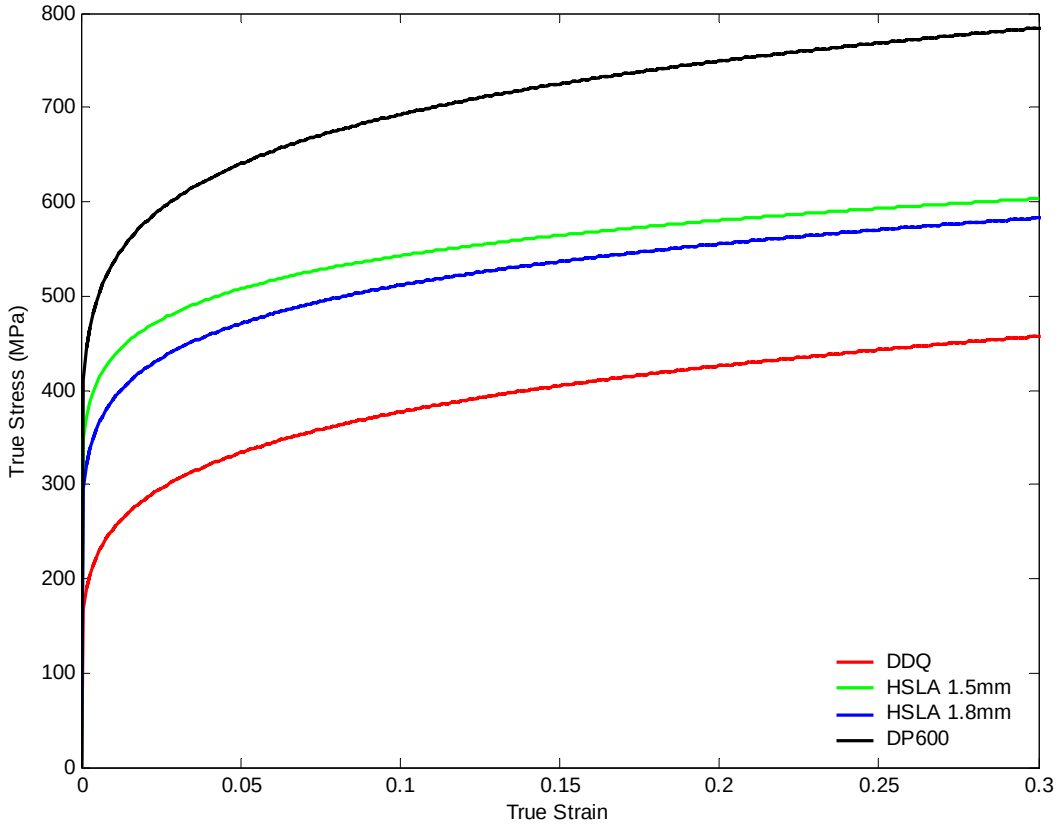

Figure 16: Quasi-static power law fits for all four alloys

The material responses at the quasi-static rate of strain (3.3 milli-strain/second) derived from the high-rate constitutive equations are shown in Figure 17 alongside the quasi-static responses given by the power law equation. The Johnson-Cook material model was used in the numerical finite element crash simulations for all four alloys, while the Zerilli-Armstrong model was used only for the HSLA350 1.8mm and DP600 materials. The modified Johnson-Cook equation with the Voce-type hardening term was only used for the DP600 material. There is a marked difference in the quasi-static responses given by the high-rate equations and those given by the power law equations that match the experimental quasi-static responses very closely. The Johnson-Cook curves are closer to the power law responses than the Zerilli-Armstrong curves. The response for DP600 given by the modified Johnson-Cook equation saturates at 760 MPa at a strain of roughly 20%. Despite the discrepancies at the quasi-static strain rates, Thompson (2006) shows that at higher rates of strain, the constitutive fits match the experimental results much more closely. The corresponding quasi-static and high-rate material parameters, as well as the average measured thicknesses of the tubes for each material are shown in Table 7. All high-rate testing and determination of high-rate constitutive parameters was performed by Thompson (2006).

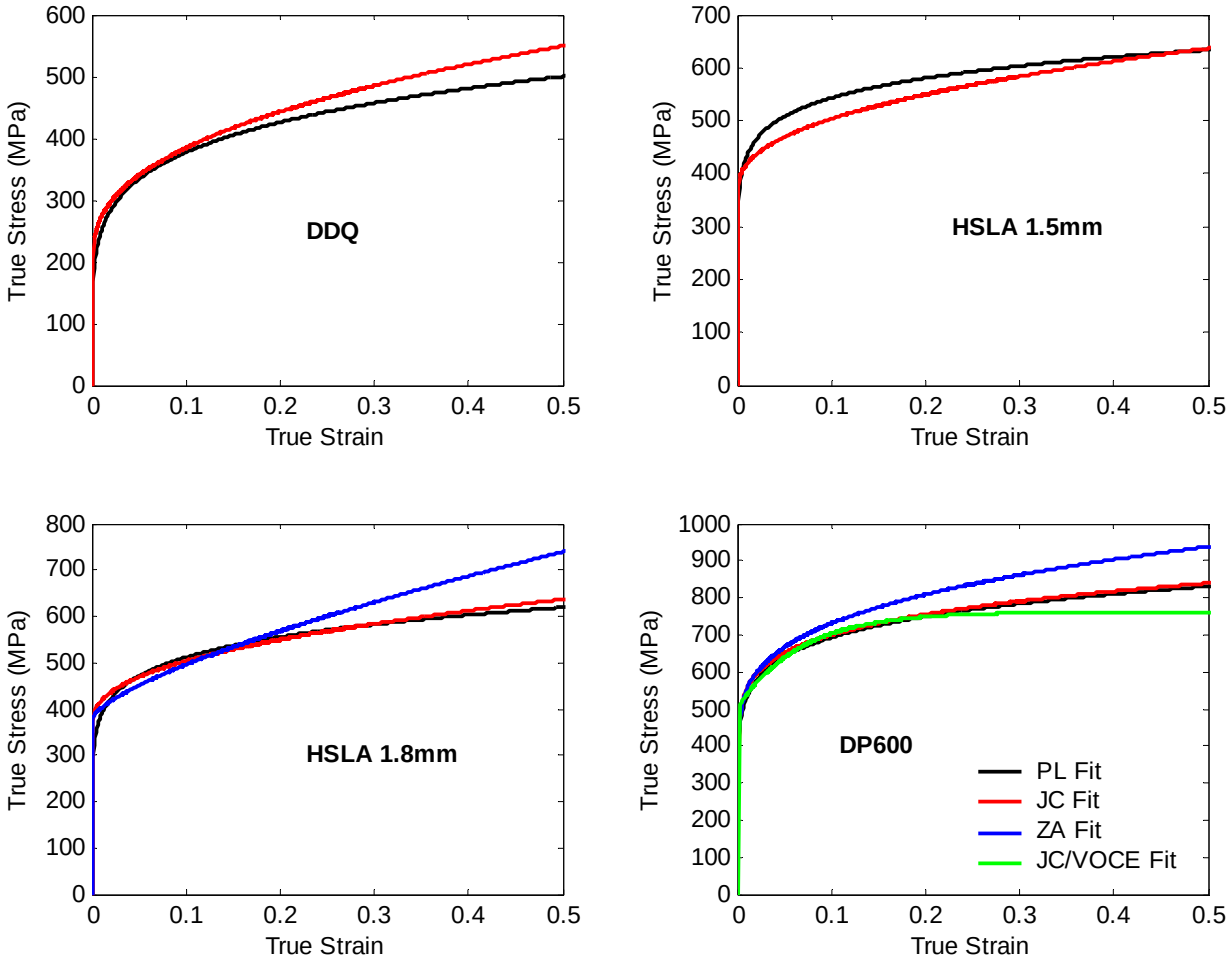

Figure 17: High-rate constitutive fits for the four alloys at the quasi-static rate of strain (PL = Power law, JC = Johnson-Cook, ZA = Zerilli-Armstrong, JC/VOCE = Modified Johnson-Cook with a Voce-type quasi-static term)

Table 7: Constitutive material parameters

		DDQ	HSLA350 1.5mm	HSLA350 1.8mm	DP600
	Thickness (mm)	1.86	1.53	1.86	1.86
Power Law	K (MPa)	565.0	677.5	672.3	898.9
	n	0.18	0.1	0.12	0.11
Johnson-Cook	A (MPa)	241.7	437.4	437.4	350.0
	B (MPa)	539.3	414.0	414.0	655.7
	n	0.40	0.44	0.44	0.19
	C	0.027	0.025	0.025	0.016
	m	1.20	0.78	0.78	1.00
	T_room (°C)	21	21	21	21
	T_melt (°C)	1221	1221	1221	1221
Johnson-Cook / Voce	A (MPa)	-	-	-	562.7
	B (MPa)	-	-	-	838.4
	n	-	-	-	15.07
	C	-	-	-	0.016
	m	-	-	-	1.00
	T_room (°C)	-	-	-	21
	T_melt (°C)	-	-	-	1221
Zerilli-Armstrong	C1 (MPa)	-	-	291.3	307.2
	C2 (MPa)	-	-	2592.3	7829.5
	C3	-	-	0.0096	0.0138
	C4	-	-	0.00032	0.00032
	C5 (MPa)	-	-	584.5	673.5
	C6 (MPa)	-	-	0.0	0.0
	n	-	-	0.706	0.288
	T_room (°C)	20	20	20	20

3.2 Tube bending simulations

The tube bending analysis sequence involved two explicit dynamic bending simulations, and two implicit springback simulations. After each analysis, a file was written that included all nodal positions and element connectivity, as well as the effective plastic strain, stress tensor, and thickness for each of the elements comprising the tube. After the first bend, the file containing the forming history was used as the input for an implicit calculation to account for elastic springback after bending. The forming history file written after the first springback calculation was used as the input for the second

bend, which was followed by the second springback calculation. In this manner, forming effects were carried over from one analysis to another.

3.2.1 Finite element mesh

For all tube bending and hydroforming simulations, the tube was modeled using fully-integrated quadrilateral shell elements with seven integration points through the thickness. All tooling components were modeled as rigid bodies. Despite their computational cost, fully-integrated elements were required for discretization of the tube since reduced-integration elements were incapable of modeling elastic springback.

The finite element mesh and setup for the first and second bends is shown in Figure 18. Upon completion of the first bend, the tooling was translated in the negative Z direction by the distance corresponding to the appropriate length of section C of the s-rail for each R/D ratio, as outlined in Table 2; the tooling was also rotated 180° about the Z axis in order to create the second bend in the opposite direction, as shown in Figure 18b.

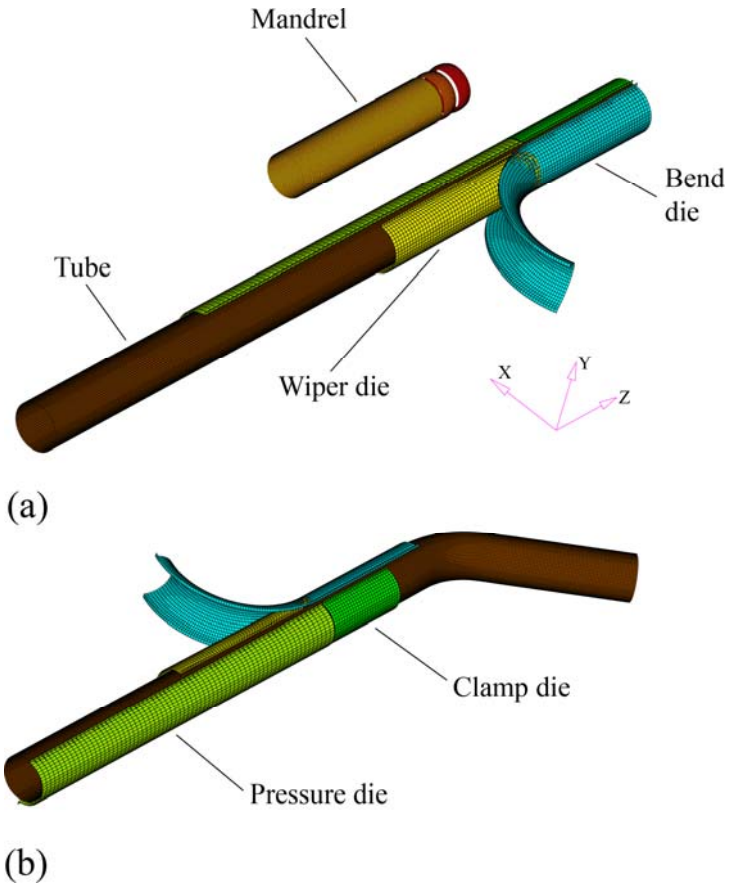

Figure 18: Finite element mesh of (a) the first bend (b) the second bend

The tube was meshed using 2.5 mm elements, based on a mesh convergence study performed by Oliveira *et al.* (2006). The pressure die, clamp die, bend die, and wiper die were meshed with an element size of 5 mm, while the mandrel was meshed with 2.5 mm elements. The tube bending models were comprised of 57 720 total elements, 31 980 of which belonged to the tube.

A detailed view of the mandrel is shown in Figure 19. In order to accurately capture the kinematics of the mandrel, rigid beam elements were created to depict the links between the balls, following the approach adopted by Dyment (2004). Each link was fixed to a mandrel ball at one end, and attached to a spherical kinematic joint at the other end to model the ball joints of the actual mandrel. All tooling dimensions were based on measurements taken of the actual tools used in the experiments. The wiper die rake angle was also measured for each of the experiments and positioned accordingly in the numerical models.

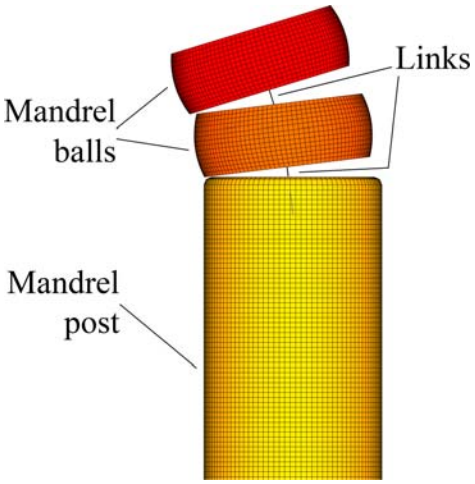

Figure 19: Detailed view of mandrel

3.2.2 Contact and friction

The interaction between the tube and rigid tooling was modeled using a penalty-stiffness based surface-to-surface contact algorithm in LS-Dyna. Since friction is known to be an important parameter in tube bending, friction coefficients were used in the numerical models based on twist-compression experiments performed by Bardelcik *et al.* (2005b) and Dyment (2004); these values are summarized in Table 8 for contact between the tube and each of the tools. The bending simulations of DP600 tubes at R/D ratios of 1.5 and 2.5 utilized a higher pressure die-to-tube friction coefficient than all other bending simulations due to the fact that pine tar powder was applied to the pressure die in the experiments, as outlined in Section 2.1.1. In order to determine the friction coefficient for this contact scenario, a

parametric study was performed numerically by varying the friction coefficient and measuring the degree of slip between the pressure die and tube. The numerically predicted slip matched the experimental slip measurement when a friction coefficient of 0.25 was used for this contact pair.

Table 8: Friction coefficients used in tube bending models

Tool	Material	Lubricant	Static and Dynamic coeff. of friction
Bend die	Nitrided 4130 tool steel	Dry	0.15
Pressure die	Nitrided 4130 tool steel	Dry (*pine tar powder)	0.15 (0.25*)
Clamp die	Nitrided 4130 tool steel	Dry	0.15
Wiper die	4130 tool steel	Hydrodraw 615	0.06
Mandrel	Nitrided and chromed 8620 tool steel	Hydrodraw 615	0.08

*Note: A coefficient of 0.25 was used for the bending models of DP600 at R/D ratios of 1.5 and 2.5.

3.2.3 Constraints, prescribed motions and loads

Constraints were assigned to the tools in the numerical tube bending models to match the constraints on the tools during the experiments. The degrees of freedom for each of the tools in the simulations are summarized in Table 9 (refer to Figure 18 for orientation of the axes). The tube did not have any constraints or boundary conditions applied to it in the bending models, aside from the contact definitions discussed above.

Table 9: Bend tooling degrees of freedom

Tool	DOF
Bend die	Y-rotation
Pressure die	X, Z-translation
Clamp die	X-translation
Wiper die	None (fully fixed)
Mandrel	All DOFs free

The tube bending process was simulated over a 30 millisecond span, even though the actual tube bending experiments lasted 4 seconds. This is a consequence of the fact that a real-time simulation of the tube bending process would surely require months of computation time, as opposed to half a day for the accelerated models used herein. The 30 millisecond simulation time was determined by Dyment (2004) to be the shortest time-span that did not inflict deleterious dynamic effects unto the results.

The sequencing of the loads and displacements prescribed to the tooling is shown in Figure 20. The clamp die was closed under displacement control in the x-direction in the first millisecond of the simulation; once fully closed, the clamp die was rigidly connected to the bend die, following the method outlined by Dyment (2004), which allowed for simple extraction of bending torque during post-processing of the numerical models. The pressure die clamp load was applied in the x-direction during the first six milliseconds of the simulation, and held constant for the remainder of the simulation. The bend die rotation about the y-axis and pressure die translation along the z-axis commenced upon full application of the pressure die clamp load at 6 milliseconds. The bend was completed during the final 24 milliseconds of the simulation using the same rotation and displacement ramping curves as the ones used in the experiments (the time axes of the curves were scaled accordingly). The mandrel was retracted 55 mm in the z-direction at 26.9 milliseconds, the simulation time corresponding to a bend angle of 42°. All the prescribed values of final displacement, rotation angle, and load were identical to those used in experiments (outlined in Table 3, Table 4, and Table 5). It should be noted that for the second bend, the displacement of the clamp die, the pressure die load in the x-direction, and the bend die rotation angle are negatives of the values displayed in Figure 20 since the tooling was rotated in the numerical models.

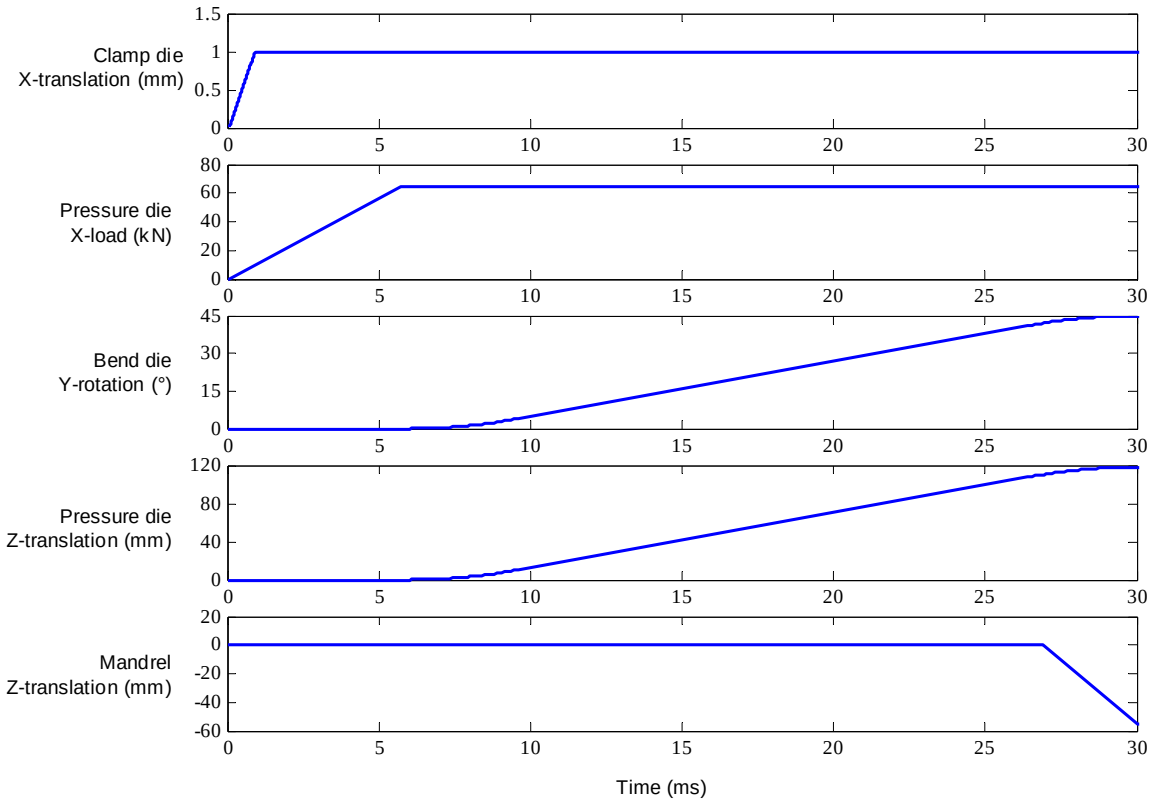

Figure 20: Tooling motion and loading history

3.3 Hydroforming simulations

The hydroforming simulation utilized the forming history file written after the second post-bending springback analysis to carry over the bending strains, stresses, and thickness changes. Upon completion of the hydroforming simulation, an implicit analysis was performed to simulate elastic springback, however, the degree of springback in hydroforming is minimal compared to bending.

3.3.1 Finite element mesh

The finite element mesh and setup for the hydroforming model is shown in Figure 21. The die surfaces were meshed based on a solid model of the actual hydroforming die used in the experiments. In order to avoid rotating the tube and performing stress tensor transformations, the meshed surfaces of the dies were rotated to properly align with the orientation of the tube after the second bend and springback stages; due to this orientation, the top die is closed along 45° trajectory.

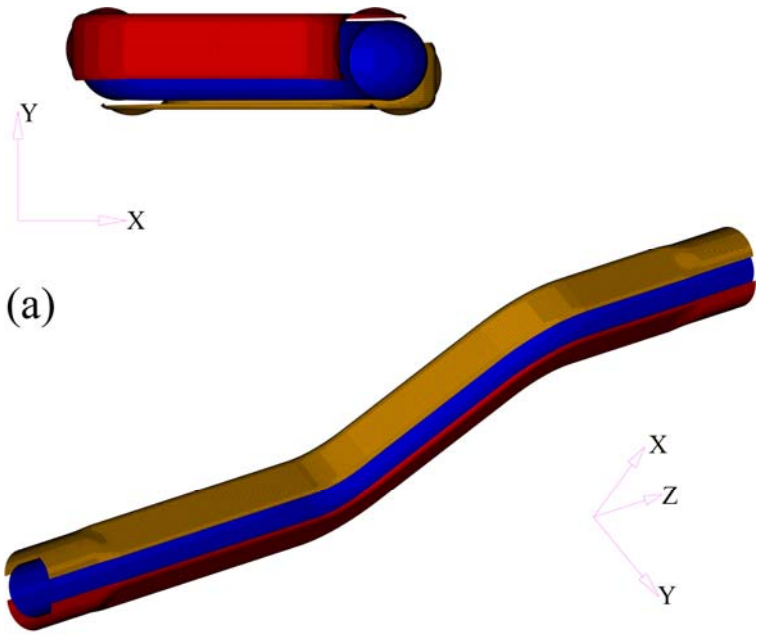

Figure 21: Finite element mesh of the hydroforming model (a) top view (b) isometric view

The surfaces of the dies were discretized with a mesh size of 2 mm, while the tube mesh was carried over from the tube bending simulations. The shortest possible length of tube was utilized in the

tube bending simulations in order to improve computational efficiency, however, this length was shorter than that of the hydroforming die. In the hydroforming simulations, the ends of the tube were extended to the corresponding length of the hydroforming die, and as a result, the tube was comprised of 35 256 elements (as opposed to 31 980 elements in the tube bending models), while the entire hydroforming model consisted of 90 156 elements.

3.3.2 Contact and friction

Contact and friction between the tube and die surfaces were accounted for in the same manner as in the tube bending simulations. A friction coefficient of 0.05 was used for all hydroforming simulations based on twist-compression experiments performed by Bardelcik *et al.* (2005b) and Dyment (2004) of contact between the tube materials and nitrided P20 tool steel lubricated with Hydrodraw 625 solid-film lubricant.

3.3.3 Constraints, prescribed motion and pressure

Constraints were assigned to the top and bottom dies in the numerical models in order to match the constraints on the tools during the experiments. The allowable degrees of freedom for the top and bottom dies in the simulations are summarized in Table 10. The top die translates in the x-y plane (refer to Figure 21a) so that it can close along a 45° path. The tube did not have any constraints or boundary conditions applied to it in the hydroforming models, aside from the contact definitions discussed above.

Table 10: Hydroforming tooling degrees of freedom

Tool	DOF
Upper die	X, Y-translation
Lower die	None (fully fixed)

The low-pressure hydroforming process was simulated over a 12 millisecond span, despite the fact that die closure in the experiments was a slow process requiring several minutes (the reason for this is outlined in Section 3.2.3). The internal pressure was linearly increased to 4.48 MPa (the average die closure pressure used in experiments) in the first millisecond of the simulation, and held constant during die closure. The top die was closed in 8 milliseconds, after which the internal pressure was linearly increased to the calibration pressure (the calibration pressure shown in Figure 22 is for the DP600 s-rails) in 2 milliseconds, and held constant for a further 2 milliseconds in order to fully form the s-rails.

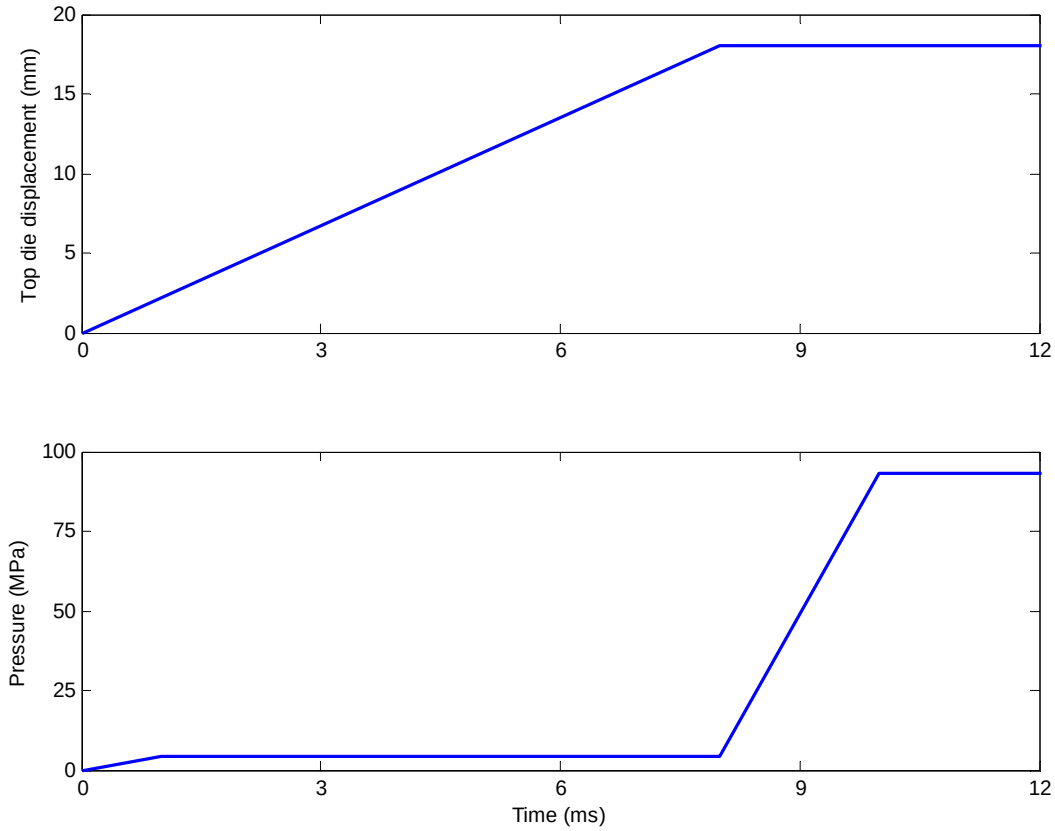

Figure 22: Top die motion and pressurization sequencing

3.4 Crash simulations

The crash simulation utilized the *dynain* file written after the post-hydroforming springback calculation to account for the effects of forming on the crash response of the structures. Numerical crash simulations were also conducted without the forming effects in order to isolate and quantify the effects of forming on crashworthiness.

3.4.1 Finite element mesh

The finite element mesh and setup for the crash model are shown in Figure 23. Only one s-rail structure was modeled for each crash analysis in order to take advantage of the symmetry of the crash setup. The ends of the tube were trimmed after the hydroforming springback simulation in order to obtain the correct overall length for the structure. A single rigid element was used to model the impact mass, while the tube was comprised of 28 938 elements.

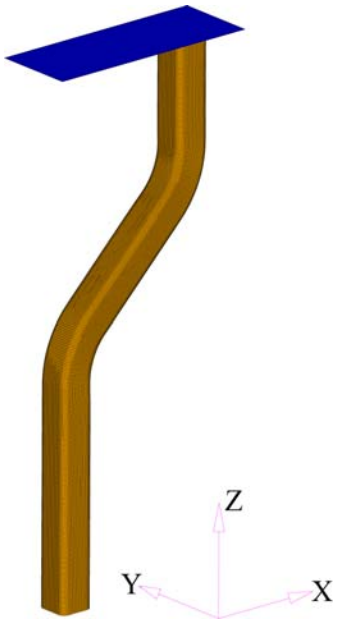

Figure 23: Finite element mesh of the crash model

3.4.2 Constraints and initial conditions

Nodes within 50 mm of the bottom end of the s-rail were fully constrained to model the clamped condition of the experiments; nodes within 50 mm of the top end of the s-rail were rigidly connected to the impact plate. These boundary conditions served to replicate the effects of the bosses and clamps, which were not directly modeled. The impact plate was constrained in all degrees-of-freedom except translation in the z-direction (refer to Figure 23).

A mass of 580 kg (the total mass of the sled and impacted plate in the experiments, divided by two) was assigned to the impact plate, which was also given an initial velocity of 4.57 m/s (as well as 6.46 and 8.06 m/s for the higher velocity simulations) in the negative z-direction to mimic the experimental crash conditions. Since the mass of the impact plate is much smaller than the mass of the sled, neglecting the fact that these components are separate entities is a reasonable assumption in the simulations, and has been shown to have insignificant effects by Oliveira *et al.* (2005b).

Chapter 4

Experimental results

This chapter presents the results from the tube bending, hydroforming, and crash experiments conducted as part of this research project. Forming process variables, crash loads, as well as strain and thickness measurements are analyzed in order to understand the effects of material strength, R/D ratio, initial wall thickness, sectional geometry, and impact velocity on the experimental results. Figure 24 shows non-hydroformed and hydroformed s-rails prior to crushing.

Figure 24: Comparison of (a) a non-hydroformed s-rail and (b) a hydroformed s-rail

4.1 Tube bending results

4.1.1 Repeatability of bending process variables

The process variables measured during bending are presented in this section, primarily in order to illustrate the high level of repeatability and low degree of scatter. The bend die rotation angle, pressure die feed displacement, and mandrel position were actively controlled during bending, therefore these results are not shown. The bend die torque, pressure die feed load, mandrel load, and pressure die clamp load are shown in Figure 25 for the first and second bends of four HSLA350 1.5 mm s-rails bent at an R/D ratio of 2.0. The variability in the presented results is typical of all the materials, therefore process variables are shown only for the HSLA350 1.5 mm material in this section. The approximate levels of variability of the results for all the materials and bending conditions are listed in Table 11. All forthcoming presentations of process variable results for the different materials will show the average results (the average of eight bends; four first bends, four second bends).

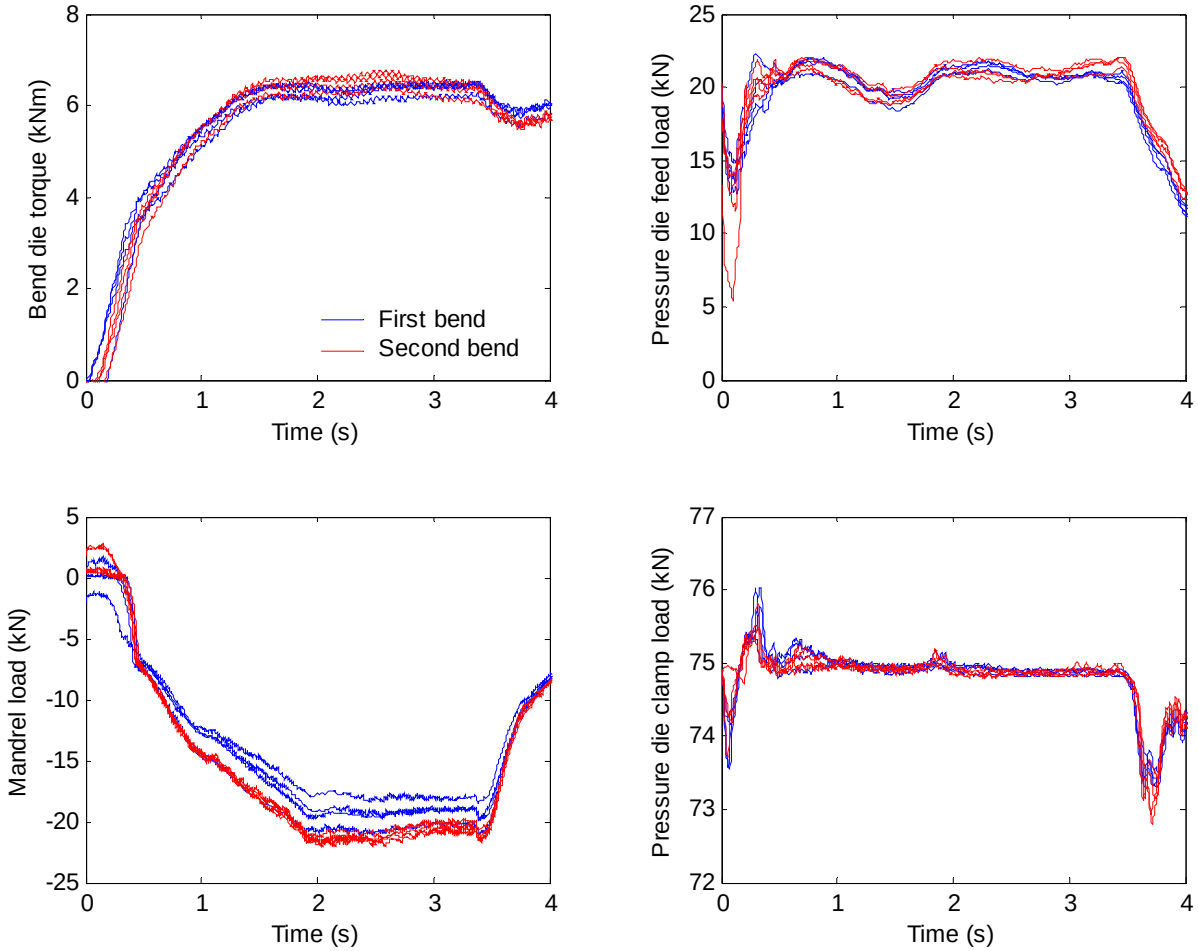

Figure 25: Bending process variables for HSLA350 1.5 mm s-rails bent at an R/D ratio of 2.0

Table 11: Variability of bending results

Material and R/D ratio	Bend die torque (kNm)	Pressure die feed load (kN)	Mandrel load (kN)	Pressure die clamp load (kN)
DDQ, R/D = 1.5	± 0.15	± 0.70	± 1.20	± 0.05
DDQ, R/D = 2.0	± 0.16	± 0.50	± 1.00	± 0.15
HSLA350 1.5 mm, R/D = 2.0	± 0.25	± 0.50	± 1.70	± 0.10
HSLA350 1.8 mm, R/D = 1.5	± 0.20	± 1.10	± 0.75	± 0.09
HSLA350 1.8 mm, R/D = 2.0	± 0.12	± 0.80	± 1.10	± 0.08
DP600, R/D = 1.5	± 0.17	± 1.00	± 1.10	± 0.10
DP600, R/D = 2.0	± 0.38	± 1.20	± 0.90	± 0.07
DP600, R/D = 2.5	± 0.75	± 2.10	± 1.00	± 0.05

The data presented in Figure 25 indicates that the process variables are similar (within the range of scatter) for the first and second bends of the s-rail. In general, the variability of the results increases with material strength, with the greatest degree of variability occurring during bending of DP600 at an R/D ratio of 2.5, while the most repeatable testing conditions occurred when using the DDQ material. This phenomenon occurred due to the fact that the tube bender was operating at a level close to its capacity when bending the higher strength DP600 steels. Variations in the lubrication conditions, such as the amount of lubricant applied to the wiper and mandrel, and in the case of the DP600 steels, the amount of pine tar applied to the pressure die, also contributed to scatter in the results.

4.1.2 Repeatability of post-bending strain and thickness measurements

A normalizing scheme was used to determine position along the length of the s-rail to simplify presentation the strain and thickness measurements such that the location of the measurements would be easily identified relative to the different sections of the s-rails; this normalizing procedure is illustrated in Figure 26. The normalizing procedure is linear, ie., the location halfway along the first bend (section B in Figure 5) corresponds to a normalized position of 1.5. For the measurements taken around the circumference of the first bend, angular positions were used with the weld seam representing the 0° and 360° locations, while the 90° location corresponds to the 9 o'clock position (refer to Figure 14) on the compressive side of the first bend. It should be noted that when the s-rail is positioned in the manner depicted in Figure 26, the weld seam is pointing upwards.

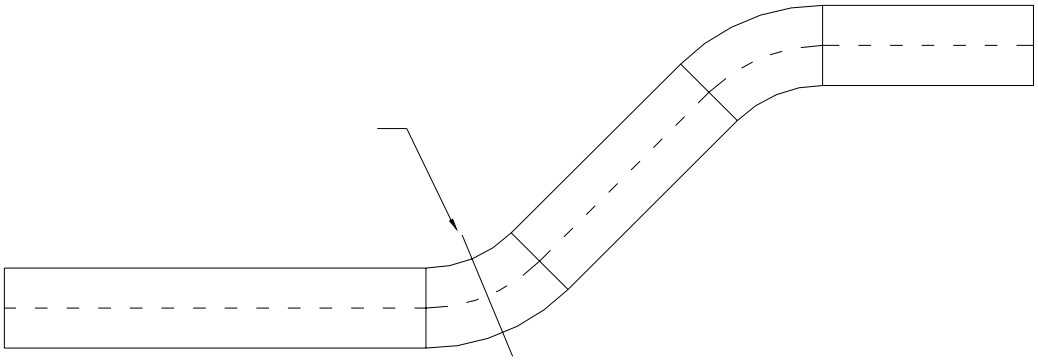

Figure 26: Schematic of normalized positions along s-rails (the normalized coordinates values are shown at the beginning of each section of the s-rail)

The strain and thickness measurement results for two HSLA350 1.5 mm s-rails bent at an R/D ratio of 2.0 are shown in Figure 27. The level of repeatability is typical of measurements taken on all the s-rails, therefore only the results of the HSLA350 1.5 mm s-rails are shown in this section. The graphs on the left side of the figure present results for the lower path of the s-rail (refer to Chapter 2, Figure 5), and the graphs on the right side of the figure present results of the circumferential measurements. The accuracy of the strain measurements is largely dependent on the quality, clarity, and darkness of the grids on the tubes. Although error bars are not plotted for the strain distributions, an error of ± 3% strain is generally associated with these measurements (Dyment, 2004), and the variability in the strain measurements between the two tests presented is less than this error. The thickness measurements, however, are not dependent on any such factors, and they are extremely repeatable along the lower path of the s-rail, as shown in Figure 27; the thickness measurements around the circumference of the s-rail exhibit scatter similar to that of the strain measurements. In view of these results, all forthcoming presentations of strain and thickness results will show only one representative curve for each condition. Due to their time consuming nature, strain measurements were only conducted for the two HSLA350 gauges, while thickness measurements were taken for all materials.

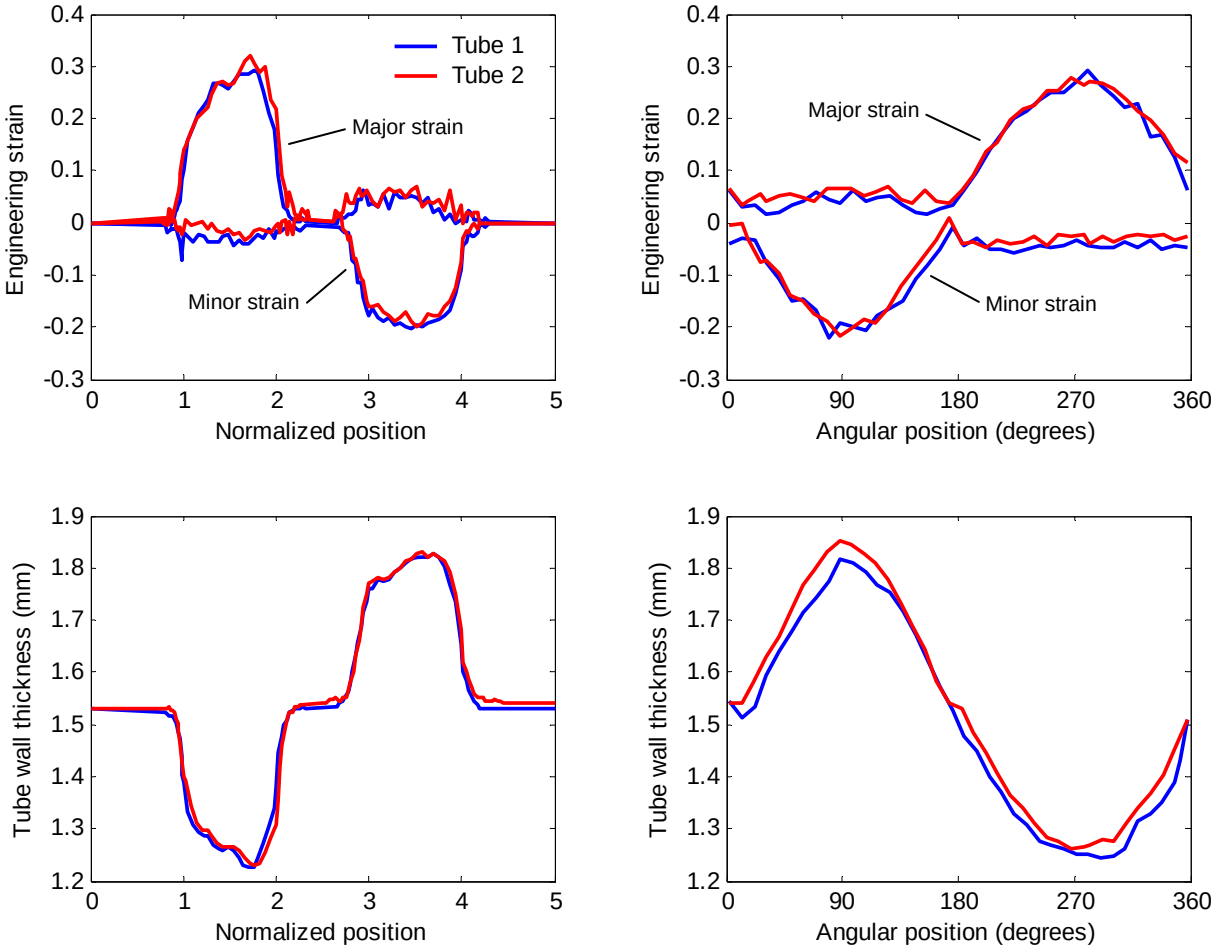

Figure 27: Strain and thickness measurements of HSLA350 1.5 mm s-rails bent at an R/D ratio of 2.0

4.1.3 Effect of material strength on tube bending results

The average bending process variables for DDQ, HSLA350 1.8 mm and DP600 at an R/D ratio of 2.0 are shown in Figure 28 in order to illustrate the effect of material strength on the bending parameters. As the material work-hardens during the bend, the torque required to continue deformation increases, as indicated in the plots. The bending torque for the DDQ and HSLA350 1.8mm materials is nearly identical, while the torque is nearly 2 kNm higher when bending the DP600 material. It is expected that the bend die torque would be higher for the HSLA350 1.8mm material in comparison to the DDQ material (due to their relative strengths), however, additional torque is also supplied to bend the tube due to the offset of the pressure die relative to the axis of rotation. The results indicate that the pressure die feed load is roughly 2-4 kN higher during bending of HSLA350 1.8mm when compared to DDQ; as expected, the pressure die feed load was the highest during bending of the DP600 material.

Differences in wiper setup can also affect the bend die torque due to changes in the frictional loads, however, these effects are expected to be minor.

The pressure die feed load for all three materials is relatively flat for the duration of the bend, which is a consequence of pressure die slip. Studies by Dyment (2004) have shown that if pressure die slip is eliminated (by directly pushing on the end of the tube), the pressure die feed load will continually increase during the bend, as opposed to the flat-line responses presented in Figure 28.

All mandrel loads presented in this work are shown with the convention of negative values denoting tensile loads on the mandrel and reflecting the fact that mandrel load is a drag force on the tube that acts against the action of the pressure die feed load. The clearance between the inside surface of the tube and the mandrel continually decreases as the tube is formed due to ovalization of the tube cross-section; consequently, the frictional load increases as a result of a higher normal load and a thinner film of lubricant, thereby increasing the mandrel load (in the negative direction) during the bend. The results indicate that mandrel load is virtually unaffected by material strength. Mandrel load is completely governed by frictional conditions, therefore increases in material strength are not expected to change the mandrel load appreciably; this explains why the mandrel loads for the HSLA350 1.8mm and DP600 materials are nearly identical, despite their large difference in strength. The mandrel load for the DDQ material is slightly larger in magnitude, however, this is most likely due to differences in the surface finish of the hot-rolled DDQ material compared to the cold-rolled DP600 and HSLA350 materials (hot-rolled surfaces are generally rougher than cold-rolled surfaces), and/or minor differences in the amount of lubricant used during bending. It should be noted that twist-compression testing was not performed on the DDQ material, therefore quantitative descriptions of the differences in surface finish are not available. In addition, the lower strength DDQ material has a higher propensity towards cross-sectional ovalization, which reduces the mandrel clearance and increases the magnitude of the mandrel load.

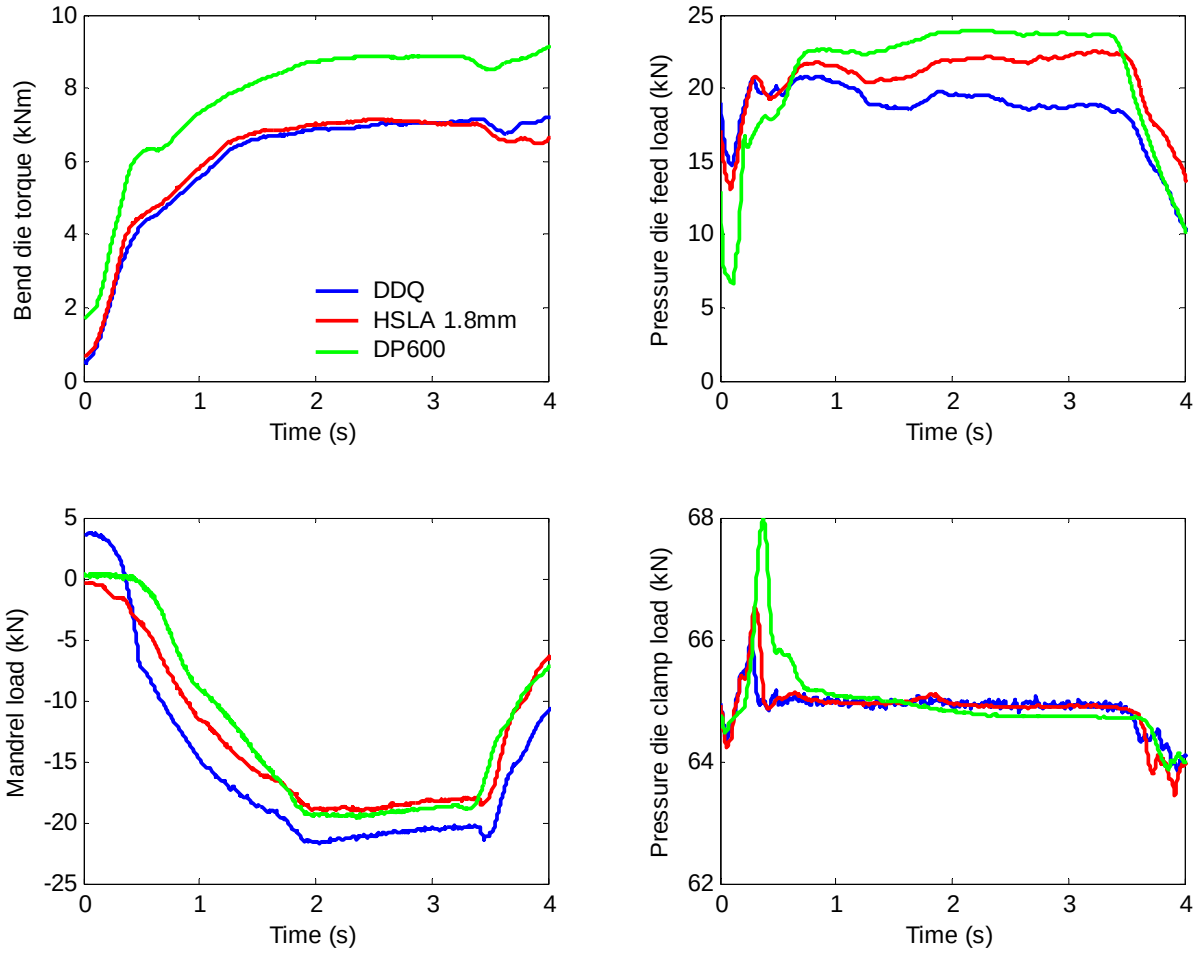

Figure 28: Bending process variables for DDQ, HSLA350 1.8 mm, and DP600 bent at an R/D ratio of 2.0

A pressure die clamp load of 65 kN was prescribed during bending of all of the aforementioned materials, which explains why the responses plotted in Figure 28 are nearly identical. During the first second of bending for all three materials, there is a spike in the pressure die clamp load with a relative magnitude that follows the relative strengths of the materials.

The results of the thickness measurements conducted on the three materials are plotted in Figure 29. The region with a normalized position between 1 and 2 (refer to Figure 26 for an overview of the normalizing scheme) corresponds to the tensile side of the first bend, while the region with a normalized position between 3 and 4 corresponds to the compressive side of the second bend. The degree of material thinning and thickening that occurs on the tensile and compressive sides of the bends diminishes after roughly a quarter of the distance into the adjacent straight sections.

The thickness measurements around the circumference of the tubes resemble a sinusoidal pattern with maximum thickness (thickening) on the compressive side of the bend and minimum

thickness (thinning) on the tensile side of the bend at 90° and 270°, respectively. The neutral axis of the bend is approximately at the 0° / 360° and 180° locations (it is shifted slightly towards the compressive side of the bend due to material thickening), hence the material thickness remains unchanged in these regions.

The level of thinning on the tensile side of the first bend is nearly identical for all three materials. The degree of material thickening on the compressive side of the second bend is nearly identical for the HSLA350 1.8mm and DP600 materials, while the DDQ material experiences slightly lower levels of thickening in this region. This result is consistent with the measurements taken around the circumference of the tube, since all three materials experienced similar levels of thinning, while there was a slight difference in the thickening response of the DDQ material. This anomaly is most likely a consequence of the surface finish of the hot-rolled DDQ steel; since sliding occurs between the tube and the wiper die on the compressive side of the bend, larger frictional forces (caused by the rougher surface of the hot-rolled DDQ) lessen the degree of material thickening on the compressive side of the bend. There is no sliding between the tube and any of the tools on the tensile side of the bend, therefore the DDQ thickness distributions closely match those of the other two materials. In general, however, material strength has a negligible effect on the wall thickness distribution within the s-rails.

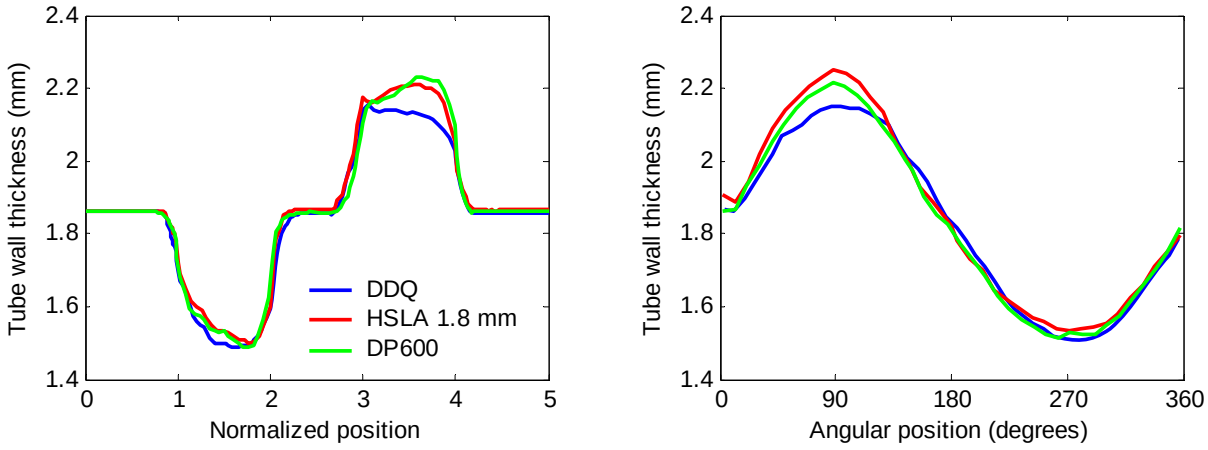

Figure 29: Thickness distributions for DDQ, HSLA350 1.8mm, and DP600 s-rails bent at an R/D ratio of 2.0

4.1.4 Effect of R/D ratio on bending results

The average bending process variables for DP600 bent at R/D ratios of 1.5, 2.0, and 2.5 are shown in Figure 30 in order to illustrate the effects of R/D ratio. When analyzing this data, it is important to note that pine tar powder was not used when bending at an R/D ratio of 2.0, therefore some of the differences in the results are not attributable to the R/D ratio, but are in fact a consequence of the use of the powder in bending. Thus, the best indication of the effects of R/D for nominally identical surface conditions can be obtained by comparing data from R/D ratios of 1.5 and 2.5. The bend die torque increases as the R/D ratio decreases (which is an expected result), with a maximum difference of 2.7 kNm of torque between tubes bent at R/D ratios of 1.5 and 2.5. The torque measured for the R/D ratio of 2.0 is only 0.5 kNm lower than that measured during bending at an R/D ratio of 1.5, however, this result is a consequence of the use of the powder. Inspection of the pressure die feed loads for the three R/D ratios indicates a maximum difference of roughly 13 kN between the measured responses of tubes bent at R/D ratios of 1.5 and 2.0, while the measured loads were nearly identical between the R/D ratios of 1.5 and 2.5. By using the pine tar powder, slip between the pressure die and tube was nearly eliminated, thereby drastically increasing the pressure die feed loads. As previously mentioned, increased pressure die feed loads reduce the bend die torque required to sustain deformation, therefore if slip were eliminated during bending at an R/D ratio of 2.0, the bend die torque would be reduced. In order to clearly illustrate the difference in torque during bending at R/D ratios of 1.5 and 2.0, the process variables measured during bending of HSLA350 1.8mm are presented in Figure 31. The pressure die feed loads are nearly identical due to similar pressure die friction conditions, while the bend die torque is roughly 2 kNm higher when bending at an R/D ratio of 1.5 as opposed to 2.0.

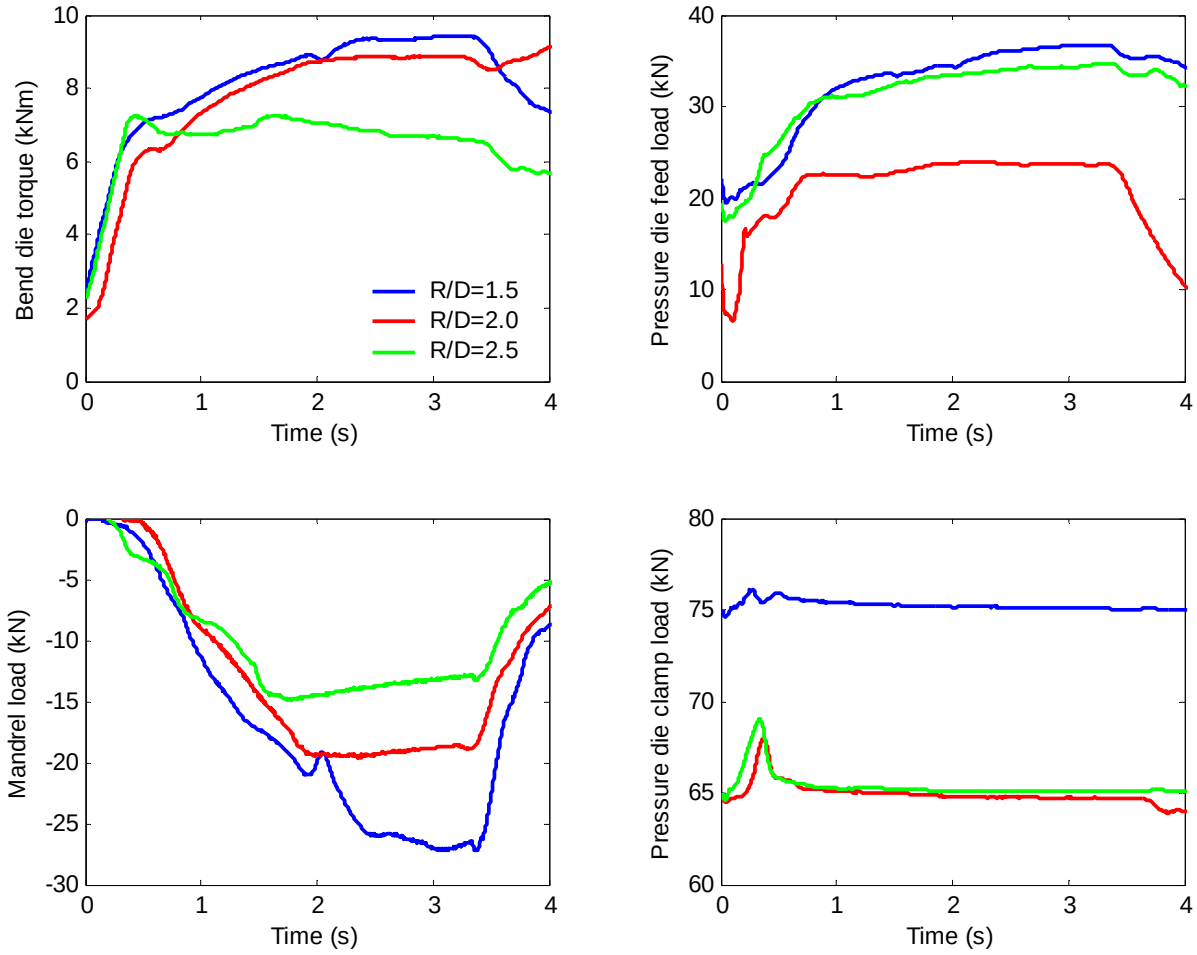

Figure 30: Bending process variables for DP600 bent at R/D ratios of 1.5, 2.0, and 2.5

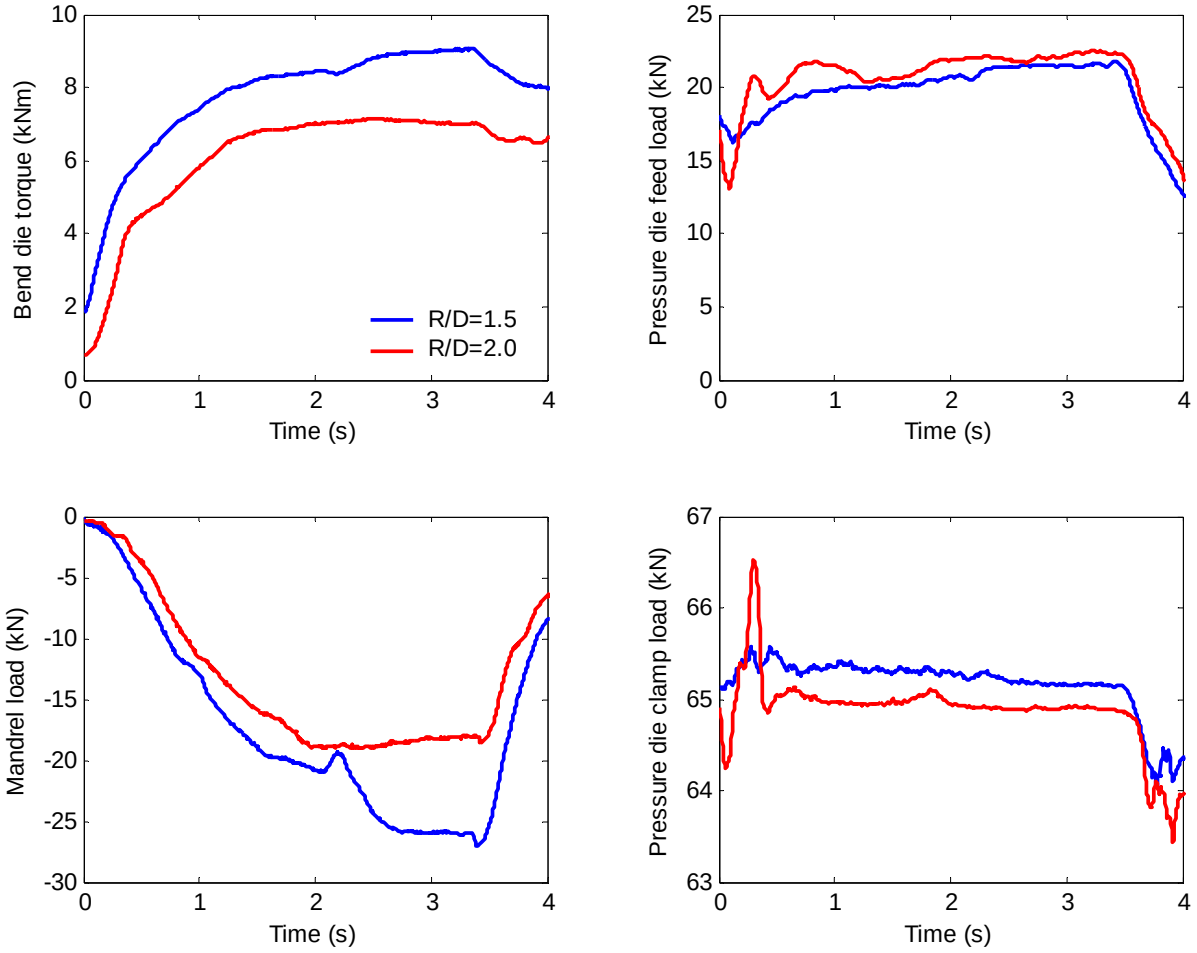

Figure 31: Bending process variables for HSLA350 1.8mm bent at R/D ratios of 1.5 and 2.0

The data shows a clear trend of increasing mandrel load with decreasing R/D ratio. As the bend radius becomes tighter, the degree of cross-sectional ovalization increases, thereby reducing the clearance between the mandrel and inner surface of the tube; this in turn increases the frictional loads on the mandrel, due to reasons already discussed. The mandrel loads measured during bending of HSLA350 1.8mm indicate a similar trend. A higher pressure die clamp load was required during bending of DP600 at an R/D ratio of 1.5 in order to eliminate wrinkling.

The thickness distributions for DP600 s-rails bent at R/D ratios of 1.5, 2.0, and 2.5 are shown in Figure 32. The level of thinning on the tensile side of the bend, and the level of thickening on the compressive side of the bend increases with decreasing R/D ratio. This result is expected due to simple geometric considerations; assuming that the mode of deformation is plane strain, geometric calculations predict minimum thicknesses of 1.24 mm, 1.40 mm, and 1.49 mm for R/D ratios of 1.5, 2.0 and 2.5, respectively, for the tensile side of the bend (these simple calculations are within 0.1 mm of the

measured results). The thickness distributions for the DDQ s-rails shown in Figure 33 indicate similar trends.

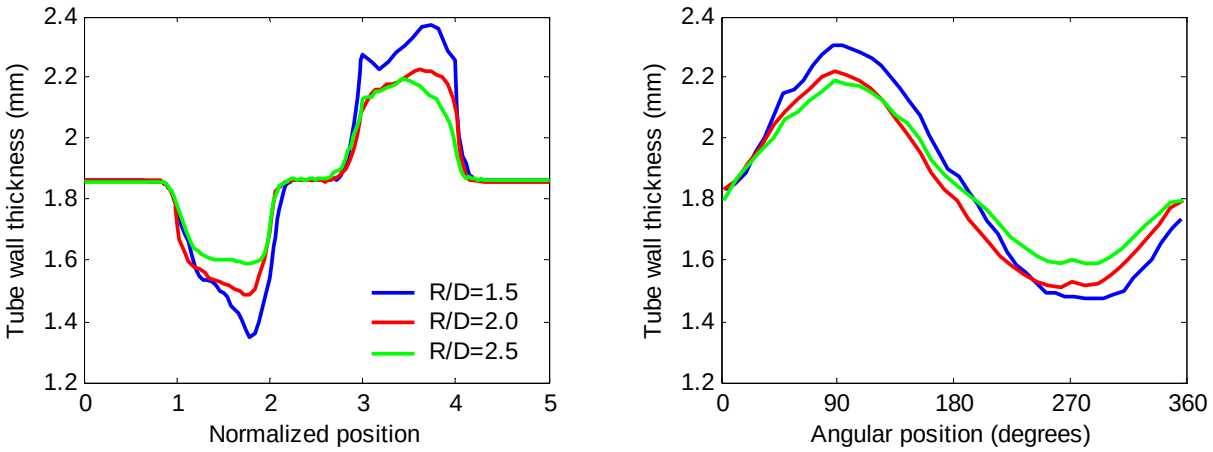

Figure 32: Thickness distributions for DP600 s-rails bent at R/D ratios of 1.5, 2.0, and 2.5

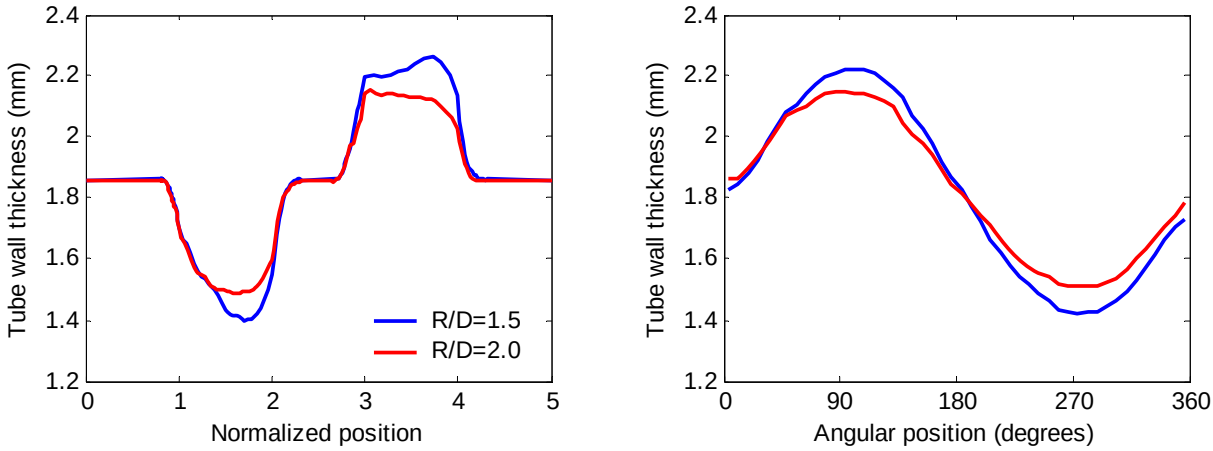

Figure 33: Thickness distributions for DDQ s-rails bent at R/D ratios of 1.5 and 2.0

4.1.5 Effect of initial material thickness on bending results

The average bending process variables for the HSLA350 1.5 mm and 1.8 mm materials at an R/D ratio of 2.0 are shown in Figure 34 in order to illustrate the effects of material thickness. The thicker gauge HSLA350 tube required a higher bending torque of roughly 1 kNm, and a higher pressure die feed load of roughly 1-2 kN. Referring to Figure 16 in Chapter 3 indicates that at 20% strain (the deformed regions of the tube experience roughly this amount of strain), the 1.5 mm gauge has a flow stress that is 4% higher than the 1.8 mm gauge, however, the thicker gauge tube has a cross-sectional

area that is 21% greater than the thinner gauge tube; consequently, higher loads are required to deform the 1.8 mm material.

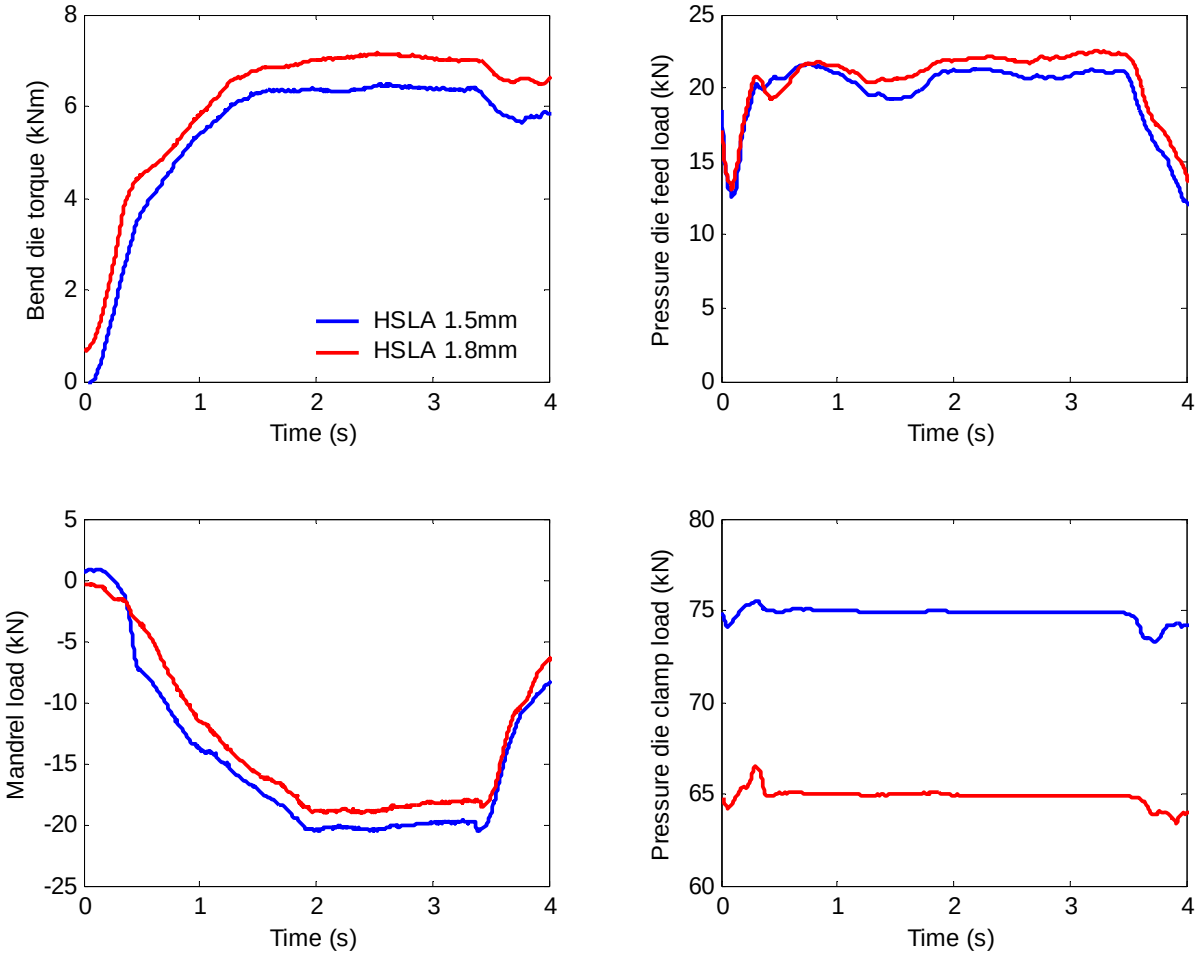

Figure 34: Bending process variables for HSLA350 1.5mm and 1.8mm bent at an R/D ratio of 2.0

The mandrel loads recorded for the 1.5 mm material are slightly higher than those measured for the 1.8 mm material. This result is due to the fact that the mandrel clearance was lower for the thinner gauge material (0.29 mm versus 0.49 mm for the 1.8 mm material). The thinner HSLA350 material also has a higher inclination towards cross-sectional ovalization, which also reduces the mandrel clearance. In addition to these factors, a higher pressure die clamp load was required for the 1.5 mm material in order to eliminate wrinkling, which also tends to increase mandrel loads due to the increased normal force of contact between the mandrel and tube.

The results of the strain and thickness measurements conducted on the HSLA350 s-rails are presented in Figure 35. Strain measurements could not be completed for the HSLA350 1.8 mm material

on the compressive side of the second bend due to the poor visibility and clarity of the circle grids in that region caused by sliding of the tube against the wiper die. On the tensile side of the bend, the major strains reach a maximum of 30 %, while the minor strains remain above -5%; on the compressive side of the bend, the minor strains reach a minimum (maximum magnitude) of roughly -20%, while the major strains remain below 5%. This indicates that the mode of deformation in tube bending is very close to plane strain; the minute degree of circumferential strain that negates the fully plane strain condition is due to cross-sectional ovalization. Simple geometric calculations assuming purely plane strain conditions predict tensile and compressive strains of ±25%. The reason for the discrepancy (in addition to the plane strain assumption) between the calculated and measured values is that the neutral axis of the bend shifts towards the compressive side of the bend due to material thickening, while the calculations assume that the neutral axis remains on the center-line of the tube.

Measurements taken around the circumference of the tubes show a sinusoidal-like decrease in the minor strain distributions on the compressive side of the bend, with a similar increase in the major strain distributions on the tensile side of the bend. The measured strains were nearly identical for both material gauges, indicating that initial material thickness has virtually no effect on the strain distribution of s-rails.

In order to compare the thickness measurements for tubes of different gauge, the measured values were normalized by the original thickness of the tube, thereby giving a percentage thickness change as shown in Figure 35. The plotted measurements show that the normalized thicknesses are virtually identical for the two gauges, therefore it is clear that initial material thickness has no effect on the percentage material thickness change.

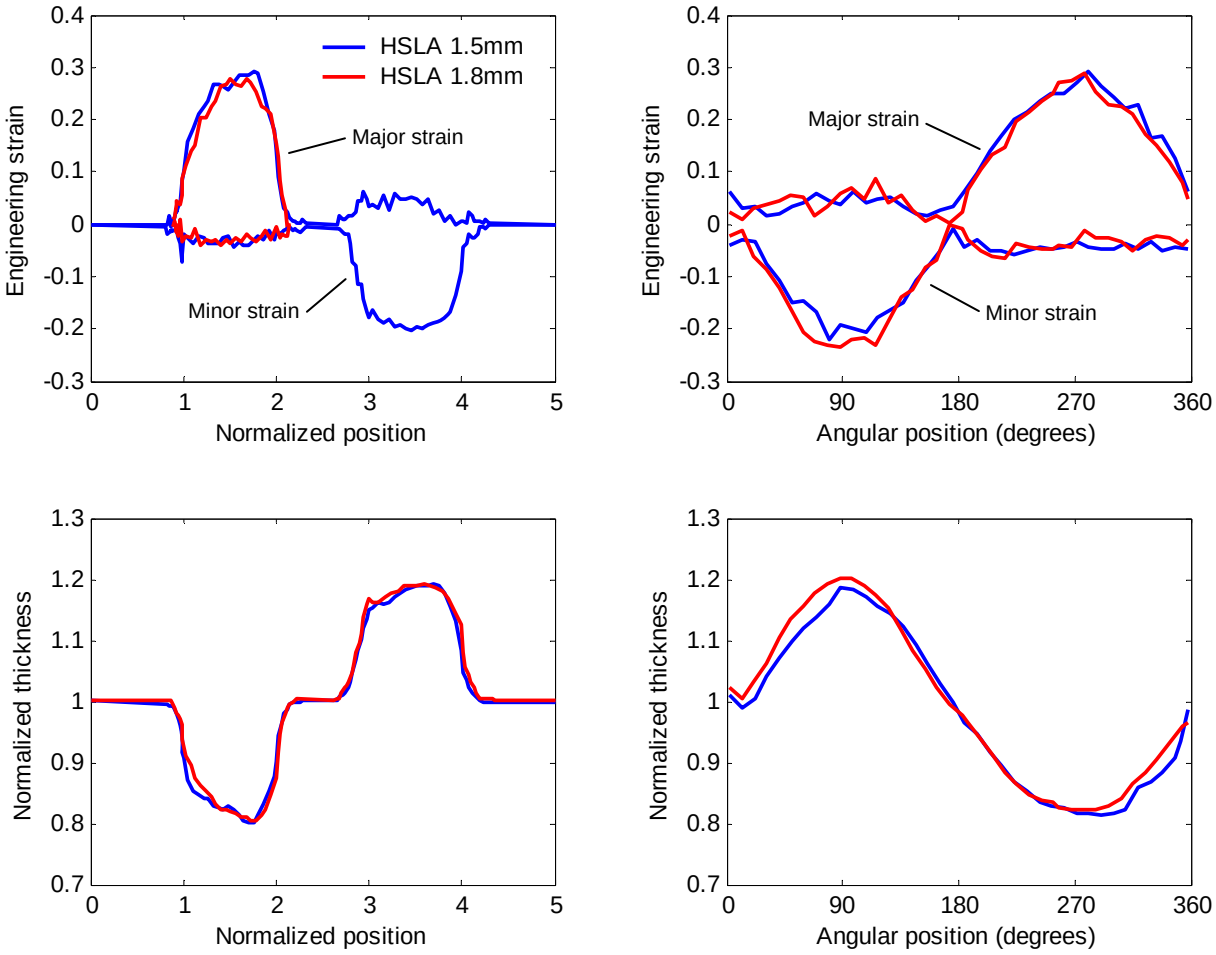

Figure 35: Strain and thickness distributions for HSLA350 1.5mm and 1.8mm s-rails bent at an R/D ratio of 2.0

4.2 Hydroforming results

4.2.1 Repeatability of post-hydroforming strain and thickness measurements

Before presenting all the hydroforming results, the strain and thickness measurements performed on the s-rails after hydroforming are presented in this section in order to show the degree of scatter and repeatability. For reference, the corners of the square cross-section occur at the 45°, 135°, 225°, and 315° locations around the circumference of the tube relative to the weld seam; the start and end positions of the first corner occur at the 32° and 58° locations, respectively, as shown in Figure 36. The post-hydroforming strain and thickness measurement results for two HSLA350 1.5 mm s-rails bent at an R/D ratio of 2.0 are shown in Figure 37; post-hydroforming measurements were taken only

around the circumference of the first bend. Strain measurements were taken only for the two gauges of HSLA350, while thickness measurements were taken for all materials.

The level of repeatability is typical of measurements taken on all the hydroformed s-rails, therefore results are shown only for the HSLA350 1.5mm s-rails in this section. The variability of the strain measurements is within the estimated error of ± 3% strain, while the thickness results from the two samples are nearly identical, with the exception of small variances at the corners. The variation is most likely due to the difficulty in placing the thickness measurement probe (which has a flat contacting surface) perpendicular to the tube due to the large curvature of the material in the corners. Aside from these exceptions, the post-hydroforming strain and thickness measurements are deemed repeatable, therefore all forthcoming presentations of these results will show only one representative curve for each condition.

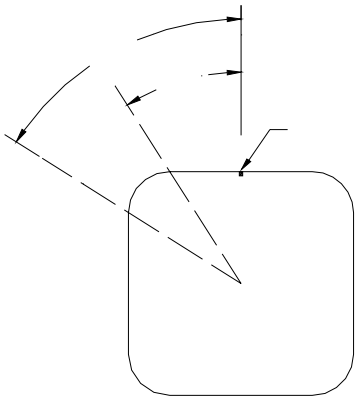

Figure 36: Corner locations relative to the weld seam

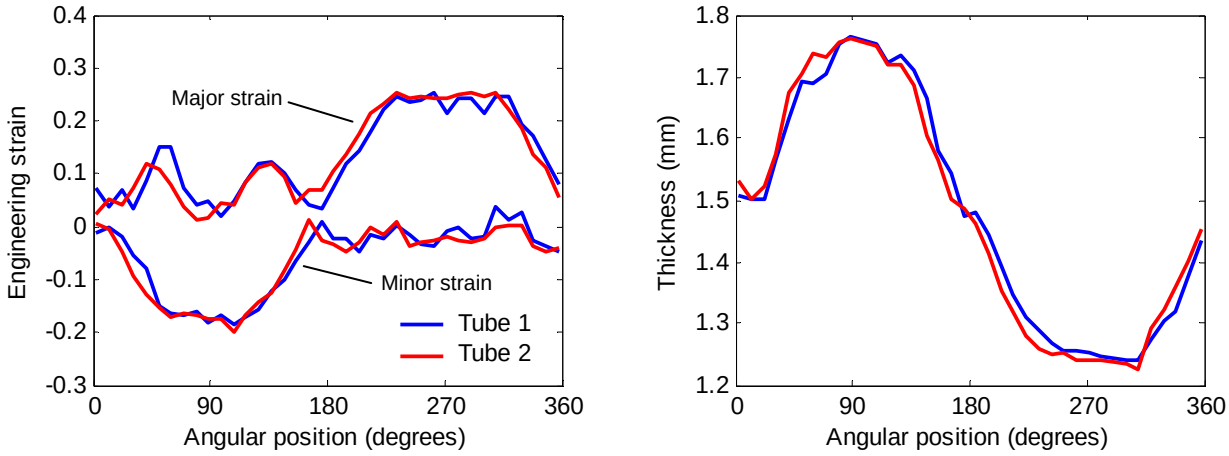

Figure 37: Post-hydroforming strain and thickness measurements of HSLA350 1.5 mm s-rails bent at an R/D ratio of 2.0

4.2.2 Effect of hydroforming on strain and thickness distributions

The strain and thickness distributions of an HSLA350 s-rail (bent at an R/D ratio of 2.0) before and after hydroforming are shown in Figure 38. Overall, the difference between the pre- and post-hydroforming distributions is difficult to discern, however, minor changes occur at the corners and adjacent regions. These results are expected, since studies such as those by Morphy (2001) and Koç *et al.* (2001) have revealed that the low-pressure hydroforming process will not dramatically change the thickness distributions of tubes.

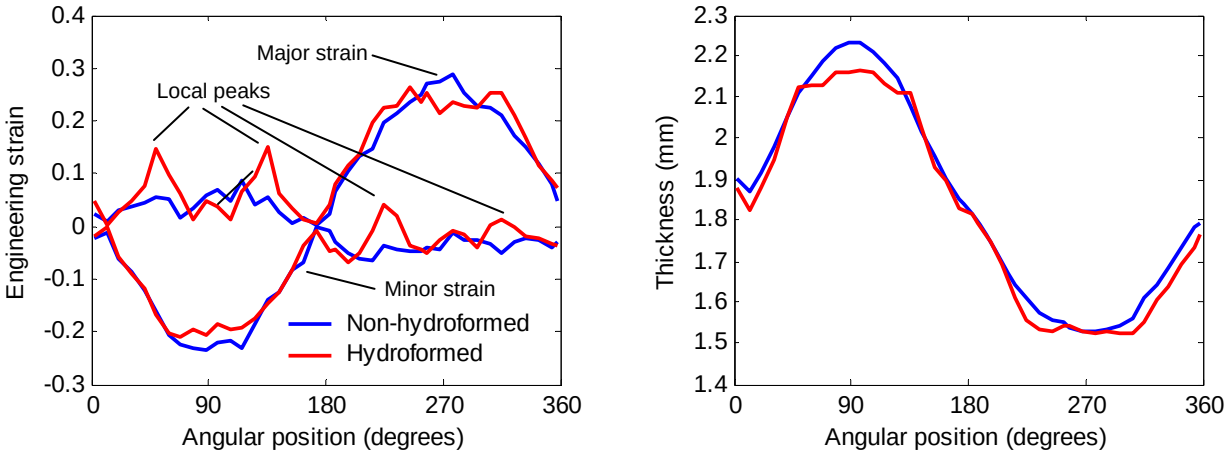

Figure 38: Pre- and post-hydroforming strain and thickness distributions of HSLA350 1.8 mm s-rails bent at an R/D ratio of 2.0

After hydroforming, the major strains increase sharply at the first two corners (at the 45° and 135° locations), while the minor strains increase slightly (a reduction in the compressive strain) across the flat region of the cross-section between the first two corners (between the 58° and 122° locations). As the tube material is bent sharply at the corners, tensile strains are induced on the outer surface of the tube in the major direction (the hoop direction on the compressive side of the bend), causing two spikes (local peaks) in the major strain at the first two corners. On the flat region of the cross-section, between the 58° and 122° locations, the material is gradually bent such that a small degree of compression occurs on the outer surface of the tube in the major direction, and through a Poisson's ratio effect, the minor strains increase slightly. On the tensile side of the bend, the minor strain is in the hoop direction, and again, two spikes occur at the corners (at the 225° and 315° locations). The major strains decrease slightly as a result of flattening of the material between the 238° and 302° locations.

The post-hydroforming thickness distribution indicates a slight (< 0.1 mm) degree of material thinning at the first two corners (at the 45° and 135° locations), which is due to the sharp bend required

to form the corners. The flat region of the cross-section between the first two corners also experiences a slight degree of material thinning. An even smaller degree of thinning occurs at the final two corners (at the 225° and 315° locations), while the flat region between these corners experiences virtually zero change in material thickness. All other regions around the circumference of the tube showed an indiscernible level of material thickness change.

4.2.3 Effect of material strength on hydroforming results

The pre- and post-hydroforming thickness distributions of DDQ, HSLA350 1.8mm, and DP600 s-rails are shown in Figure 39. It has already been established that material strength does not affect the thickness distributions of the s-rails (Section 4.1.3); examination of Figure 39 indicates similar trends for the hydroformed s-rails. The HSLA350 1.8mm and DP600 s-rails display nearly identical thickness distributions after hydroforming, while the wall thickness of the DDQ s-rails is roughly 0.1 mm lower than the other two materials on the compressive side of the bend; both of these results mimic those of the non-hydroformed s-rails. This suggests that any differences in the wall thickness distributions of hydroformed s-rails of differing strength are simply a result of the pre-hydroforming thickness distributions (which do not vary appreciably as a function of material strength) and not of the low-pressure hydroforming process. As noted in Section 4.1.3, the anomalous post-bending DDQ thickness results are most likely caused by differences between the surface finishes (hence differences in frictional properties) of the hot-rolled DDQ versus the cold-rolled HSLA350 and DP600 materials. Based on these results, it is clear that the thickness distributions of the hydroformed (low-pressure) s-rails are insensitive to material strength.

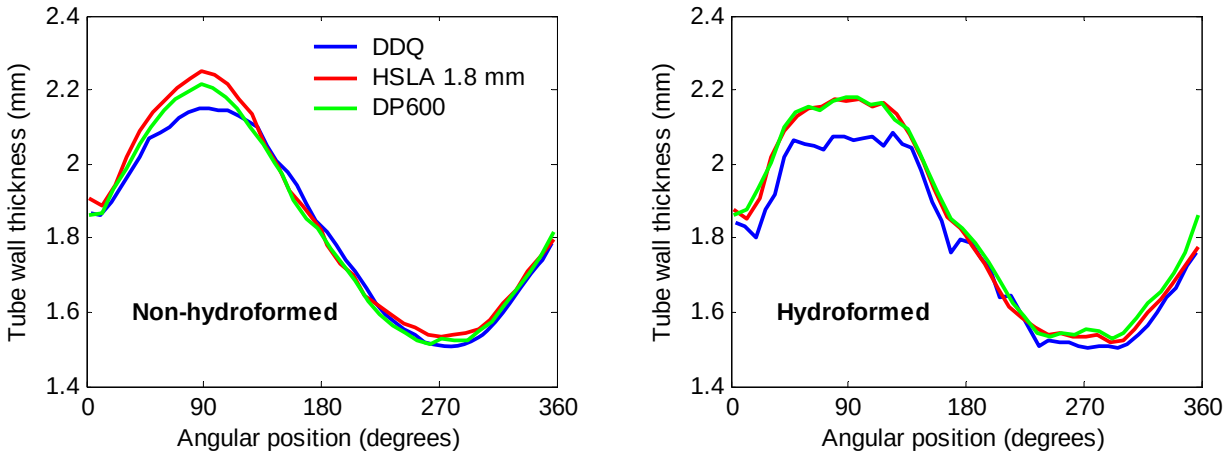

Figure 39: Post-hydroforming thickness distributions for DDQ, HSLA350 1.8mm, and DP600 s-rails bent at an R/D ratio of 2.0

Cross-sectional corner radius is a geometric parameter of hydroformed s-rails that is affected by material strength. Only the DDQ s-rails are formed to the full 12.0mm corner radius, while the measured corner radii of HSLA350 1.8mm and DP600 s-rails were 12.5 mm and 13.0 mm, respectively; this occurred despite the fact that greater internal pressures were used for the two higher strength materials (refer to Section 2.2.1). By equating the ultimate tensile strengths of the steels to the hoop stresses in the corners of the cross-sections, it can be shown that calibration pressures of 54, 71, and 98 MPa (7,800, 10,340, and 14,160 psi) are required for the DDQ, HSLA350 1.8mm, and DP600 materials, respectively; of the three materials, only the DP600 steel was formed with insufficient pressure due to the maximum capacity of the hydroforming press (roughly 94 MPa). Although the calibration pressure used for the HSLA350 1.8mm exceeded the calculated value by roughly 19 MPa (2,700 psi), the final corner radius was larger than the desired 12.0 mm, which suggests that the corner was fully formed during calibration, but opened slightly due to elastic springback upon removal of the internal pressure and tooling.

4.2.4 Effect of R/D ratio on hydroforming results

The pre- and post-hydroforming thickness distributions from the DP600 s-rails at the three R/D ratios are shown in Figure 40. The differences in the thickness distributions of the non-hydroformed s-rails are reflected in the hydroformed s-rails, with a clear trend of increasing material thickness change with decreasing R/D ratio. The same trend is apparent for the DDQ s-rails, as shown in Figure 41. As was the case in Section 4.2.3, the differences in the post-hydroformed thickness distributions of s-rails bent at different R/D ratios are a direct result of the bending process, and the thickness distributions of s-rails after the low-pressure hydroforming process are unaffected by the R/D ratio of pre-bent tubes. The final cross-sectional corner radii of the hydroformed tubes were not noticeably affected by R/D ratio, although it should be noted that the radius measurement tool makes readings in 0.5 mm increments, therefore differences smaller than this amount are not recognizable.

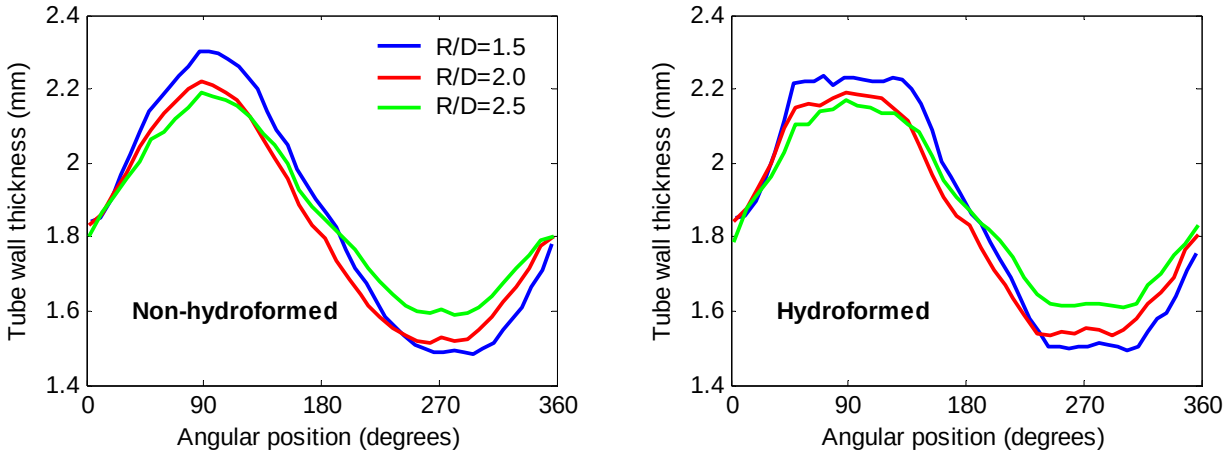

Figure 40: Post-hydroforming thickness distributions for DP600 s-rails bent at R/D ratios of 1.5, 2.0, and 2.5

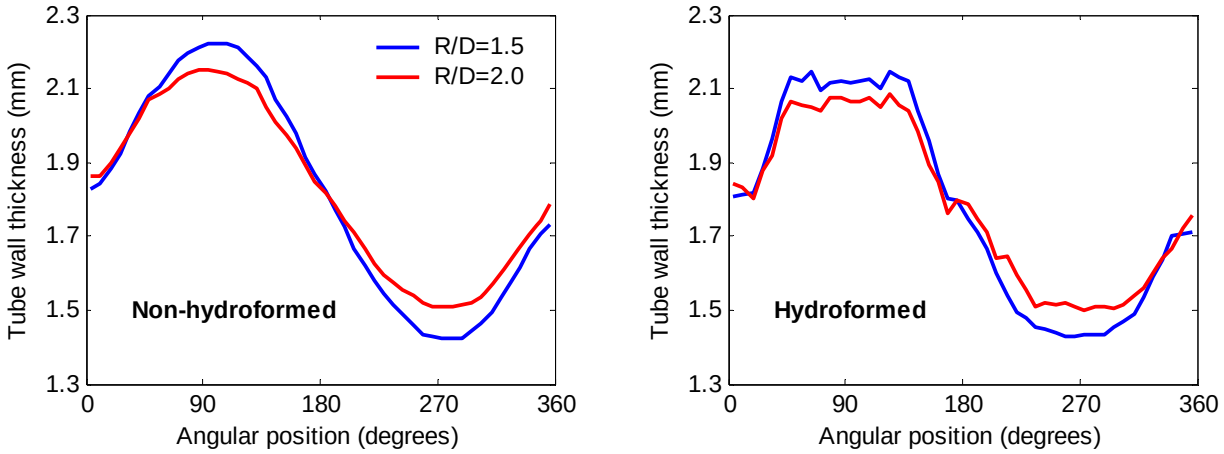

Figure 41: Post-hydroforming thickness distributions for DDQ s-rails bent at R/D ratios of 1.5 and 2.0

4.2.5 Effect of initial material thickness on hydroforming results

The pre- and post-hydroforming strain and thickness distributions of HSLA350 1.5 and 1.8 mm s-rails bent at an R/D ratio of 2.0 are shown in Figure 42. The thickness results are normalized by the original thickness of each HSLA350 gauge in order to allow for a direct comparison. The strain and thickness distributions after bending are clearly unaffected by initial material thickness (this was discussed in detail in Section 4.1.5); the same is true of the post-hydroforming thickness distributions, as shown in Figure 42. The strain and thickness results for the two gauges of HSLA350 are nearly identical, suggesting that initial material thickness does not affect the strain and percentage wall

thickness changes before or after hydroforming. There was no distinguishable difference between the measured cross-sectional corner radii of the HSLA350 1.5 and 1.8mm s-rails.

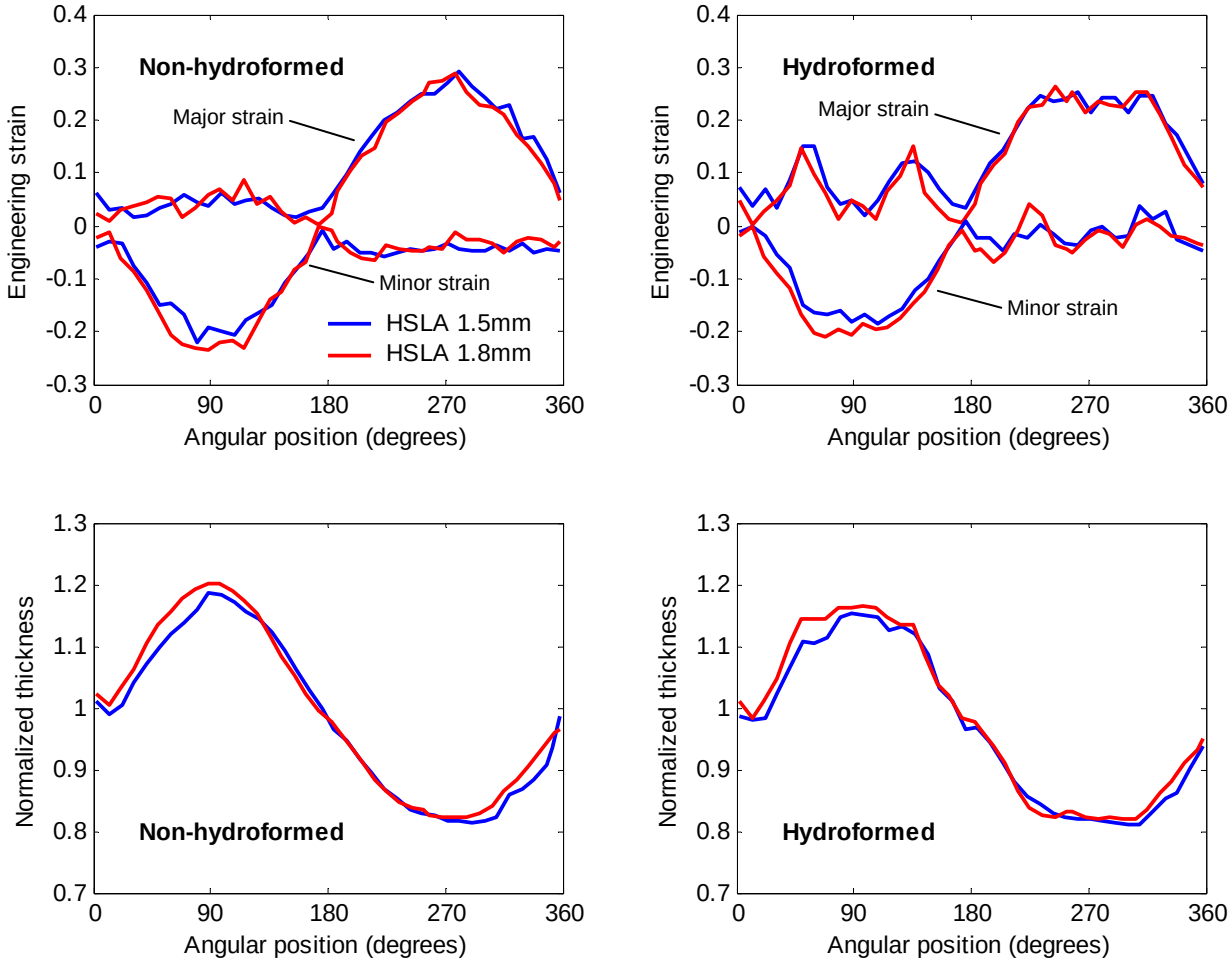

Figure 42: Post-hydroforming strain and thickness distributions for HSLA350 1.5mm and 1.8mm s-rails bent at an R/D ratio of 2.0

4.3 Crash test results

4.3.1 Repeatability of crash test results

Before presenting the results from the crash experiments, the loads measured during the crash tests are presented in this section in order to illustrate the degree of scatter and repeatability. All results are shown up to a displacement of 300 mm, since this corresponds to the maximum realistic crush displacement of an s-rail in a small automobile during crash events (the point at which the middle

section of the s-rail is parallel to the impacted plate). The displacement of an s-rail in an automotive crash scenario is limited to this amount due to the intervention of other elements, such as the engine, tires, and other crash structures within the automotive frame.

The crushing loads from three impact experiments conducted on non-hydroformed HSLA350 1.8mm s-rails bent at an R/D ratio of 2.0 are shown in Figure 43; the crushing loads are essentially identical for all three tests. The load-displacement data is numerically integrated using a trapezoidal rule integration scheme in order to derive the energy absorption response of the structures, which again, is nearly identical for all three tests. This level of repeatability is typical of all the tests (conducted on non-hydroformed, as well as hydroformed s-rails), therefore results are shown only for the non-hydroformed HSLA350 1.8mm s-rails in this section. Although the data is omitted, the loads measured from the left and right s-rails during crash are essentially identical, therefore all crash data (experimental and numerical) contained in this thesis is presented for two s-rails. Based on the excellent repeatability displayed in the crash tests, all forthcoming presentations of these results will show only one representative curve for each condition.

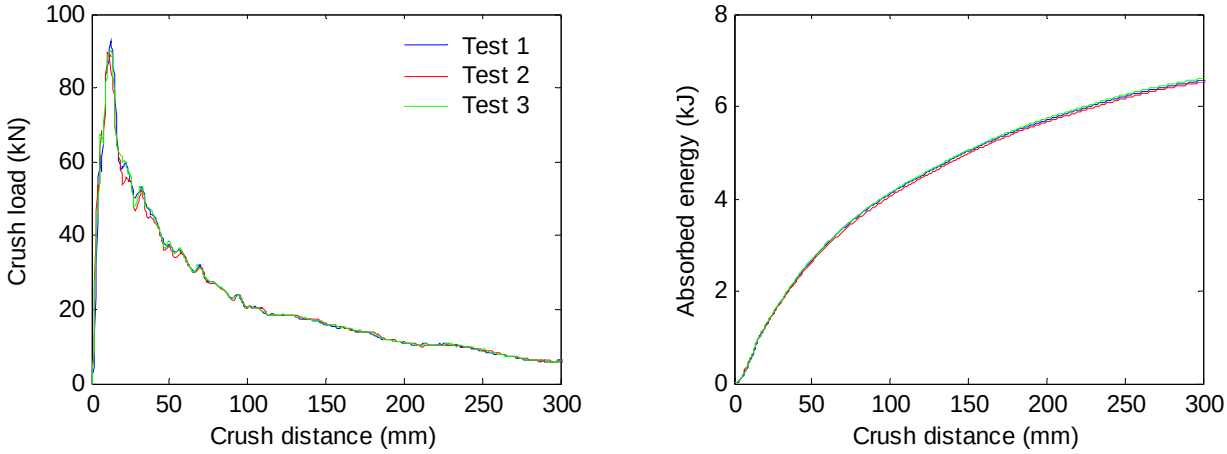

Figure 43: Crash test results for non-hydroformed HSLA350 1.8mm s-rails bent at an R/D ratio of 2.0

4.3.2 Effect of hydroforming on crash test results

The load-displacement and energy-displacement curves for non-hydroformed and hydroformed HSLA350 1.8mm s-rails bent at R/D ratios of 1.5, and 2.0 are shown in Figure 44 and Figure 45, respectively. The peak loads measured during the test, as well as the values of absorbed energy after 300mm of crush distance are listed in Table 12 for each R/D ratio; percentage differences are presented

in parentheses with respect to the non-hydroformed s-rails. The tabulated results are also presented graphically in Figure 46.

At the onset of crash, the measured load quickly increases to a peak corresponding to the load required to initiate the bending collapse mode of deformation in the s-rails; once bending collapse has commenced, the load decreases dramatically as the tube cross-section collapses in the plastic hinge regions. The rate of energy absorption is highest at the beginning of the crash test, since this is the point at which the load on the structure is greatest.

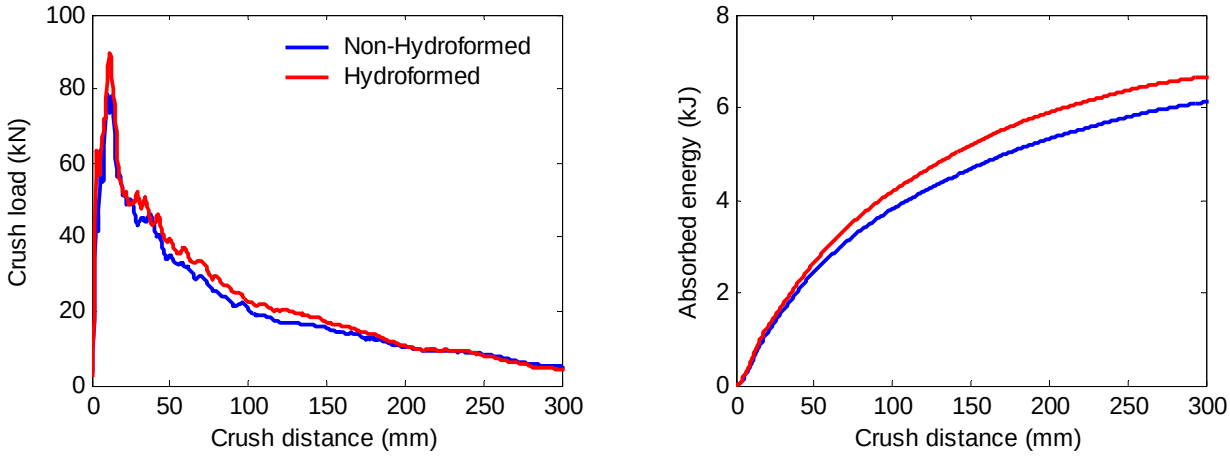

Figure 44: Crash test results for hydroformed and non-hydroformed HSLA350 1.8mm s-rails bent at an R/D ratio of 1.5

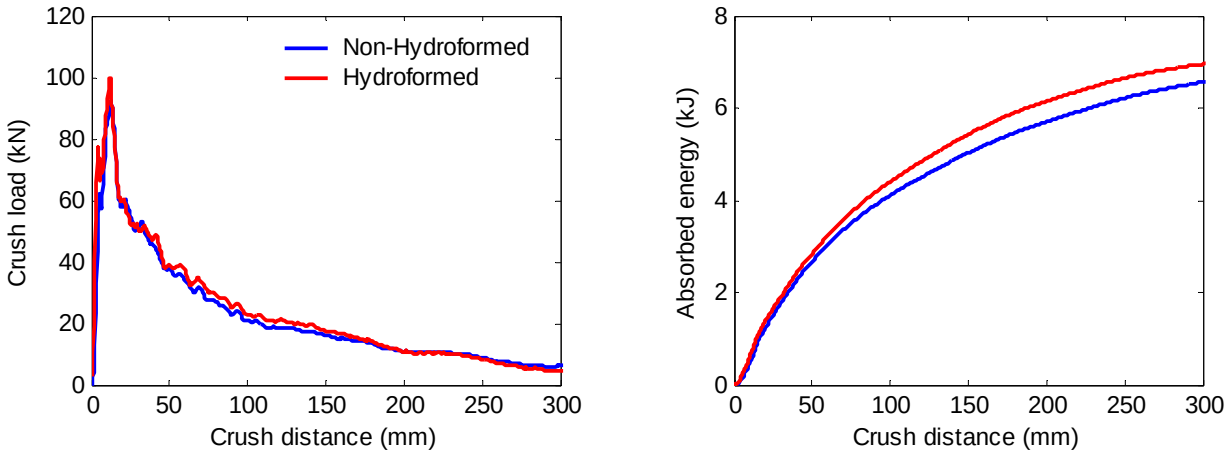

Figure 45: Crash test results for hydroformed and non-hydroformed HSLA350 1.8mm s-rails bent at an R/D ratio of 2.0

The difference between the crash performance of the non-hydroformed and hydroformed structures appears to be small, especially for the s-rails bent at an R/D ratio of 2.0. The increase in the

peak loads of hydroformed s-rails bent at an R/D ratio of 1.5 is 13.7% when compared to corresponding non-hydroformed structures, whereas this increase is only 7.9% for the s-rails bent at an R/D ratio of 2.0; the same trend is apparent in the energy absorption results. This comparison indicates that despite the minor difference in the crash response of non-hydroformed and hydroformed s-rails, hydroforming has a greater effect on the crash performance of s-rails at tighter bend radii. Since the difference in the crash response of non-hydroformed and hydroformed s-rails is so small, all forthcoming presentations of crash test results (except for the higher velocity tests) will focus only on the hydroformed s-rails.

Table 12: Peak load and energy results for non-hydroformed and hydroformed HSLA350 1.8mm s-rails bent at R/D ratios of 1.5 and 2.0

	R/D=1.5		R/D=2.0	
	Non-hydro	Hydro	Non-hydro	Hydro
Peak load (kN)	78.6	89.4 (+13.7%)	92.6	99.9 (+7.9%)
Energy @ 300 mm (kJ)	6.11	6.66 (+9.0%)	6.56	6.95 (+5.9%)

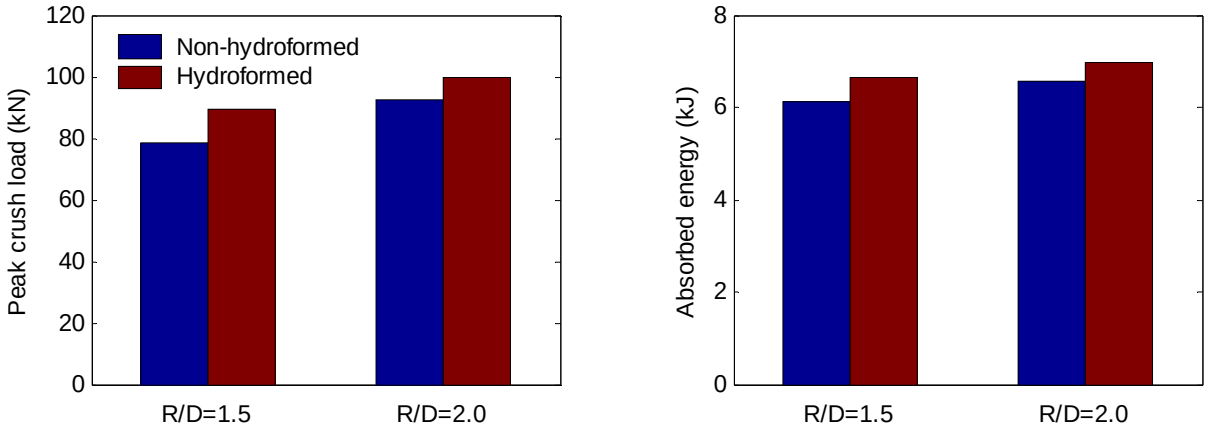

Figure 46: Peak load and energy results for non-hydroformed and hydroformed HSLA350 1.8mm s-rails bent at R/D ratios of 1.5 and 2.0

The reason for the small difference in the crash performance of non-hydroformed and hydroformed s-rails is due to the small difference in the bending rigidity of the two cross-sections, as well as the minor changes in strain and thickness after hydroforming. The second polar moment of area for a non-hydroformed s-rail cross-section is 300.3×10^3 mm^4, while that of a hydroformed section is 319.9×10^3 mm^4, a difference of only 6.5%, which will not drastically affect the crushing loads. Furthermore, previous discussions have illustrated that the low-pressure hydroforming process does not strain or thin the tube material appreciably, therefore work hardening and strength changes due to changes in wall thickness are minimal. It should be emphasized that hydroforming processes that

induce a larger increase in the section modulus will result in larger increases in crush load and absorbed energy.

4.3.3 Effect of material strength on crash test results

The load-displacement and energy-displacement curves for hydroformed DDQ, HSLA350 1.8mm, and DP600 s-rails bent at an R/D ratio 2.0 are shown in Figure 47. The peak loads measured during the test, as well as the values of absorbed energy after 300mm of crush distance are listed in Table 13 and presented graphically in Figure 48; for the tabulated results of the HSLA350 1.8mm and DP600 s-rails, percentage differences are presented in parentheses with respect to the DDQ s-rails.

The loads measured during the tests show that DP600 s-rails exhibit the strongest crash response followed by the HSLA350 1.8mm s-rails, which is an expected result based on the relative strengths of the materials (refer to Section 3.1, Figure 16). The peak load measured for the HSLA350 1.8mm s-rails is 28.0% higher than that of the DDQ s-rails, while the peak load for the DP600 s-rails is 12.1% higher than that of the HSLA350 1.8mm s-rails. The energy absorbed by the HSLA350 1.8mm s-rails is 31.1% higher than the energy absorbed by DDQ s-rails, while the absorbed energy for the DP600 s-rails is 25.0% higher than that of the HSLA350 1.8mm s-rails. This data indicates that the percentage increase in peak load and energy absorption is greater for HSLA350 1.8mm relative to DDQ than for DP600 relative to HSLA350 1.8mm.

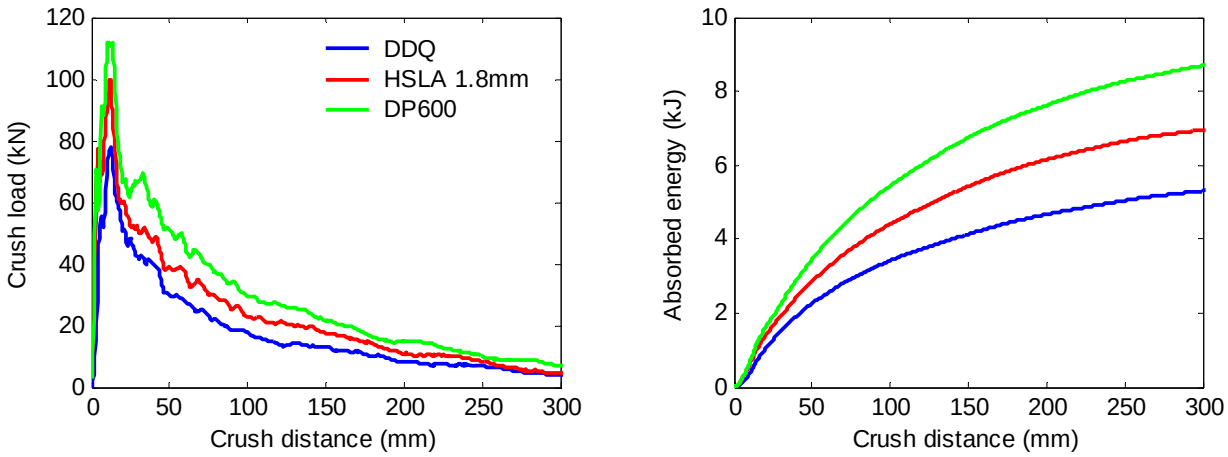

Figure 47: Crash test results for hydroformed DDQ, HSLA350 1.8mm, and DP600 s-rails bent at an R/D ratio of 2.0

Table 13: Peak load and energy results for hydroformed DDQ, HSLA350 1.8mm, and DP600 s-rails bent at an R/D ratio of 2.0

	DDQ	HSLA350 1.8mm	DP600
Peak load (kN)	78.0	99.9 (+28.0%)	112.1 (+43.7%)
Energy @ 300 mm (kJ)	5.30	6.95 (+31.1%)	8.69 (+64.0%)

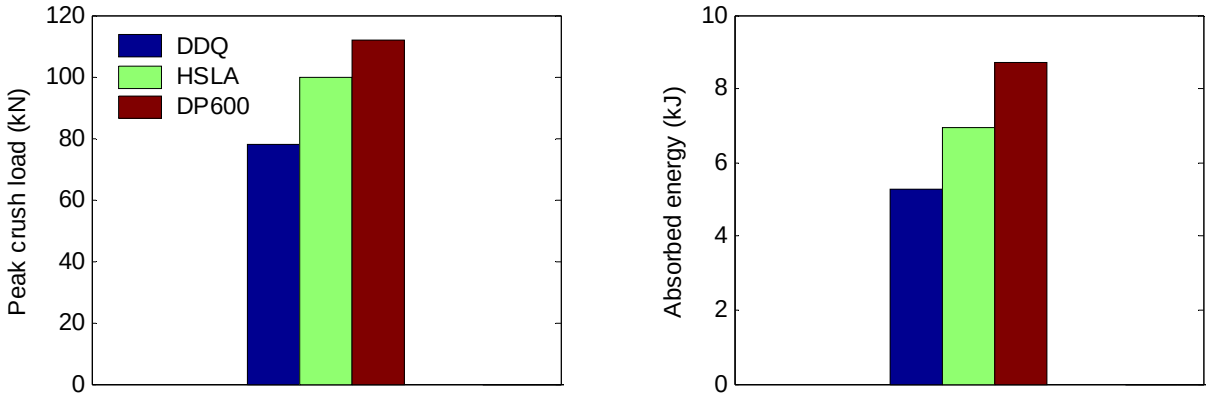

Figure 48: Peak load and energy results for hydroformed DDQ, HSLA350 1.8mm, and DP600 s-rails bent at an R/D ratio of 2.0

4.3.4 Effect of R/D ratio on crash test results

The load-displacement and energy-displacement curves for hydroformed DP600 s-rails bent at R/D ratios of 1.5, 2.0, and 2.5 are shown in Figure 49. The peak loads measured during the test, as well as the values of absorbed energy after 300mm of crush distance are listed in Table 14 and presented graphically in Figure 50; for the tabulated results of the s-rails bent at R/D ratios of 2.0 and 2.5, percentage differences are presented in parentheses with respect to the s-rails bent at an R/D ratio of 1.5.

The difference between the response of s-rails bent at an R/D ratio of 1.5 and that of s-rails bent at an R/D ratio of 2.0 is minor, with the peak load lying 6.3% higher and the energy absorption 4.7% higher in the case of the R/D=2.0 s-rails. The effect of the bend radius is more apparent at the R/D ratio of 2.5, since the measured peak load and energy absorption are 11.7% and 8.5% higher than the R/D=2.0 s-rails. Comparison of s-rails bent at the most severe (R/D=1.5) and least severe (R/D=2.5) bend radii indicates a difference of 18.7% in the peak load and 13.6% in the energy absorption, with the less severe bend radius exhibiting the stronger response for both measures.

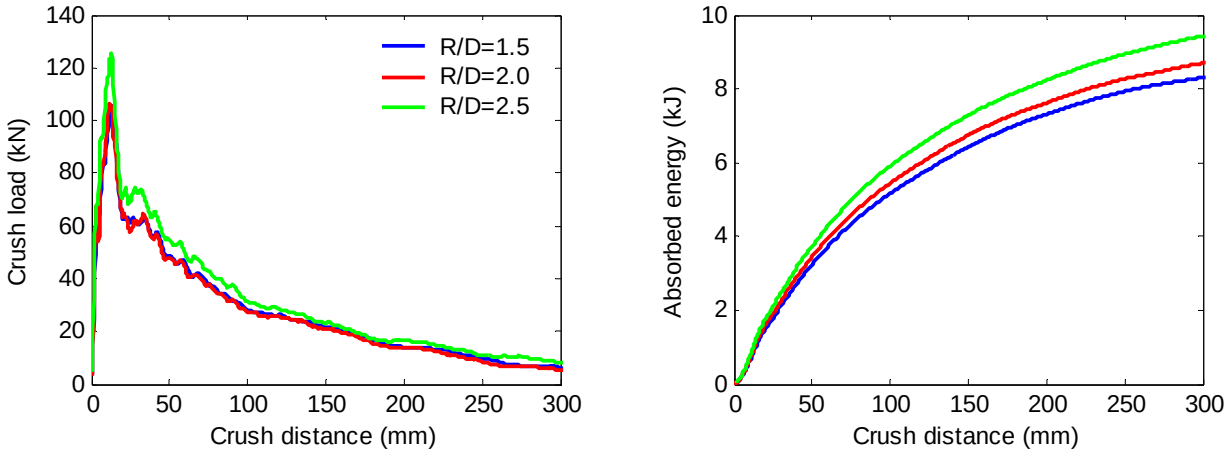

Figure 49: Crash test results for hydroformed DP600 s-rails bent at R/D ratios of 1.5, 2.0, and 2.5

Table 14: Peak load and energy results for hydroformed DP600 s-rails bent at R/D ratios of 1.5, 2.0, and 2.5

	R/D=1.5	R/D=2.0	R/D=2.5
Peak load (kN)	105.5	112.1 (+6.3%)	125.2 (+18.7%)
Energy @ 300 mm (kJ)	8.30	8.69 (+4.7%)	9.43 (+13.6%)

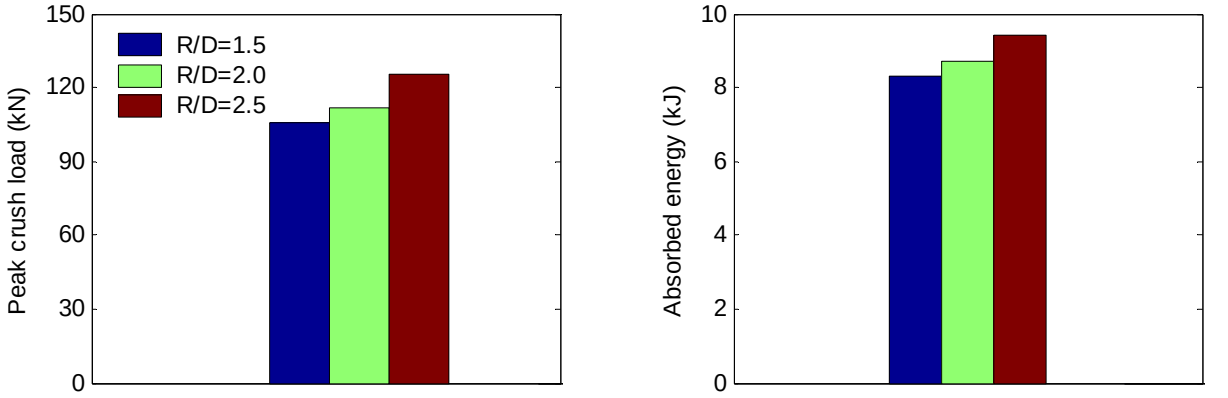

Figure 50: Peak load and energy results for hydroformed DP600 s-rails bent at R/D ratios of 1.5, 2.0, and 2.5

The reason for the minor effect of bend radius on the crash response of s-rails is most likely due to the fact that the majority of the deformation occurs near the neutral axes of the bends, with the sharpest folds within the hinge regions directly on the neutral axis. As a results, the effects of the varying degrees of residual strains, stresses, and wall thickness change – a consequence of different R/D ratios (refer to Section 4.1.4) – are minimized. The small differences in the crash responses are attributed mainly to geometric effects; as the R/D ratio decreases, the length of section C of the s-rail

(refer to Chapter 2, Figure 5) increases, resulting in a longer moment arm acting on the hinges of the s-rails and reducing the crushing loads.

4.3.5 Effect of initial material thickness on crash test results

The load-displacement and energy-displacement curves for hydroformed HSLA350 1.5 and 1.8mm s-rails bent at an R/D ratio 2.0 are shown in Figure 51. The mass-specific load-displacement and energy-displacement responses (the curves shown in Figure 51 are divided by the total mass of the structures; 5.98 kg for two HSLA350 1.5mm s-rails, and 7.22 kg for two HSLA350 1.8mm s-rails) are shown in Figure 52. The absolute and specific values of peak load and energy absorption after 300mm of crush distance are listed in Table 15; for the HSLA350 1.8mm s-rails, percentage differences are presented in parentheses with respect to the HSLA350 1.5mm s-rails. The tabulated absolute peak loads and energies are also presented graphically in Figure 53.

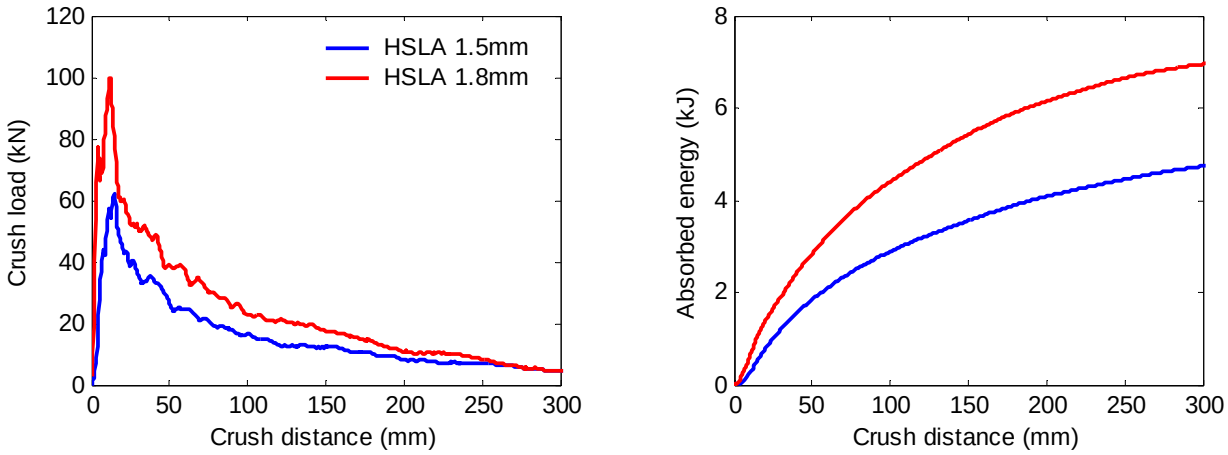

Figure 51: Crash test results for hydroformed HSLA350 1.5 and 1.8mm s-rails bent at an R/D ratio of 2.0

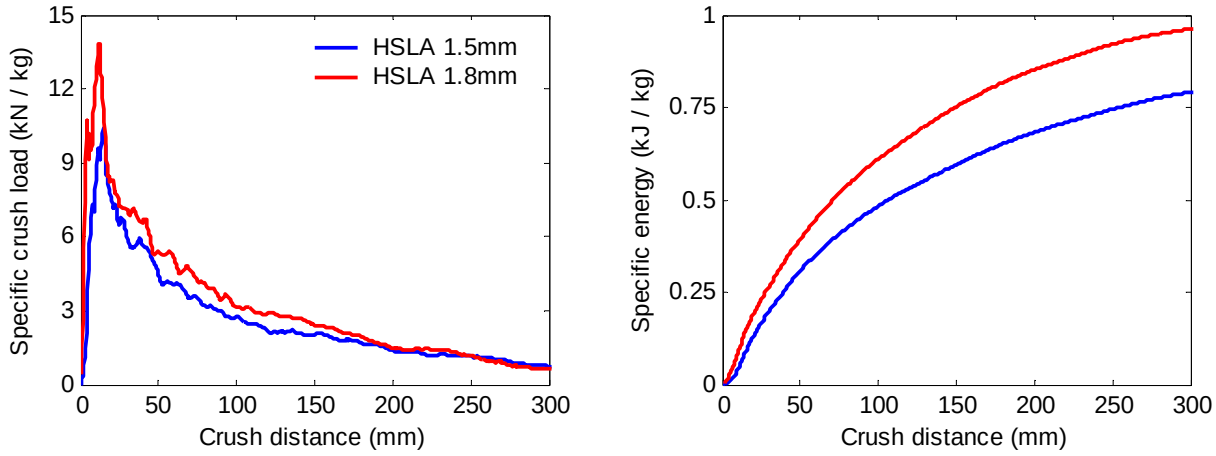

Figure 52: Mass-specific crash test results for hydroformed HSLA350 1.5 and 1.8mm s-rails bent at an R/D ratio of 2.0

Table 15: Absolute and specific peak load and energy results for hydroformed HSLA350 1.5 and 1.8mm s-rails bent at an R/D ratio of 2.0

	HSLA350 1.5mm	HSLA350 1.8mm
Peak load (kN)	62.1	99.9 (+60.9%)
Energy @ 300 mm (kJ)	4.73	6.95 (+46.9%)
Specific peak load (kN / kg)	10.4	13.9 (+33.7%)
Specific energy @ 300 mm (kJ / kg)	0.79	0.96 (+21.5%)

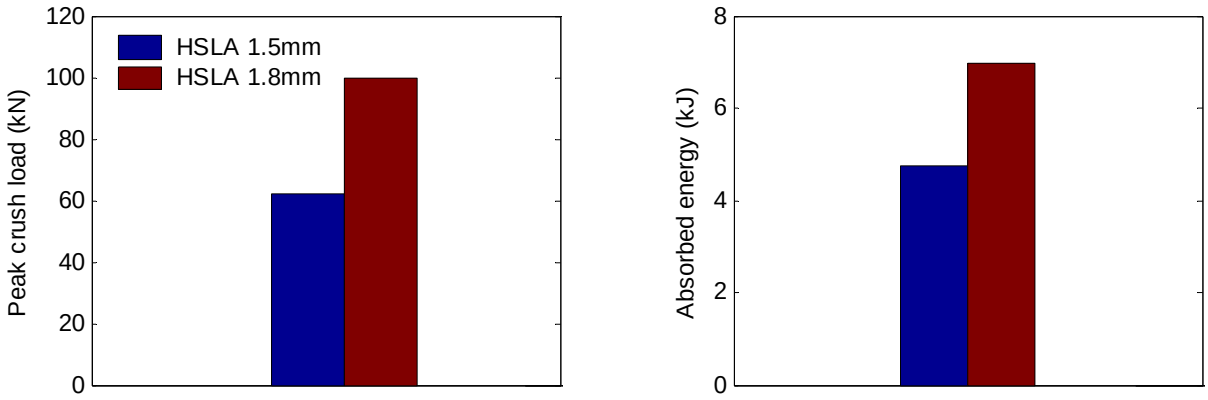

Figure 53: Peak load and energy results for hydroformed HSLA350 1.5 and 1.8mm s-rails bent at an R/D ratio of 2.0

The data shows a drastic increase of 60.9% in the peak load and 46.9% in the energy absorption of s-rails by increasing the wall thickness from 1.5mm to 1.8mm. Despite the fact that the HSLA350 1.8mm s-rails are 21% heavier than the HSLA350 1.5mm s-rails, the mass specific peak load

is 33.7% higher than the HSLA350 1.5mm s-rails, while the mass-specific energy absorption is 21.5% higher. These results indicate a non-linear relationship between wall thickness and the peak load and energy absorption responses of s-rails. This non-linear result is in accord with the findings of Oliveira *et al.* (2006), who have shown that by increasing the wall thickness of aluminum s-rails from 2.0mm to 3.5mm (an increase in mass of 71%), the peak load increases by 180%, while the energy absorption increases by 200%. The relationship between wall thickness and mass-specific energy absorption appears to be linear within the range of thicknesses examined in the current study.

4.3.6 Effect of impact velocity on crash test results

The load-displacement and energy-displacement curves for non-hydroformed HSLA350 1.8mm s-rails bent at an R/D ratio of 1.5 and impacted at 4.57 m/s and 6.46 m/s are shown in Figure 54, while the same set of results are presented in Figure 55 for hydroformed HSLA350 1.8mm s-rails bent at an R/D ratio of 1.5 and impacted at 4.57 m/s and 8.06 m/s. The peak loads measured during the test, as well as the values of absorbed energy after 300mm of crush distance are listed in Table 16; percentage differences are presented in parentheses with respect to s-rails impacted at 4.57 m/s.

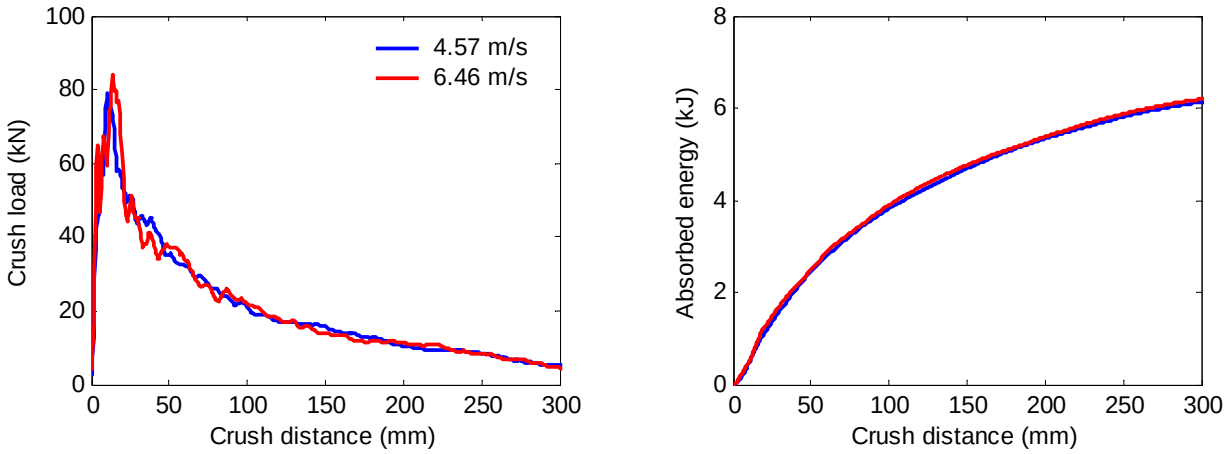

Figure 54: Crash test results for non-hydroformed HSLA350 1.8mm s-rails bent at an R/D ratio of 1.5 and impacted at 4.57 and 6.46 m/s

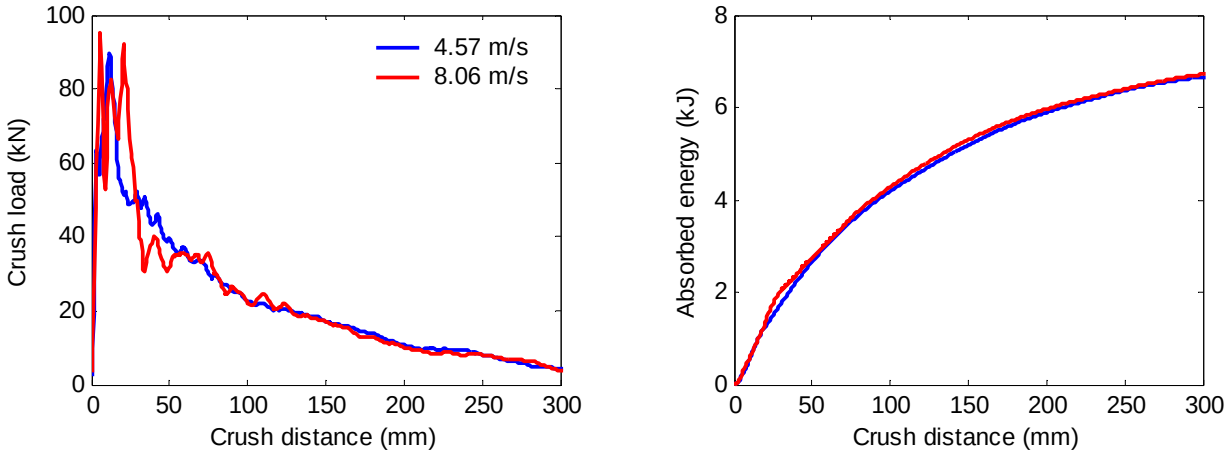

Figure 55: Crash test results for hydroformed HSLA350 1.8mm s-rails bent at an R/D ratio of 1.5 and impacted at 4.57 and 8.06 m/s

Comparison of the data between the lower velocity impacts and the higher velocity impacts indicates an increase in the peak loads by roughly 6.5%, while the energy absorption increases by roughly 1.0% at the higher impact velocities. Aside from the slightly higher peak load, the load-displacement responses shown in Figure 54 are nearly identical for the two impact velocities (4.57 m/s and 6.46 m/s), while the energy absorption responses are indistinguishable. The load-displacement response of the s-rails impacted at 8.06 m/s presented in Figure 55 shows what appears to be some ringing in the data due to the higher impact velocity during the first 60mm of displacement; once the ringing subsides at roughly 60mm of crush distance, the load-displacement responses obtained from the two impact velocities are nearly identical. This result is mirrored in the energy absorption responses, since there is a slight difference in the response of s-rails impacted at the two different velocities during the ringing, but after a crush distance of roughly 60mm, the energy absorption responses are virtually identical. These results show that within the range of the velocities used in the impact tests, there is no appreciable difference in the crash response of steel s-rails impacted at different velocities.

Due to the constraints of the impact sled and concerns regarding the integrity of the sled at higher impact velocities, tests were not performed with velocities that were drastically higher than 4.57 m/s. The Johnson-Cook constitutive material model presented in Section 3.1 suggests that a material's flow stress is logarithmically dependent on strain rate, hence differences of orders of magnitude in strain rate – and therefore differences of orders of magnitude in impact velocity – are required to substantially increase the material's flow stress during impact and significantly increase the load-displacement response of s-rails, which could not be achieved on the test apparatus available. This issue will be investigated in more detail in Chapter 5, since there are no constraints on the impact velocities that can be used in numerical models, and increases of orders of magnitude can be easily achieved.

Table 16: Peak load and energy results for HSLA350 1.8mm s-rails bent at an R/D ratio of 1.5 and impacted at 4.57, 6.46, and 8.06 m/s

	Non-hydroformed		Hydroformed	
	V = 4.57 m/s	V = 6.46 m/s	V = 4.57 m/s	V = 8.06 m/s
Peak load (kN)	79.1	84.0 (+6.2%)	89.4	95.4 (+6.7%)
Energy @ 300 mm (kJ)	6.13	6.19 (+1.0%)	6.66	6.72 (+0.9%)

Chapter 5

Numerical results

This chapter presents the results predicted by numerical simulations of tube bending, hydroforming, and crash of s-rail structures. Predicted forming process variables, crash loads, as well as strain and thickness measurements are presented, and where available, juxtaposed with the corresponding experimental results in order to assess the accuracy of the numerical models.

5.1 Tube bending predictions

5.1.1 Bending process variables

The predicted bending process variables are presented in this section alongside the measured experimental process variables in order to validate the numerical tube bending models. The predicted process variables are presented for the first bend of the s-rail only, since there are no discernable differences between the results of the first and second bends. The measured process variables are the average values from eight bends for each condition (four first bends, four second bends).

During the experiments, it was observed that a torque of 0.7 kNm was required to rotate the bend die and overcome frictional losses without actually bending a tube; it was also observed that a load of 9.2 kN was required to advance the pressure die due to losses in the system. Consequently, a constant torque value of 0.7 kNm, and a load of 9.2 kN was added to the numerical predictions of bend die torque and pressure die feed, respectively, in order to account for losses associated with the tube bender that cannot be simulated in numerical models. Since the numerical simulations are accelerated

in order to reduce computational times (refer to Section 3.2.3), the time axis of the numerical results is scaled linearly from 24 milliseconds in the models to the actual bending time of 4 seconds used in the experiments.

Predicted and measured bending process variables for DP600 bent at R/D ratios of 1.5, 2.0, and 2.5 are shown in Figure 56, Figure 57, and Figure 58, respectively. The predicted bend die torques for all three R/D ratios increase drastically at the start of the bend, and decrease drastically at the end of the bend; this is caused by the high angular acceleration and deceleration of the bend die and tube that occurs during a very short time frame in the numerical models (due to the fact that the models are artificially accelerated). In order to minimize these spikes in the predicted torque results, the mass and rotational inertias of the bend die are assigned values close to zero, however, the mass of the tube cannot be assigned arbitrarily, therefore the spikes could not be averted completely. The magnitudes of the spikes increase with R/D ratio, since increasing the distance of the tube from the rotation center increases the inertia of the rotating system, hence increasing the torque required to accelerate the mass of the tube.

The predicted bend die torque for DP600 bent at an R/D ratio of 1.5 is roughly 1.0 kNm below the measured torque for the majority of the duration of the bend, while the predicted torque at an R/D ratio of 2.0 is greater than the measured torque by roughly 0.5-1.0 kNm. The predicted torque at an R/D ratio of 2.5 drops below the measured torque by nearly 2.0 kNm after the initial spike, however, from the 2.0 to 3.5 second points of the bend, the predicted values are in excellent agreement with the measured values.

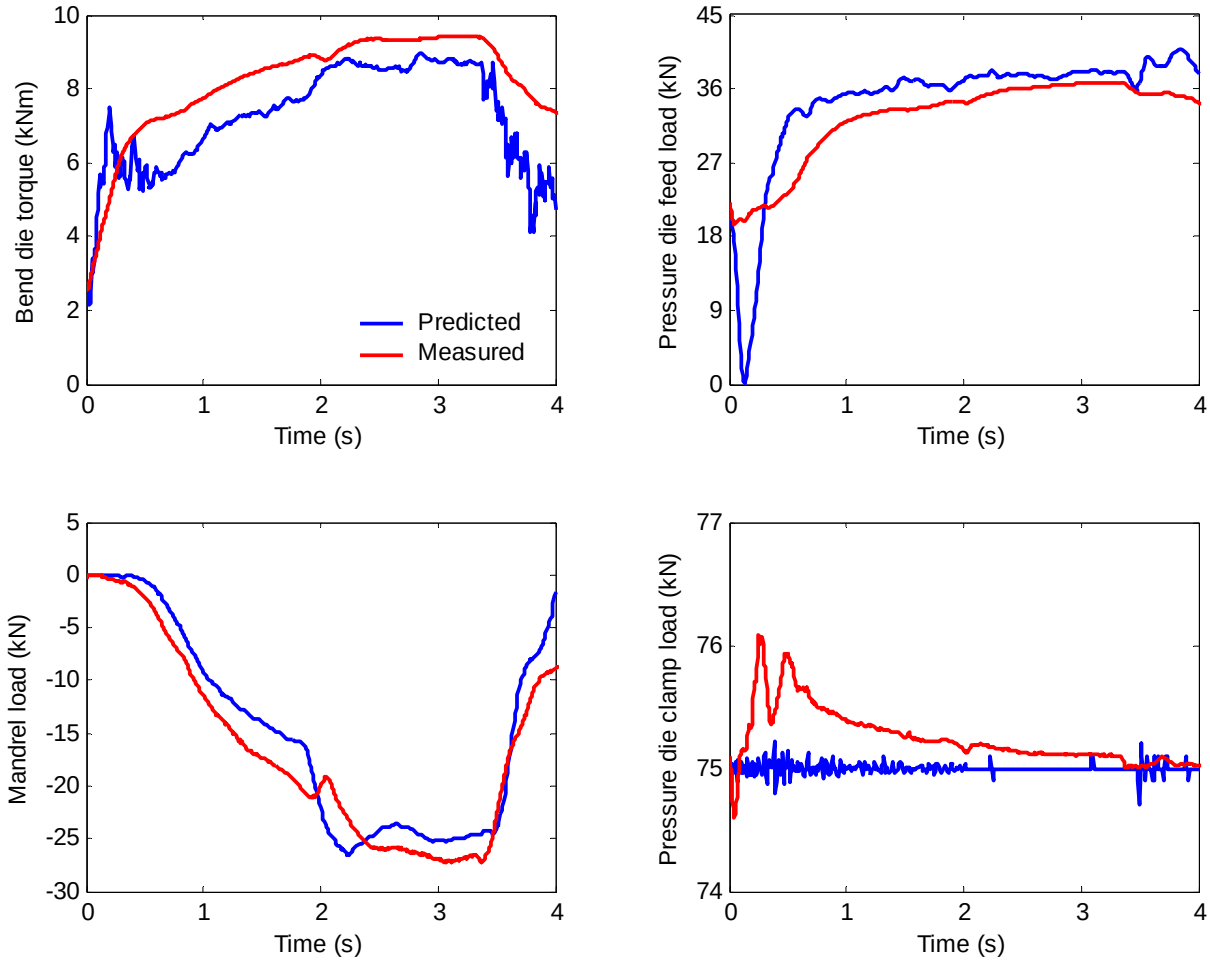

Figure 56: Predicted and measured bending process variables for DP600 bent at an R/D ratio of 1.5

The predicted pressure die feed loads for DP600 bent at the three R/D ratios are in close agreement with the measured values, especially at the R/D ratios of 2.0 and 2.5. These results validate the coefficient of friction used to simulate contact between the pressure die and tube when pine tar powder was used. The pressure die clamp loads were specified explicitly in the models, and they are shown alongside the measured values in order to illustrate that the correct clamping loads were used in the models; spikes and oscillations in the measured pressure die clamp loads cannot be simulated in the numerical models since they are dependent on the control system used in the experiments.

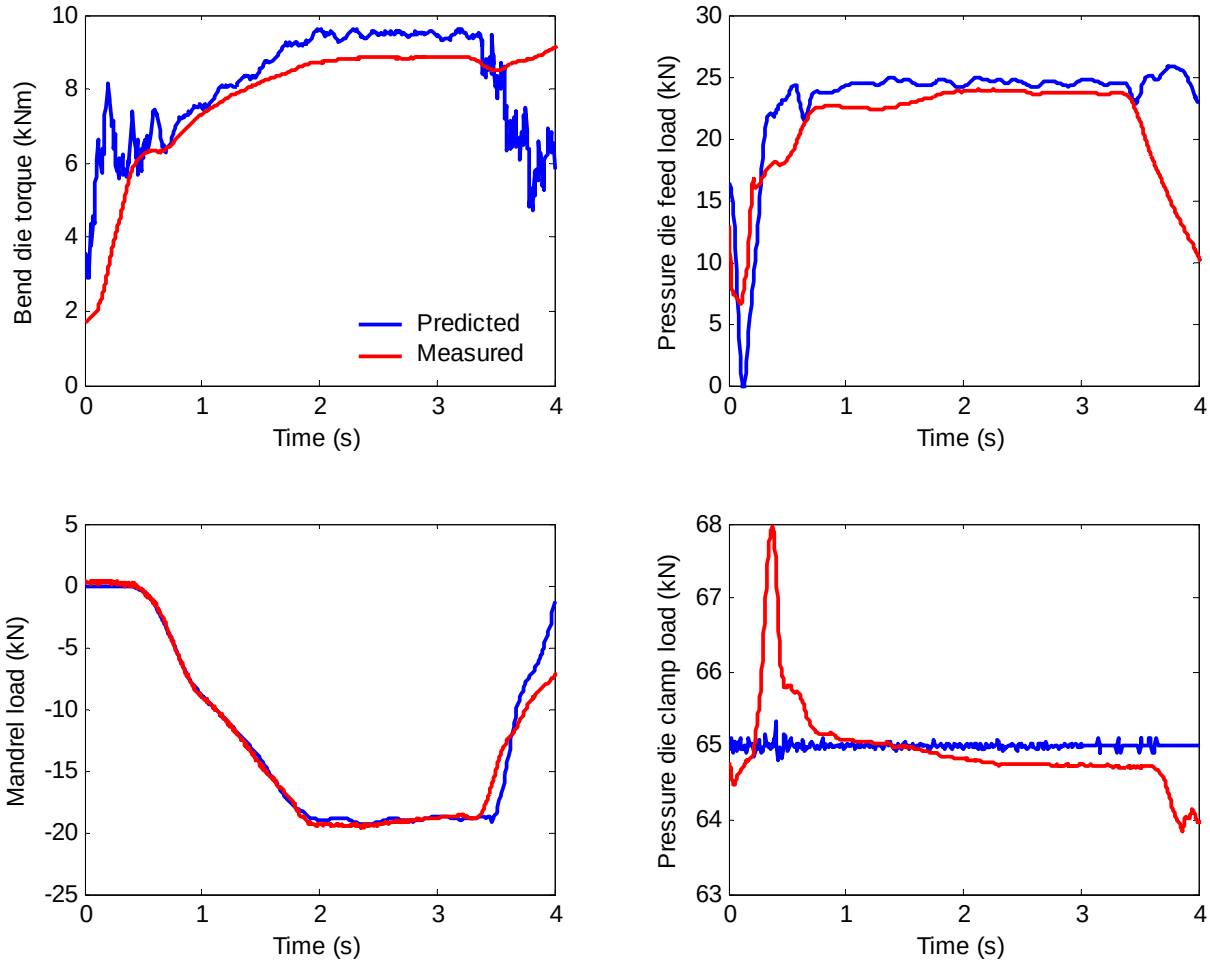

Figure 57: Predicted and measured bending process variables for DP600 bent at an R/D ratio of 2.0

The predicted mandrel loads for DP600 bent at the three R/D ratios are in excellent agreement with the measured values, particularly for the R/D ratios of 2.0 and 2.5, where the predicted loads are nearly identical to the measured loads. The overall accuracy of the predicted results presented for DP600 at the three different R/D ratios indicates that the numerical models can correctly capture the effects of R/D ratio on the bending process variables, therefore the results for the other materials will be presented only at an R/D ratio of 2.0.

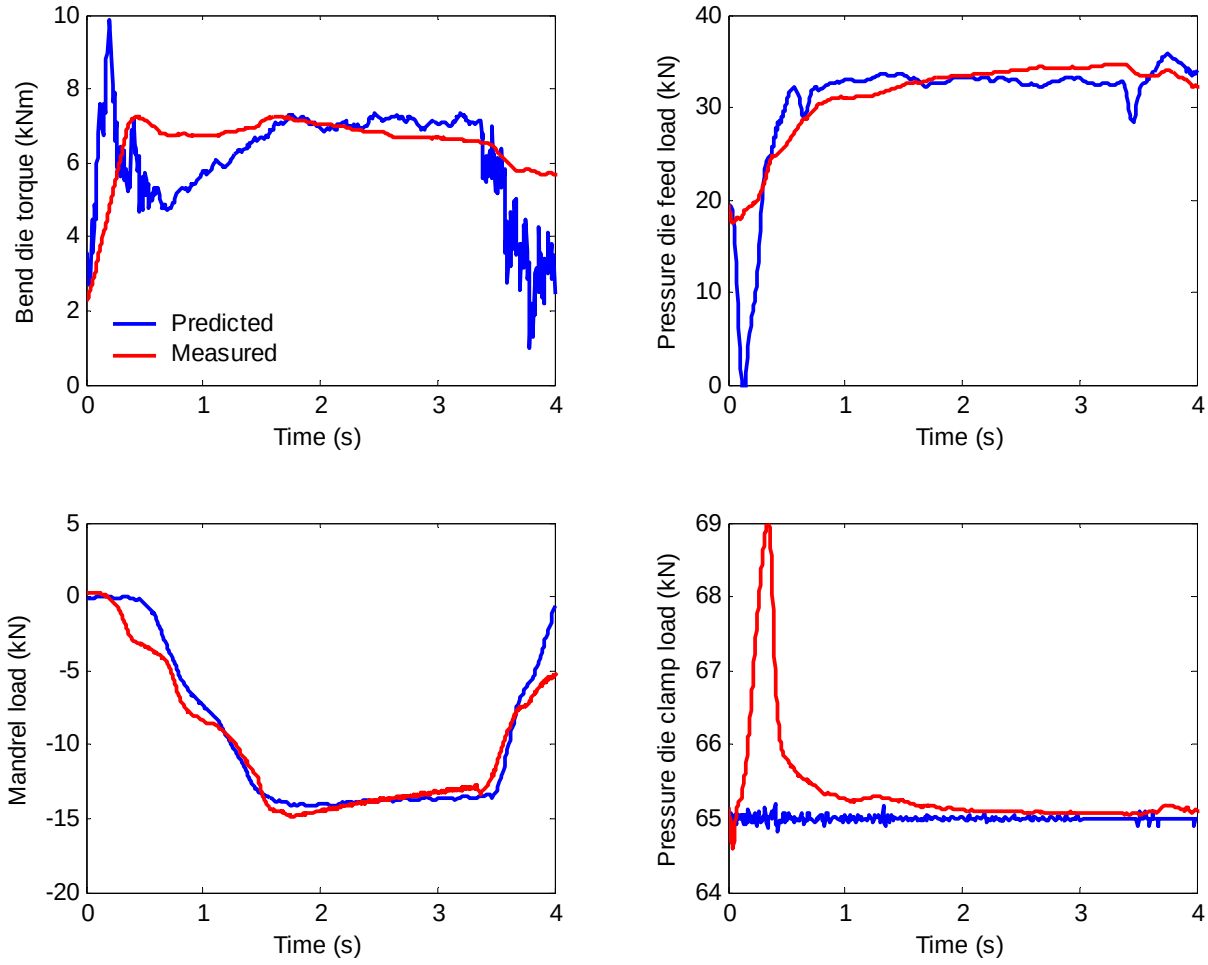

Figure 58: Predicted and measured bending process variables for DP600 bent at an R/D ratio of 2.5

Predicted and measured bending process variables for HSLA350 1.8mm bent at an R/D ratio of 2.0 are shown in Figure 59. Aside from the initial and final spikes, the predicted bend die torque is in excellent agreement with the measured experimental torque, as is the predicted pressure die feed load. The predicted mandrel loads are roughly 2.0 kN higher (lower in magnitude) than the measured values. Accurate predictions of mandrel loads are mostly dependent on the accuracy of the coefficient of friction used in the models, therefore the observed discrepancy suggests that the coefficient of friction used for contact between the HSLA350 1.8mm tubes and the mandrel is slightly erroneous.

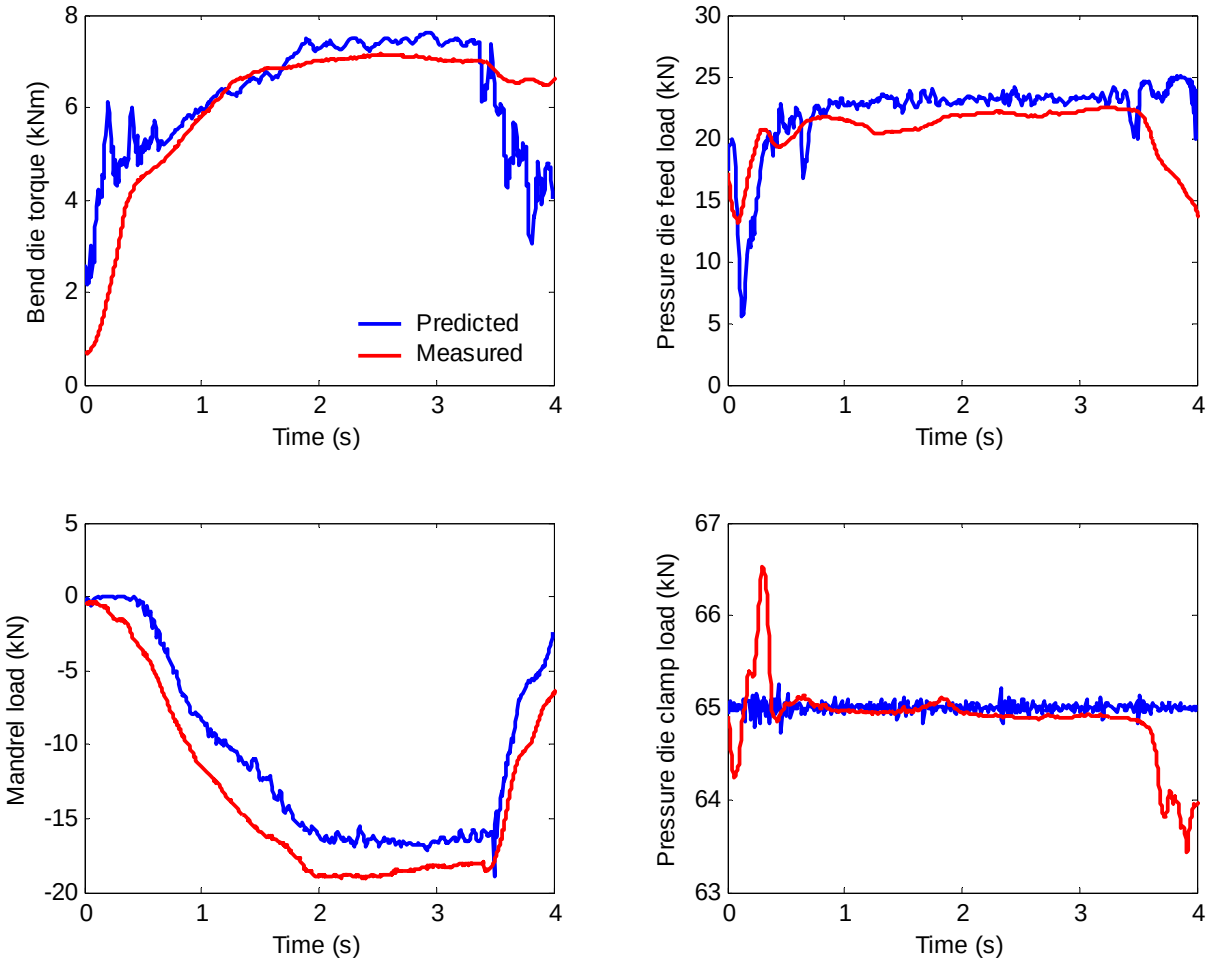

Figure 59: Predicted and measured bending process variables for HSLA350 1.8mm bent at an R/D ratio of 2.0

Predicted and measured bending process variables for HSLA350 1.5mm bent at an R/D ratio of 2.0 are shown in Figure 60. After the initial spikes, the predicted bend die torque is greater than the measured torque by nearly 1.0 kN. The predicted pressure die feed loads are as much as 5.0 kN higher than the measured loads, a discrepancy that could not be rectified. The predicted mandrel loads are roughly 4.0 kN higher (lower in magnitude) than the measured mandrel loads. Once again, the discrepancy between the predicted and measured mandrel loads suggests that the tube-to-mandrel coefficient of friction used in the models is somewhat inaccurate.

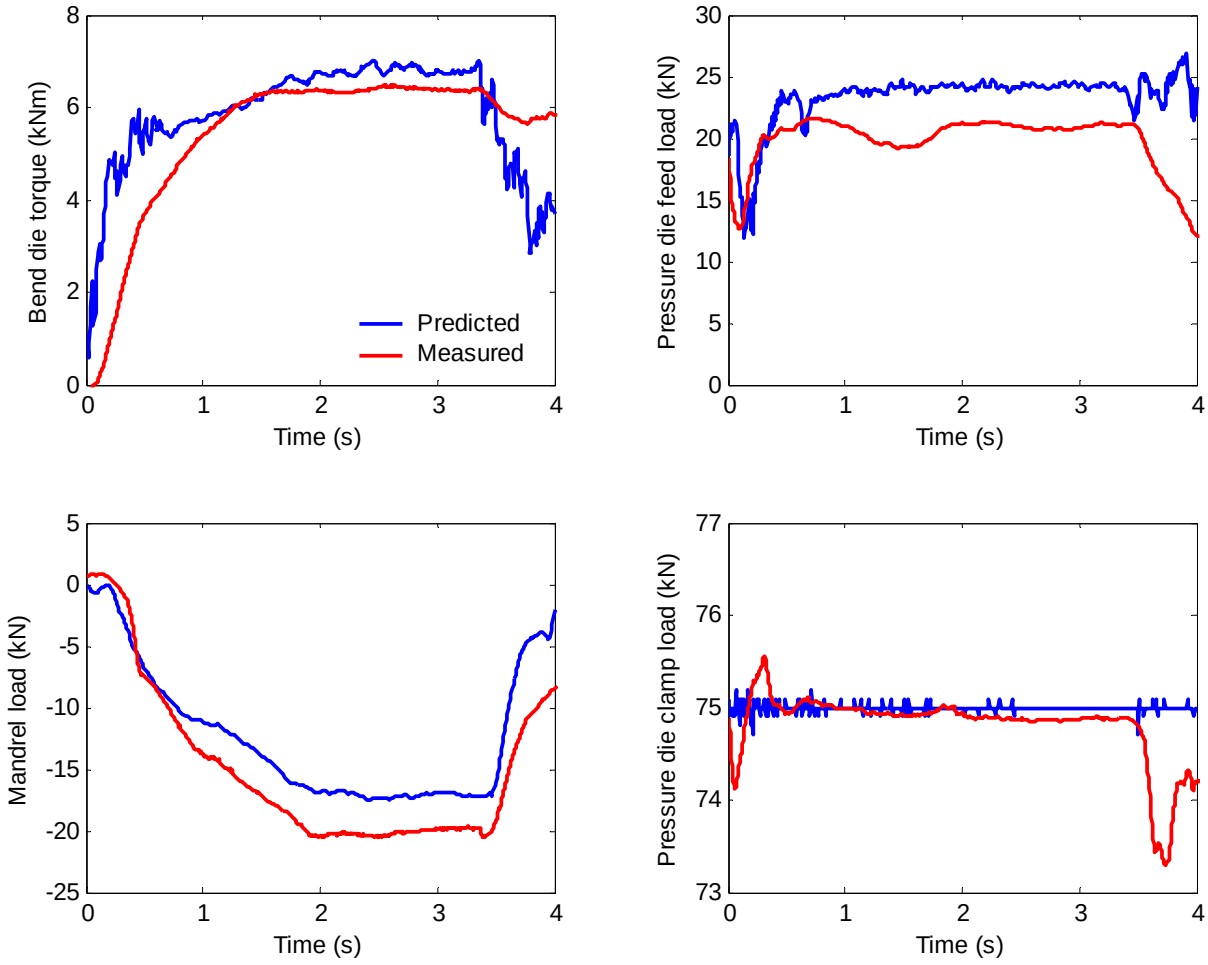

Figure 60: Predicted and measured bending process variables for HSLA350 1.5mm bent at an R/D ratio of 2.0

Predicted and measured bending process variables for DDQ bent at an R/D ratio of 2.0 are shown in Figure 61; the results for the R/D ratio of 1.5 have been omitted for brevity. The predicted bend die torque is roughly 1.5 kNm lower than the measured torque, the largest discrepancy between the predicted and measured torques of any of the materials. The predicted mandrel loads are also lower in magnitude than the measured values by the largest margin among the different materials, with a maximum discrepancy of roughly 6.0 kN. The predicted pressure die feed loads are in close agreement with the measured results, deviating from the measured values by roughly 2.0 kN. The discrepancy between the predicted and measured DDQ bending results is attributed to the use of inaccurate coefficients of friction in the numerical models, since twist compression testing was only performed for the cold-rolled materials and the hot-rolled DDQ is expected to exhibit higher coefficients of friction due to a rougher surface finish. Higher frictional loads will increase the magnitude of the predicted mandrel loads, and also increase the predictions of the bend die torque.

In general, the predicted bending process variables are in close agreement with the measured experimental values. The predictions are most accurate for the DP600 material, and the least accurate for the DDQ material. The numerical models accurately predict the effects of the different R/D ratios on the bending process variables.

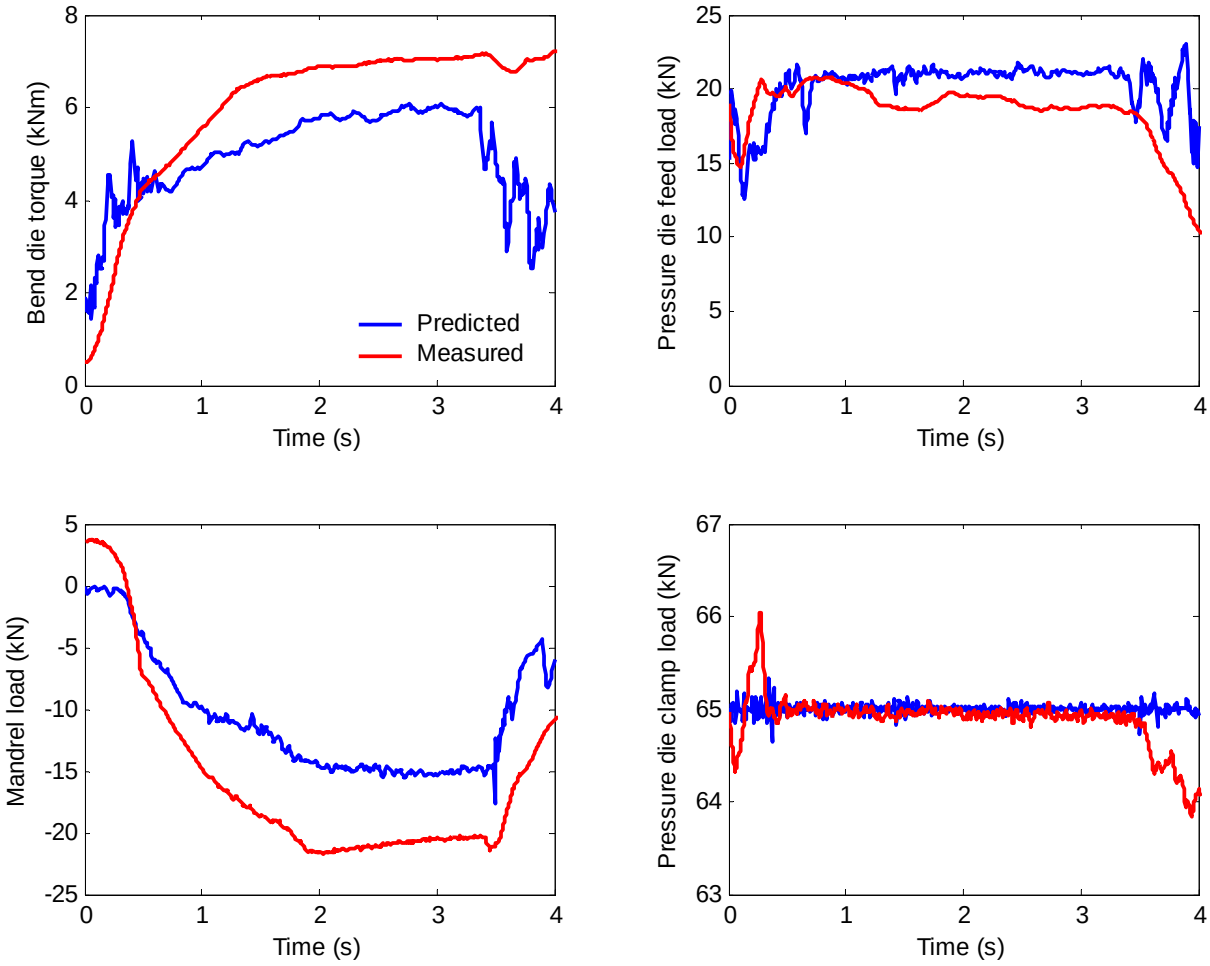

Figure 61: Predicted and measured bending process variables for DDQ bent at an R/D ratio of 2.0

5.1.2 Post-bending thickness results

A predicted contour plot of wall thickness for a DP600 s-rail bent at an R/D ratio of 2.0 is shown in Figure 62. Tube wall thinning occurs on the tensile side of the bend, while thickening occurs on the compressive side of the bend. The tube wall thickness of all other regions of the s-rail remains relatively unchanged.

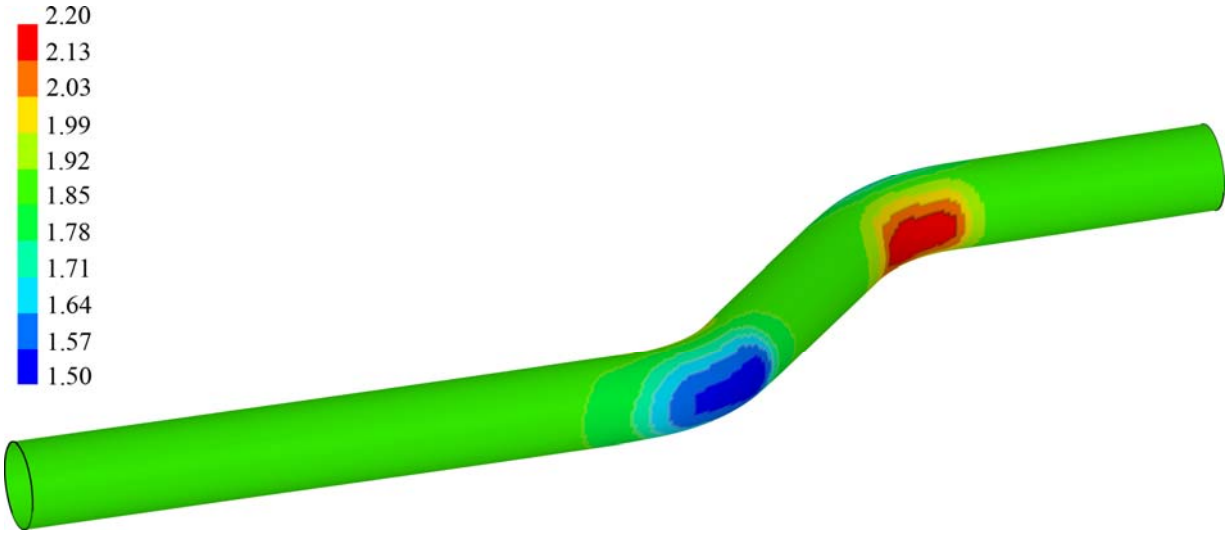

Figure 62: Predicted contours of wall thickness for a DP600 s-rail bent at an R/D ratio of 2.0 (isometric view)

Predicted and measured thickness distributions along the lower paths and around the circumferences of the first bends of DP600 s-rails bent at R/D ratios of 1.5, 2.0, and 2.5 are shown in Figure 63, Figure 64, and Figure 65, respectively. The normalizing schemes are identical to those presented in Section 4.1.2.

Predicted lower path and circumferential thickness distributions are nearly identical to the measured distributions at R/D ratios of 1.5 and 2.0, deviating by a maximum of 0.05 mm. At an R/D ratio of 2.5, the model underpredicts the wall thickness by less than 0.1 mm on the compressive side of the second bend along the lower path of the s-rail (between normalized positions of 3 and 4 in Figure 65), which is the largest discord between the predicted and measured thickness results among the DP600 s-rails. The same minute discrepancy is evident around the circumference of the DP600 s-rail bent at an R/D ratio of 2.5. Aside from these slight deviations, the numerical predictions of wall thickness distributions are in excellent accord with the measured results and accurately capture the effects of R/D ratio on the tube wall thickness distributions of s-rails, therefore forthcoming presentations of thickness distributions for the other materials will only focus on s-rails bent at an R/D ratio of 2.0.

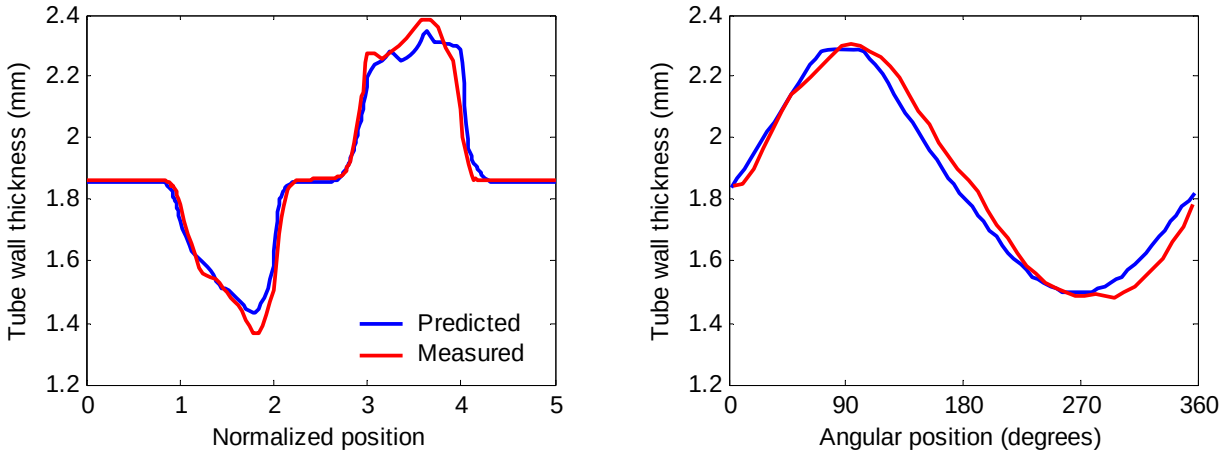

Figure 63: Predicted and measured thickness distributions for DP600 s-rails bent at an R/D ratio of 1.5

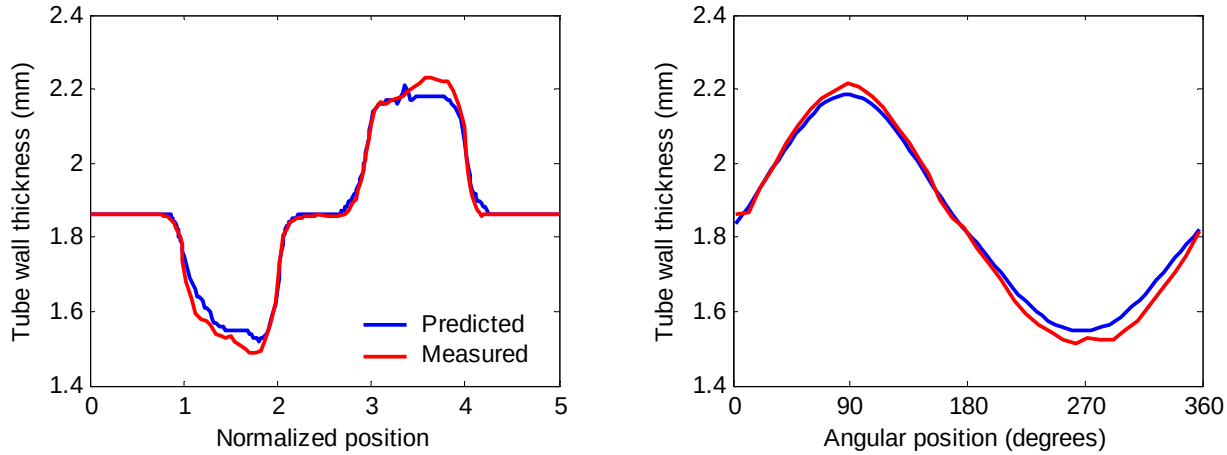

Figure 64: Predicted and measured thickness distributions for DP600 s-rails bent at an R/D ratio of 2.0

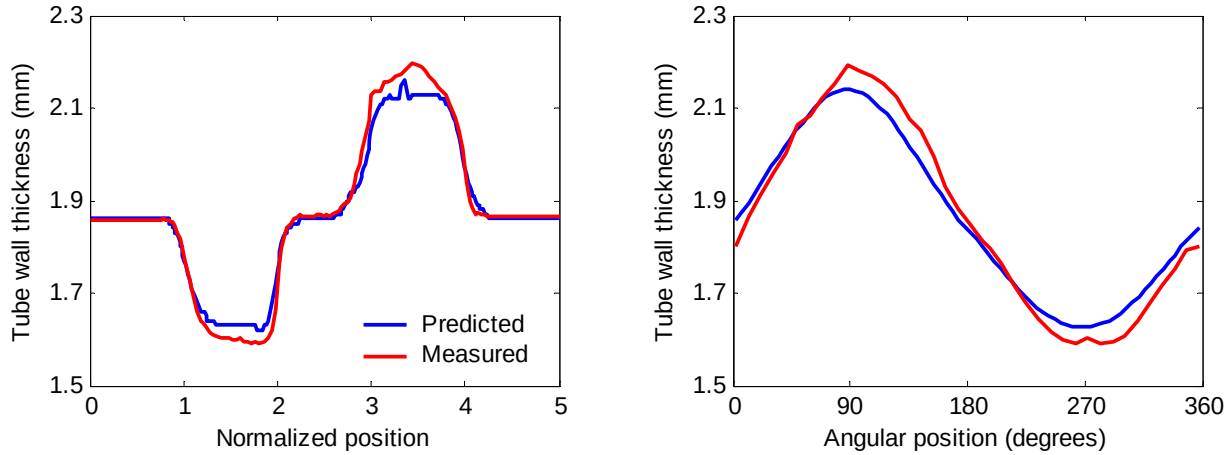

Figure 65: Predicted and measured thickness distributions for DP600 s-rails bent at an R/D ratio of 2.5

Predicted and measured thickness distributions for HSLA350 1.8 and 1.5mm s-rails bent at an R/D ratio of 2.0 are shown in Figure 66 and Figure 67, respectively. The predicted thickness distributions for the HSLA350 1.8mm s-rail are essentially identical to the measured results. A slight discrepancy between the predicted and measured results is apparent for the HSLA350 1.5mm s-rails, however, the maximum difference is below 0.1mm.

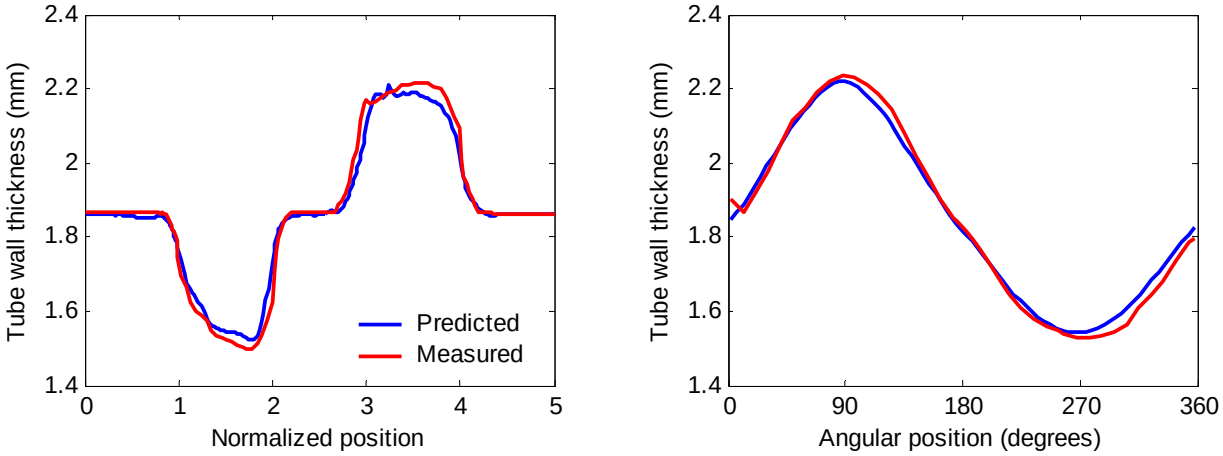

Figure 66: Predicted and measured thickness distributions for HSLA350 1.8mm s-rails bent at an R/D ratio of 2.0

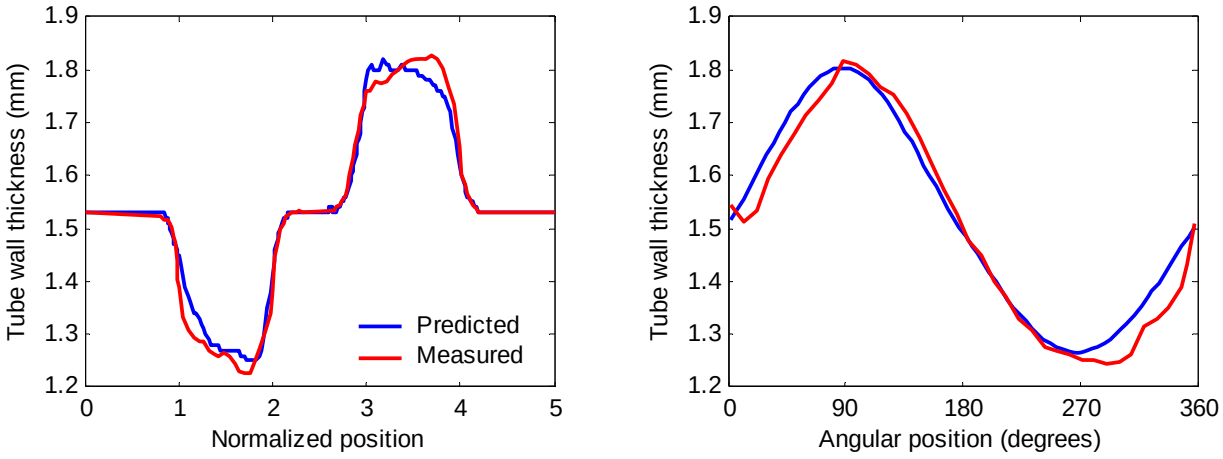

Figure 67: Predicted and measured thickness distributions for HSLA350 1.5mm s-rails bent at an R/D ratio of 2.0

Predicted and measured thickness distributions for DDQ s-rails bent at an R/D ratio of 2.0 are shown in Figure 68. On the tensile side of the first bend along the lower path of the s-rail (between normalized positions of 1 and 2) the numerical model overpredicts the wall thickness by roughly

0.05mm, while the predicted wall thickness is nearly identical to the measured values at all other locations along the lower path of the s-rail. The greatest discord between the predicted and measured thickness results of s-rails occurs in the circumferential thickness distributions of DDQ s-rails bent at an R/D ratio of 2.0; as shown in Figure 68, the predicted wall thickness values are roughly 0.15mm higher than the measured values on the compressive side of the bend, and roughly 0.1mm higher on the tensile side of the bend. Aside from this minor inaccuracy, which could not be rectified, the numerical predictions are nearly identical to the measured wall thickness distributions for all of the different materials and R/D ratios.

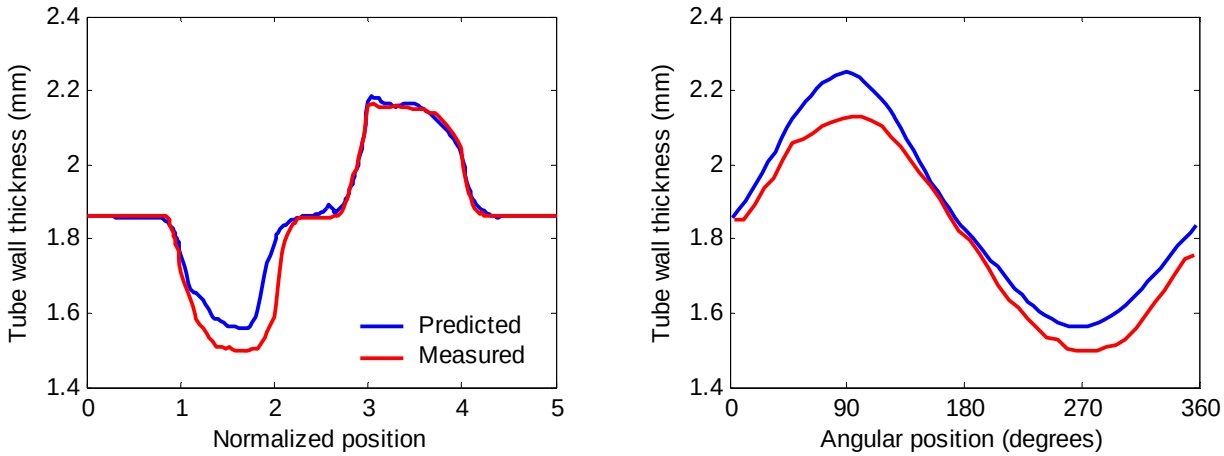

Figure 68: Predicted and measured thickness distributions for DDQ s-rails bent at an R/D ratio of 2.0

5.1.3 Post-bending strain results

Predicted contours of major, minor, and effective plastic strain for DP600 s-rails bent at an R/D ratio of 2.0 are presented in Figure 69, Figure 70, and Figure 71, respectively. The contours of major and minor strain give a more lucid description of the post-bending strains than the forthcoming strain distributions. Examination of Figure 71 indicates that the effective plastic strains within the bend regions of s-rails bent at an R/D ratio of 2.0 exceed 30%, while the straight sections of the as-bent s-rails are predicted to be nearly free of plastic deformation.

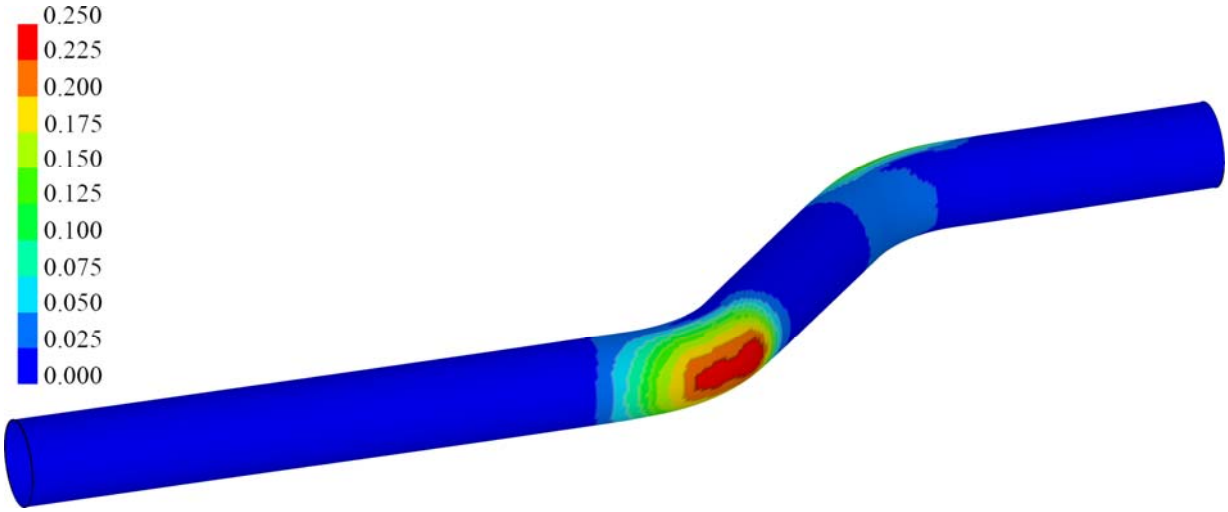

Figure 69: Predicted contours of major strain for a DP600 s-rail bent at an R/D ratio of 2.0 (isometric view)

Figure 70: Predicted contours of minor strain for a DP600 s-rail bent at an R/D ratio of 2.0 (isometric view)

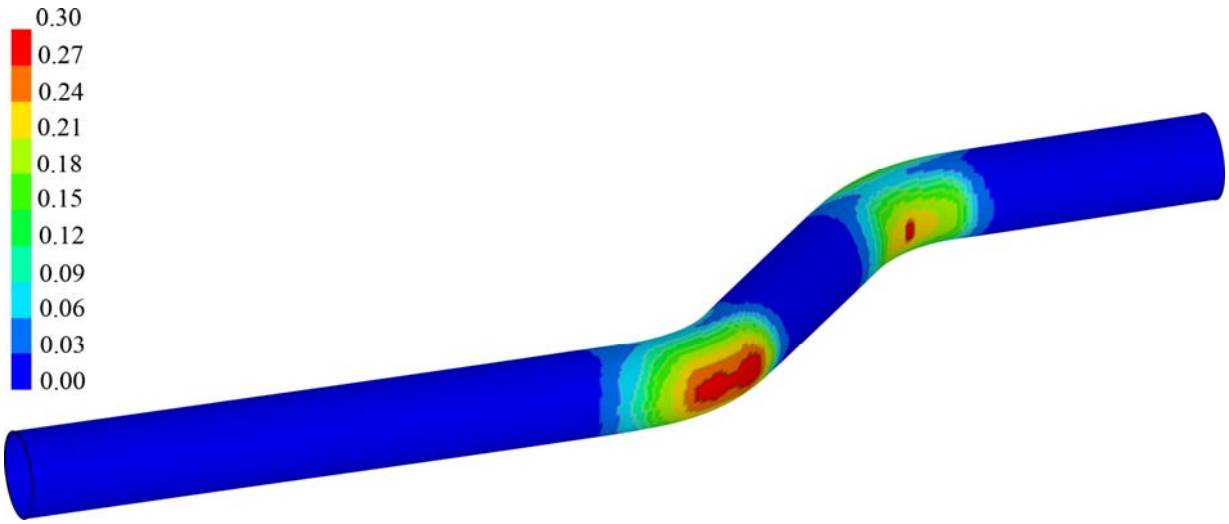

Figure 71: Predicted contours of effective plastic strain for a DP600 s-rail bent at an R/D ratio of 2.0 (isometric view)

Figure 72 presents the predicted and measured strain distributions for HSLA350 1.5mm s-rails bent at an R/D ratio of 2.0. The predicted major and minor strains along the lower path and around the circumference of the first bend are in excellent agreement with the measured strains, aside from oscillations in the measured strains that are a consequence of measurement error.

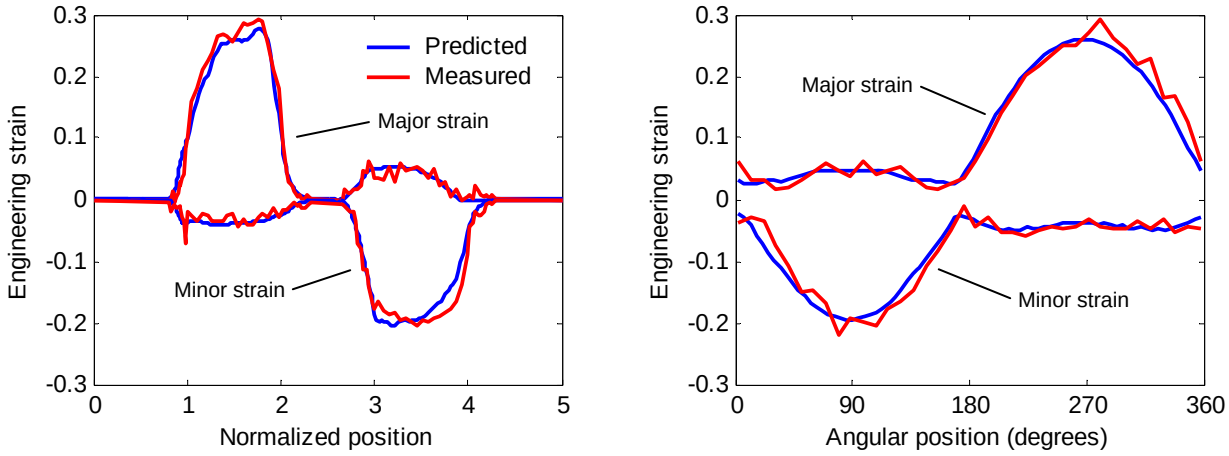

Figure 72: Predicted and measured strain distributions for HSLA350 1.5mm s-rails bent at an R/D ratio of 2.0

Predicted and measured strain distributions for HSLA350 1.8mm s-rails bent at an R/D ratio of 2.0 are presented in Figure 73. As discussed in Section 4.1.5, the grids on the compressive side of the second bend (between normalized positions of 3 and 4) were damaged and nearly indiscernible due to

friction with the wiper die, therefore measured results are presented only for the tensile side of the first bend (between normalized positions 1 and 2). The close agreement between the predicted and measured strains on the tensile side of the first bend suggests that the entire predicted lower path strain distribution is an accurate representation of the actual strains induced on the HSLA350 1.8mm s-rails during bending. The predicted strains are also in close agreement with the measured strains around the circumference of the first bend. Based on the results presented in Figure 72 and Figure 73, it is clear that the numerical models accurately predict the strain distributions within the s-rails after bending.

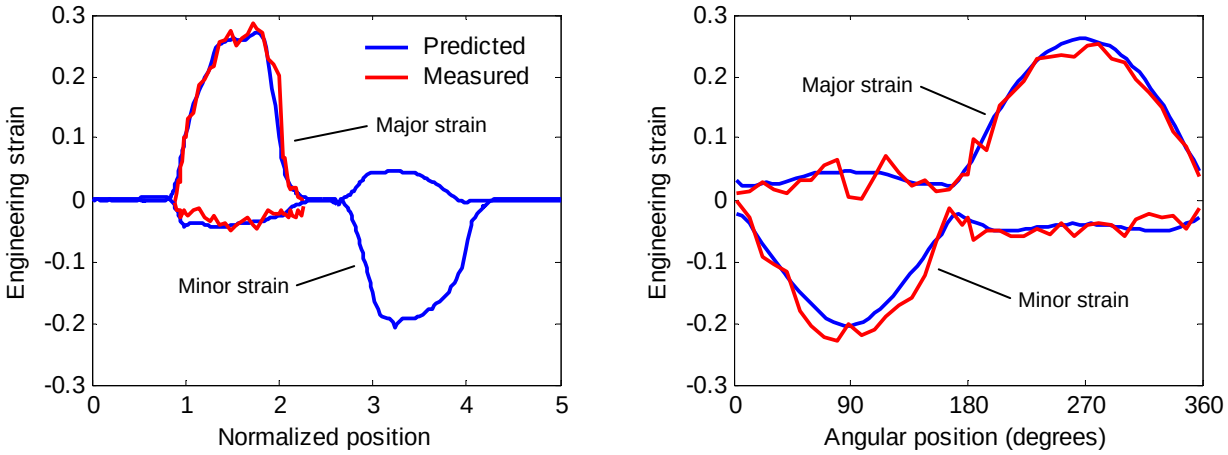

Figure 73: Predicted and measured strain distributions for HSLA350 1.8mm s-rails bent at an R/D ratio of 2.0

Since strain measurements were not conducted on DP600 or DDQ s-rails due to the time consuming nature of the work, the predicted strain distributions for s-rails made from these materials are shown in Figure 74 and Figure 75. Figure 74 presents the predicted strain distributions of DP600 s-rails at R/D ratios of 1.5, 2.0, and 2.5. The major strain increases with decreasing R/D ratio on the tensile side of the bend, while the minor strain decreases with decreasing R/D ratio on the compressive side of the bend, which are both expected results. Due to the nearly plane strain nature of the deformation state of tube bending, these results could also be inferred from the conclusions of Section 4.1.4 (increasing wall thickness change with decreasing R/D ratio).

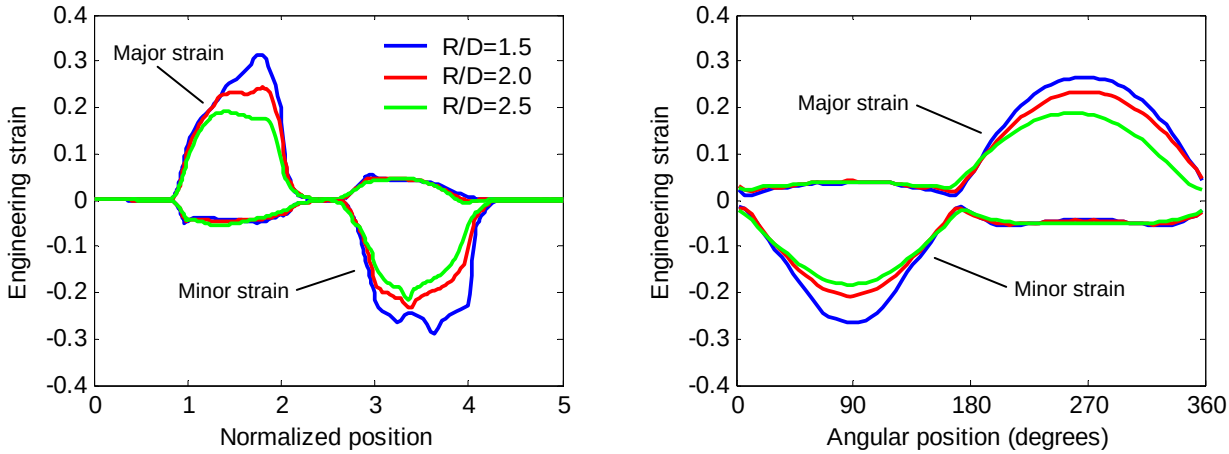

Figure 74: Predicted strain distributions for DP600 s-rails bent at R/D ratios of 1.5, 2.0, and 2.5

Figure 75 presents the predicted strain distributions for DDQ, HSLA350 1.8mm, and DP600 s-rails bent at an R/D ratio of 2.0. The maximum discrepancy in the results for the three materials is roughly 7% strain, therefore it is concluded that material strength has only a minor effect on the strain distributions of as-bent s-rails; once again, this result could also be inferred from the conclusions of Section 4.1.3 (material strength has little effect on the thickness distributions of s-rails).

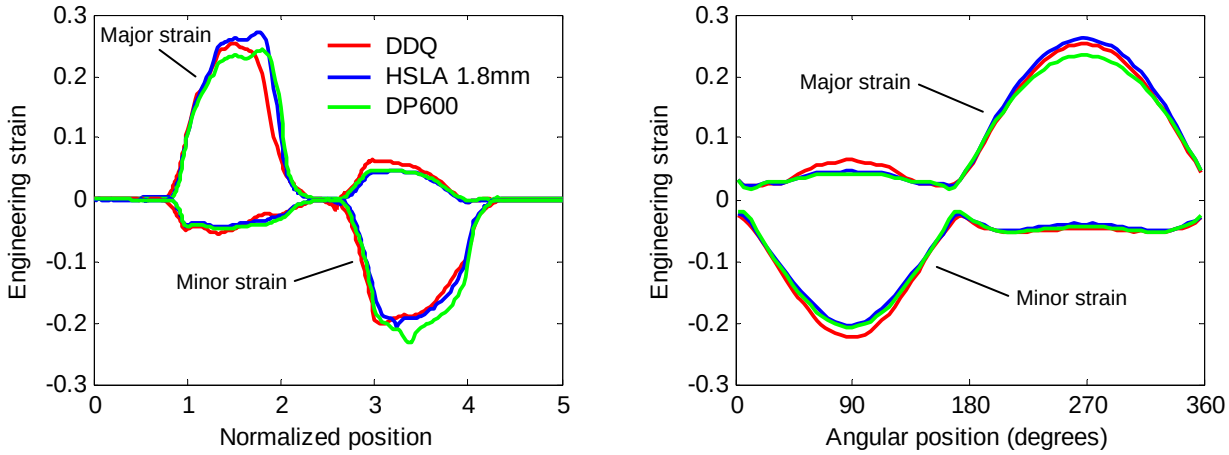

Figure 75: Predicted strain distributions for DDQ, HSLA350 1.8mm, and DP600 s-rails bent at an R/D ratio of 2.0

5.2 Hydroforming predictions

5.2.1 Post-hydroforming thickness results

A predicted contour plot of wall thickness for a hydroformed DP600 s-rail bent at an R/D ratio of 2.0 is shown in Figure 76. The contours of wall thickness for a hydroformed s-rail appear very similar to the contours presented in Figure 62 for a non-hydroformed s-rail, which is an expected result based on the conclusions of Section 4.2.2 (low-pressure hydroforming does not appreciably change the wall thickness of s-rails). This fact is further illustrated in Figure 77, which shows the thickness distribution around a straight section of a hydroformed DP600 s-rail. The thickness around the straight section lies between the original value of 1.860 mm and a minimum value of 1.844 mm in the corners of the cross-section, a reduction of less than 1%.

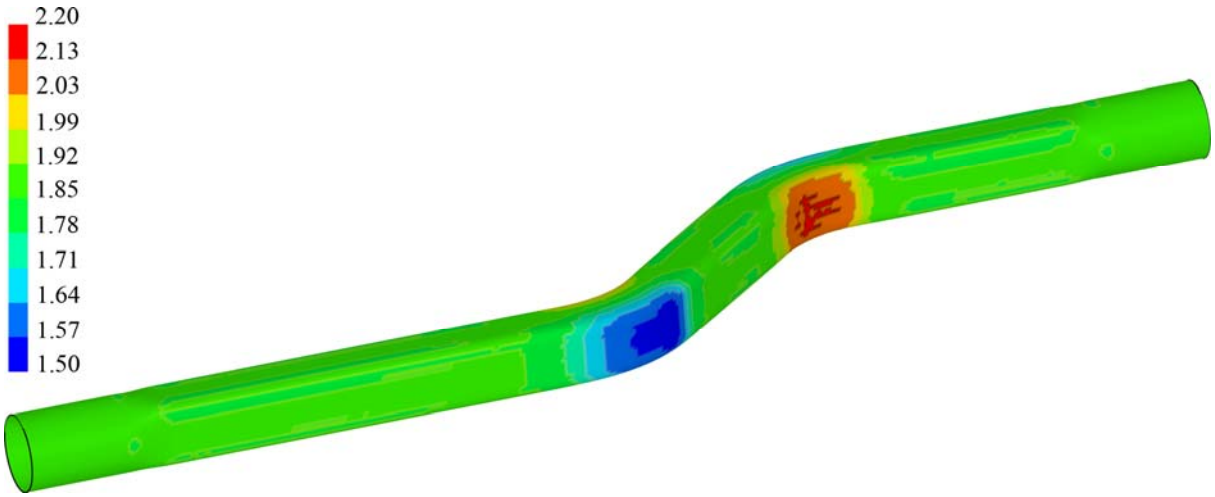

Figure 76: Predicted contours of wall thickness for a hydroformed DP600 s-rail bent at an R/D ratio of 2.0

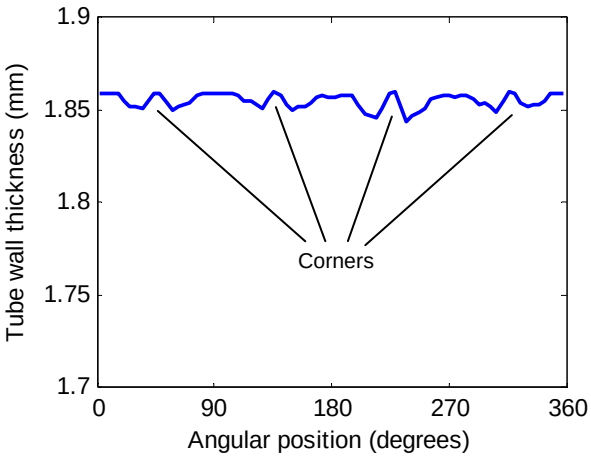

Figure 77: Predicted thickness distribution around the perimeter of a straight section of a hydroformed DP600 s-rail

Predicted and measured thickness distributions around the circumferences of hydroformed DDQ, HSLA350 1.5mm, HSLA350 1.8mm, and DP600 s-rails bent at an R/D ratio of 2.0 are shown in Figure 78. The predicted wall thickness distributions for HSLA350 1.8mm and DP600 s-rails are in excellent agreement with the measured results. The predicted results for the HSLA350 1.5mm s-rails are also in close agreement with measurements, deviating from the measured values by less than 0.1mm. The predictions for the DDQ s-rails are the least accurate of all the materials with a maximum discrepancy of 0.15mm between the predicted and measured values; this result is actually a consequence of the inaccuracy in the thickness predictions from the bending simulations, as previously shown in Figure 68. Aside from this discrepancy, it is clear that the thickness predictions derived from hydroforming simulations are in close accord with the measured results.

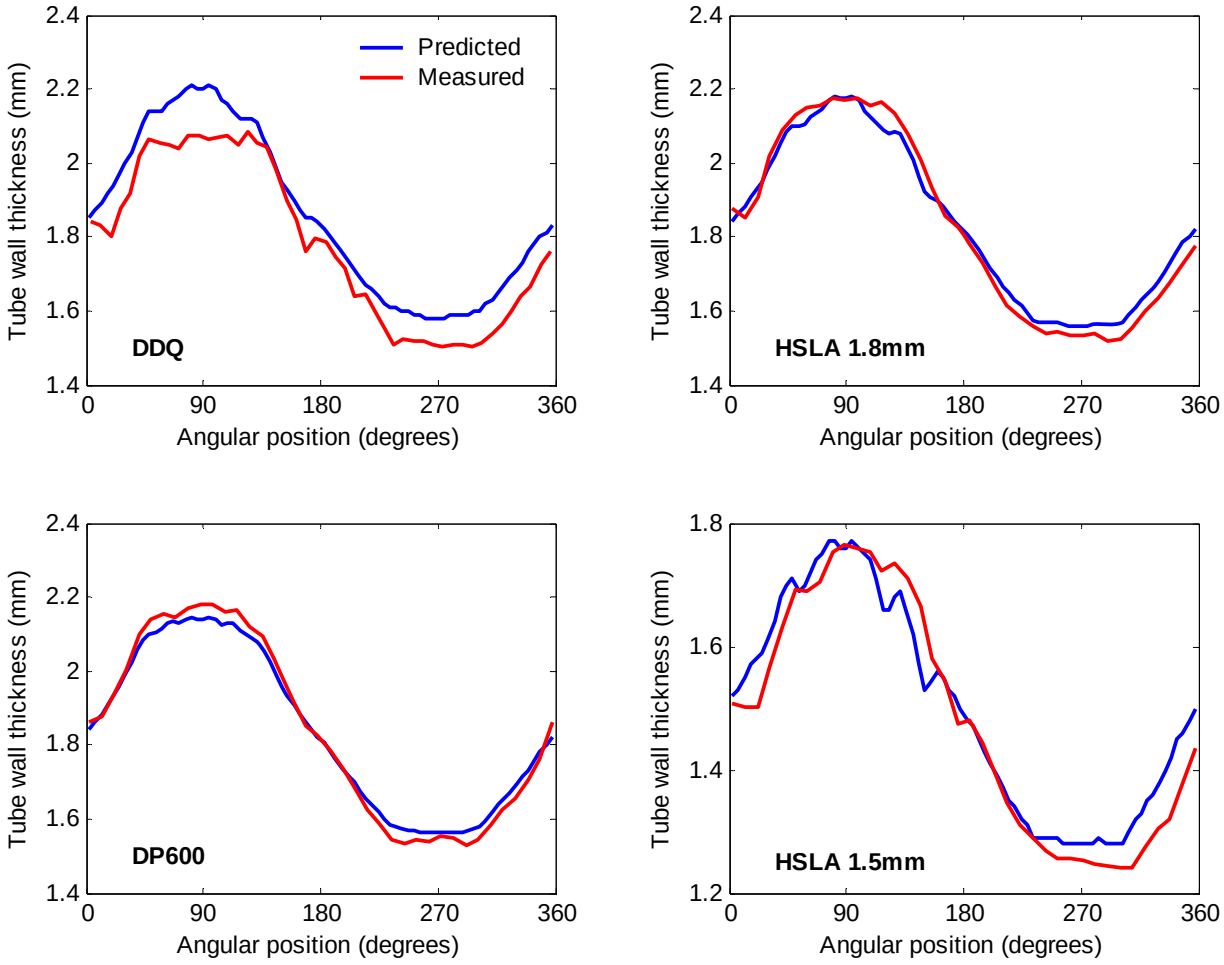

Figure 78: Predicted and measured post-hydroforming thickness distributions for DDQ, HSLA350 1.8mm, DP600, and HSLA350 1.5mm s-rails bent at an R/D ratio of 2.0

5.2.2 Post-hydroforming strain results

Predicted contours of major, minor, and effective plastic strain for hydroformed DP600 s-rails bent at an R/D ratio of 2.0 are presented in Figure 79, Figure 80, and Figure 81, respectively. There is a marked change in the strain contours of hydroformed s-rails compared to those of non-hydroformed s-rails (shown in Figure 69, Figure 70, and Figure 71), most notably along the corners of the cross-section where the majority of deformation occurs during hydroforming.

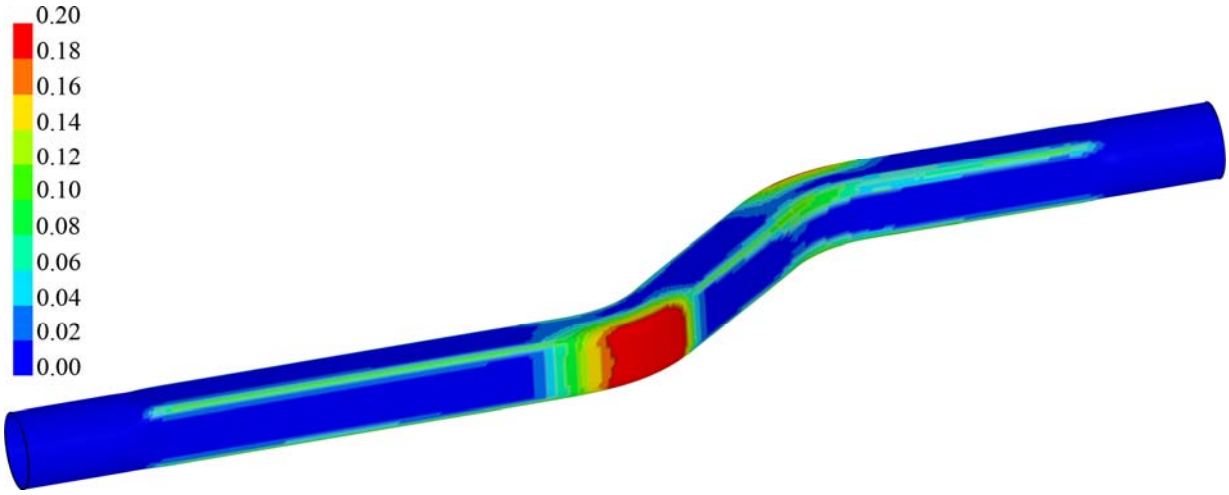

Figure 79: Predicted contours of major strain for a hydroformed DP600 s-rail bent at an R/D ratio of 2.0

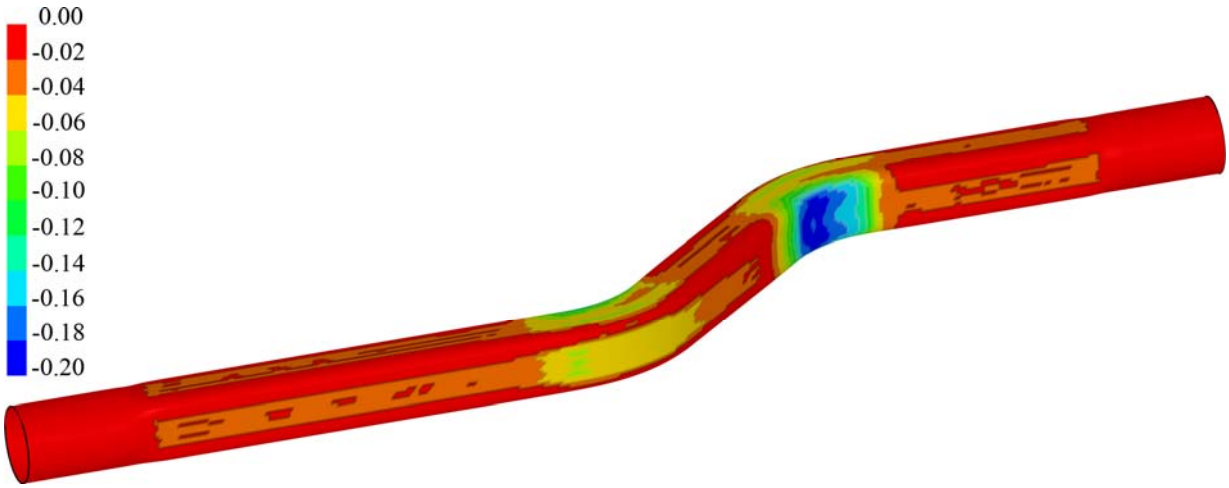

Figure 80: Predicted contours of minor strain for a hydroformed DP600 s-rail bent at an R/D ratio of 2.0

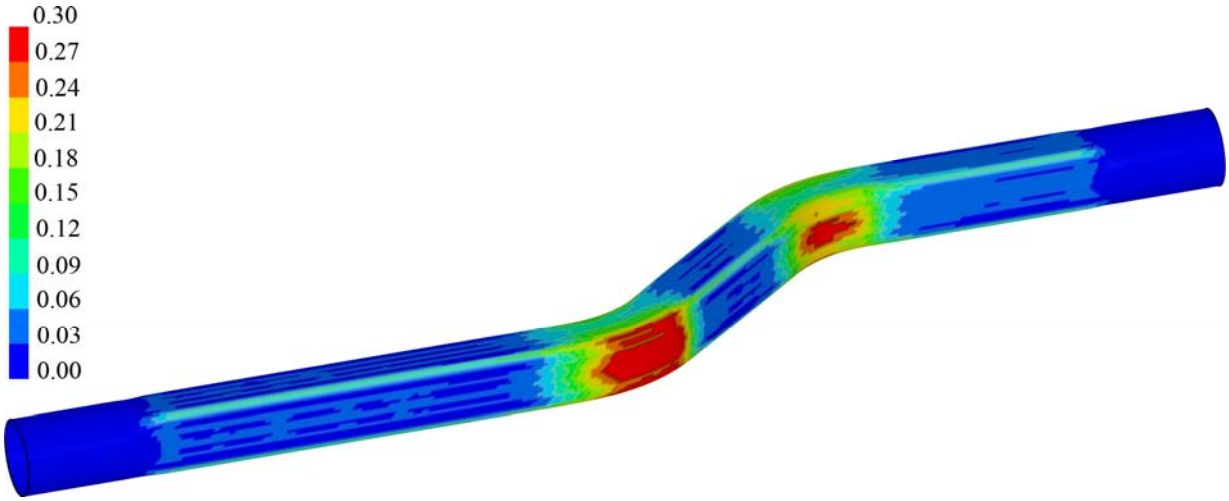

Figure 81: Predicted contours of effective plastic strain for a hydroformed DP600 s-rail bent at an R/D ratio of 2.0

Predicted and measured strain distributions around the circumferences of HSLA350 1.5 and 1.8mm s-rails are presented in Figure 82. The maximum discrepancy between the predicted and measured strains is 5% strain, which is slightly greater than the estimated measurement error associated with the strain measurements. Disregarding the inherent oscillations in the measured results, the predicted strains are in close agreement with the measured strains for both thickness gauges of the HSLA350 material. Based on these results, it is clear that the numerical models accurately predict the strain distributions of s-rails after hydroforming.

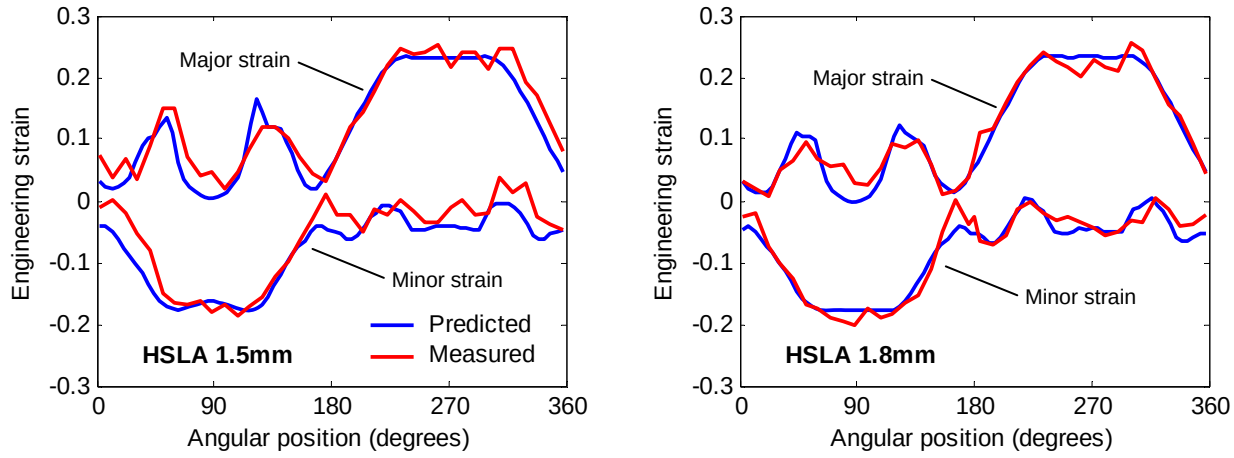

Figure 82: Predicted and measured post-hydroforming strain distributions for HSLA350 1.5 and 1.8mm s-rails bent at an R/D ratio of 2.0

Since strain measurements were not conducted on DDQ and DP600 s-rails, only the predicted circumferential strain distributions for hydroformed DDQ, HSLA350 1.8mm, and DP600 s-rails are presented in Figure 83. The results indicate that material strength has virtually no effect (5% strain at most) on the strain distributions of hydroformed s-rails (using the low-pressure process), a conclusion that could also be derived based on the observations of Section 4.2.3 (material strength has a negligible effect on the thickness distributions of hydroformed s-rails).

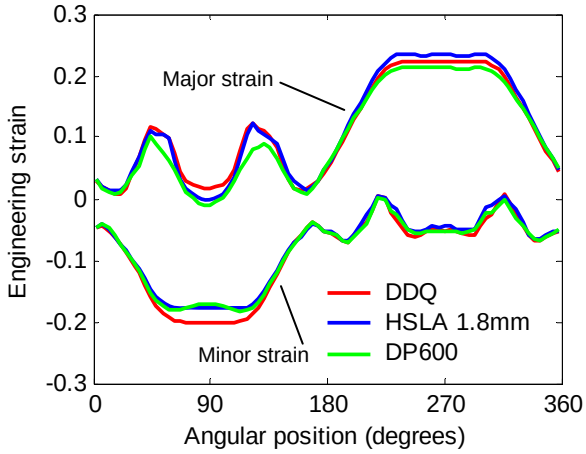

Figure 83: Predicted and measured post-hydroforming strain distributions for DDQ, HSLA350 1.8mm, and DP600 s-rails bent at an R/D ratio of 2.0

Figure 84 shows the predicted major and minor strains around a bend region of a non-hydroformed s-rail, along with the strains around a straight section (strain measurements were not conducted around the straight sections of s-rails) and a bend section of a hydroformed s-rail. Four distinct peaks occur at the corners of the cross-section within the straight region, where the major strains reach approximately 7%. The three plots illustrate that the post-hydroforming strains around a bend section of an s-rail are essentially the result of superimposing the post-bending strains around a bend section upon the post-hydroforming strains around a straight section.

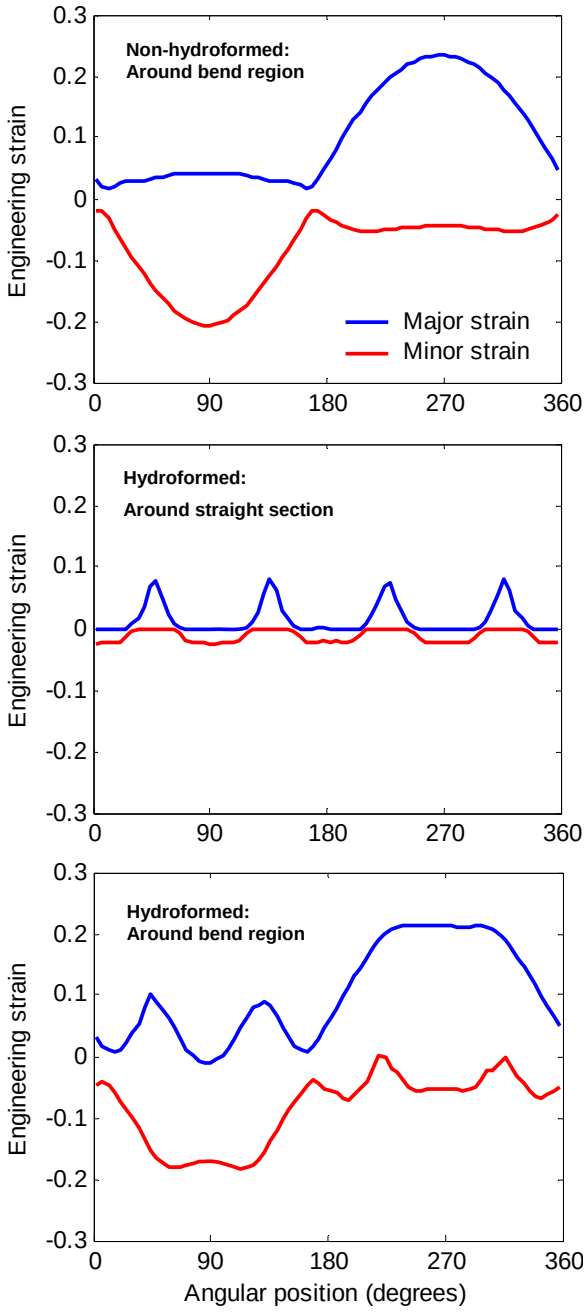

Figure 84: Predicted major and minor strain distributions around the circumference of a bent region of a non-hydroformed s-rail, around the perimeter of a straight section of a hydroformed s-rail, and around the perimeter of a bent region of a hydroformed s-rail

5.3 Crash predictions

5.3.1 Crash results – deformed shapes

The predicted shapes of crushed non-hydroformed and hydroformed s-rails, along with those of the actual s-rails from the crash experiments, are presented in this section in order to assess the accuracy of the models in predicting the deformed geometries of s-rails after crash. The deformed geometries for non-hydroformed and hydroformed DP600 s-rails bent at an R/D ratio of 2.0 are shown in Figure 85 and Figure 86, respectively. For both types of s-rails, the numerical models accurately predict the overall shapes of the deformed s-rails, as well as the sharp folds that occur at the three plastic hinges. Effective plastic strains are predicted to exceed 50% in the plastic hinge regions of non-hydroformed and hydroformed s-rails, and locally at the sharp corners of the hinges, the predicted effective plastic strains exceed 100%. These high levels of effective plastic strain are incurred under a bending mode of deformation, hence material fracture does not occur. The predicted deformation of DP600 s-rails bent at the other R/D ratios, as well as the deformation of the DDQ, HSLA350 1.5 and 1.8mm s-rails are also in close agreement with the actual deformed shapes (not shown for brevity).

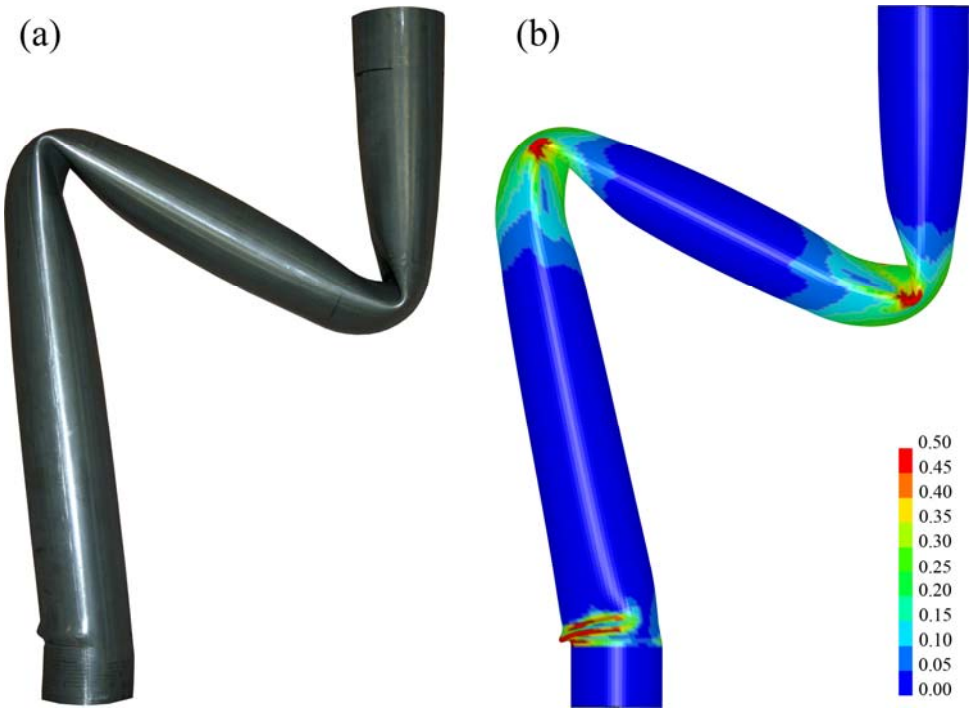

Figure 85: Juxtaposition of (a) actual and (b) predicted deformed geometry of non-hydroformed DP600 s-rails bent at an R/D ratio of 2.0 with contours of effective plastic strain

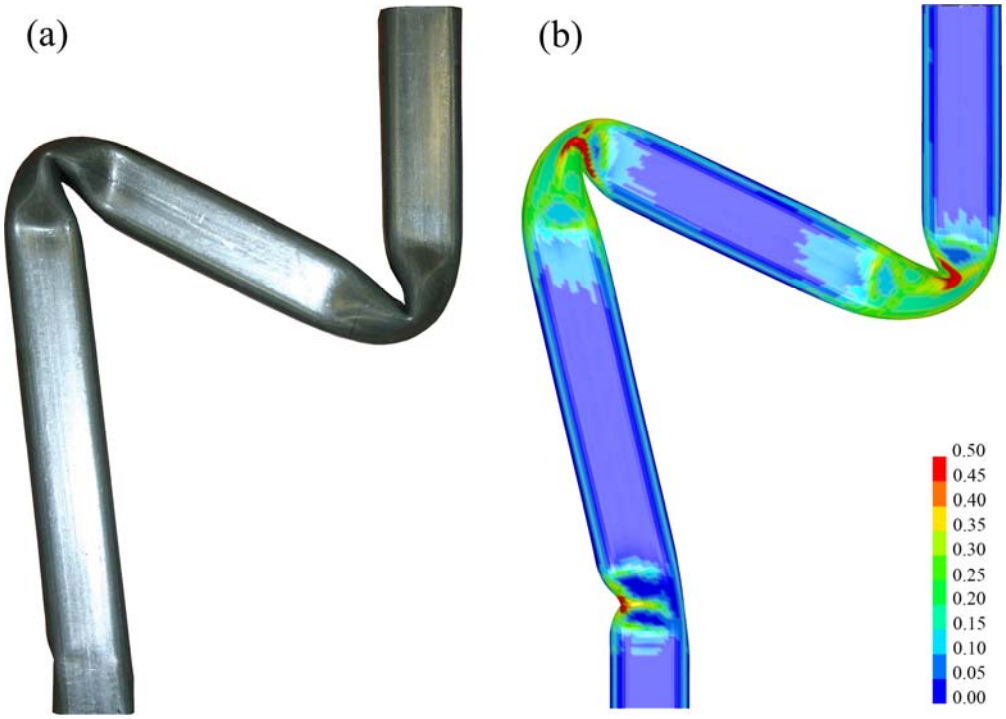

Figure 86: Juxtaposition of (a) actual and (b) predicted deformed geometry of hydroformed DP600 s-rails bent at an R/D ratio of 2.0 with contours of effective plastic strain

5.3.2 Crash results – load and energy

The predicted load and energy responses are presented in this section along with the measured experimental results in order to validate the accuracy of the numerical crash simulations. In order to duplicate the method of data acquisition used in the experiments, the predicted accelerations of the impact plate are monitored at the same frequency as that of the load cells used in the experiments (1000 Hz) and electronically filtered to mimic the mechanical filtering of the experiments; the mechanical filter is approximated by Mayer (2006b) as the equivalent of a Butterworth electronic filter (Butterworth, 1930) at 1000 Hz, therefore all predicted accelerations were numerically filtered using this scheme. The filtered predicted accelerations are then multiplied by the mass of the plate (1160 kg) to obtain the crushing loads. Load histories obtained using the contact forces between the impact plate and s-rail displayed excessive oscillations, therefore this method was not used for extracting the predicted loads from the numerical models. All of the predicted results presented in this section and forthcoming sections are based on numerical simulations utilizing a Johnson-Cook strain-rate-sensitive material model, except when explicitly stated otherwise.

Predicted and measured crash results for non-hydroformed and hydroformed DP600 s-rails bent at R/D ratios of 1.5, 2.0, and 2.5 are presented in Figure 87, Figure 88, and Figure 89, respectively; the corresponding predicted and measured peak loads and absorbed energies at 300 mm of crush displacement are tabulated in Table 17, Table 18, and Table 19. For all the tabulated results presented in this section, percentage differences are quoted for the predicted values with respect to the measured values. The predicted and measured load responses are in excellent accord for all the DP600 models, particularly after 50mm of displacement. The predicted peak loads for all the DP600 simulations are roughly within ±4% of the measured peak loads, the greatest deviation occurring for non-hydroformed DP600 s-rails bent at an R/D ratio of 2.0, in which case the peak load is over-predicted by 4.3%.

Since previous sections have established the accuracy of the forming models, it is unlikely that the discrepancies between the predicted and measured peak loads are a result of the use of inaccurate forming histories in the numerical simulations. Two important factors affecting the predictions of peak load are the constitutive material model used in the simulations, and the fact that the Butterworth filter applied to the predicted accelerations is only an approximation of the mechanical filter of the experimental setup.

Predictions of energy absorption are inherently not as accurate as load predictions since the energy-displacement curves are derived by integrating the force-displacement curves; consequently, any slight discrepancy between the predicted and measured forces leads to a larger discrepancy in the energy responses due to cumulative error induced through integration. For all the cases presented for DP600 s-rails, the numerical simulations over-predict the measured energy absorptions, with a minimum error of 2.1% for hydroformed s-rails bent at an R/D ratio of 2.0, and a maximum error of 9.0% for non-hydroformed s-rails bent at the same R/D ratio. In general, the simulations of hydroformed DP600 s-rails provide more accurate predictions of energy absorption when compared with simulations of non-hydroformed s-rails. The numerical predictions for DP600 s-rails are in close agreement with the measured results and accurately capture the effects of R/D ratio on the crash responses, therefore the results for HSLA350 1.8mm, HSLA350 1.5mm, and DDQ s-rails will be presented only at an R/D ratio of 2.0.

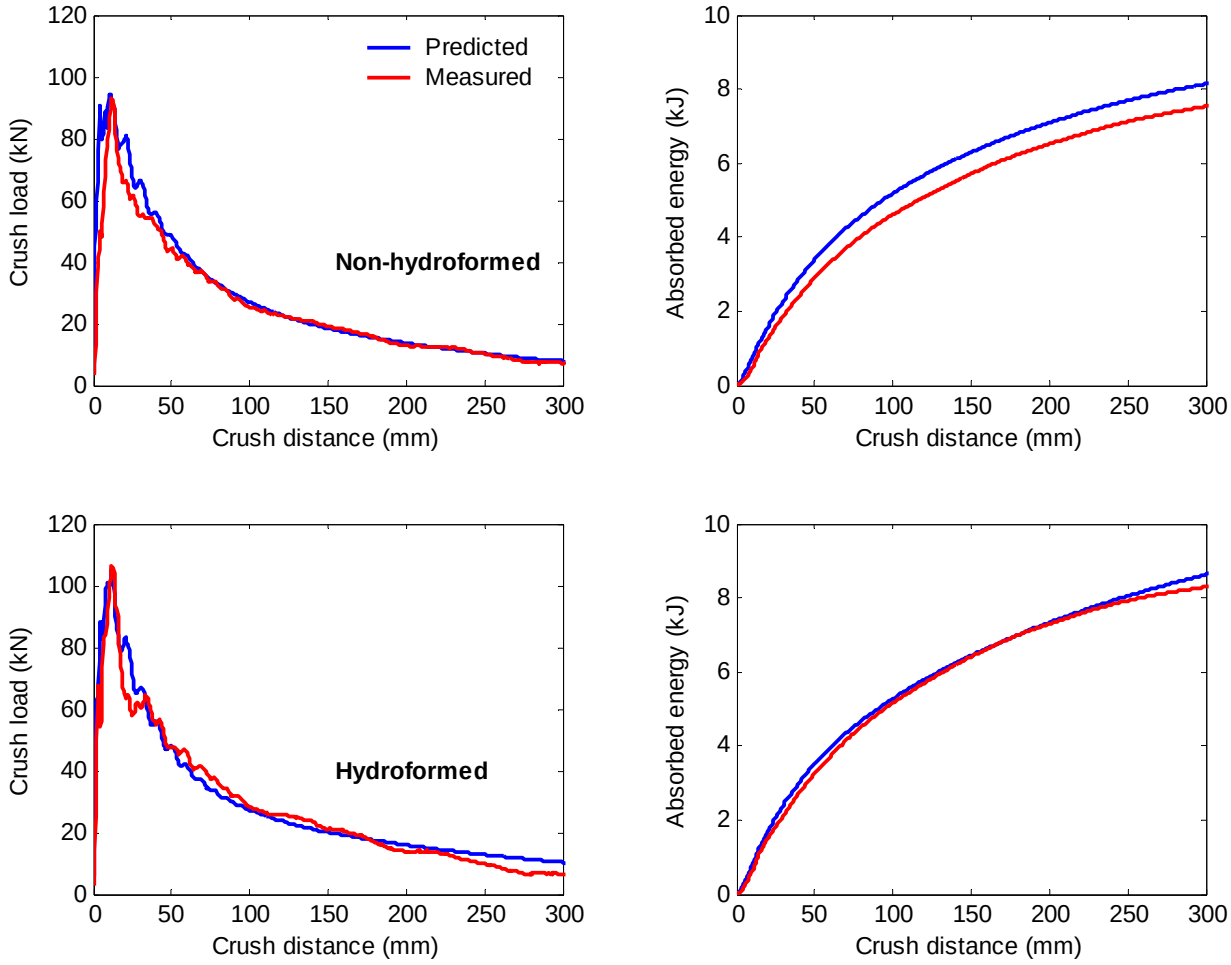

Figure 87: Predicted and measured crash results for non-hydroformed and hydroformed DP600 s-rails bent at an R/D ratio of 1.5

Table 17: Predicted and measured peak load and energy results for non-hydroformed and hydroformed DP600 s-rails bent at an R/D ratio of 1.5

	Non-hydroformed		Hydroformed	
	Measured	Predicted	Measured	Predicted
Peak load (kN)	92.8	94.5 (+1.8%)	106.4	104.8 (-1.5%)
Energy @ 300 mm (kJ)	7.53	8.14 (+8.1%)	8.30	8.63 (+4.0%)

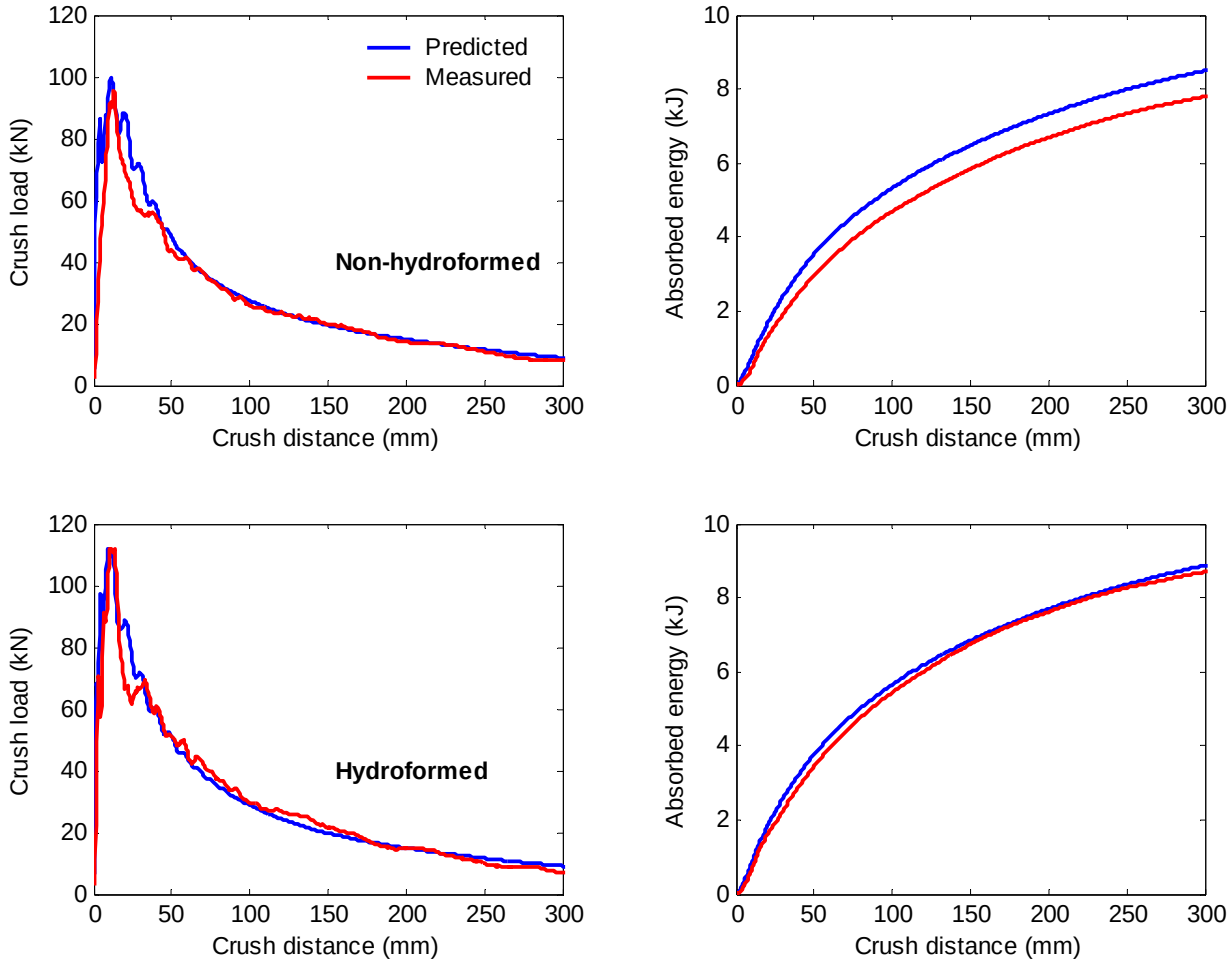

Figure 88: Predicted and measured crash results for non-hydroformed and hydroformed DP600 s-rails bent at an R/D ratio of 2.0

Table 18: Predicted and measured peak load and energy results for non-hydroformed and hydroformed DP600 s-rails bent at an R/D ratio of 2.0

	Non-hydroformed		Hydroformed	
	Measured	Predicted	Measured	Predicted
Peak load (kN)	95.7	99.8 (+4.3%)	112.1	112.3 (+0.2%)
Energy @ 300 mm (kJ)	7.79	8.49 (+9.0%)	8.69	8.87 (+2.1%)

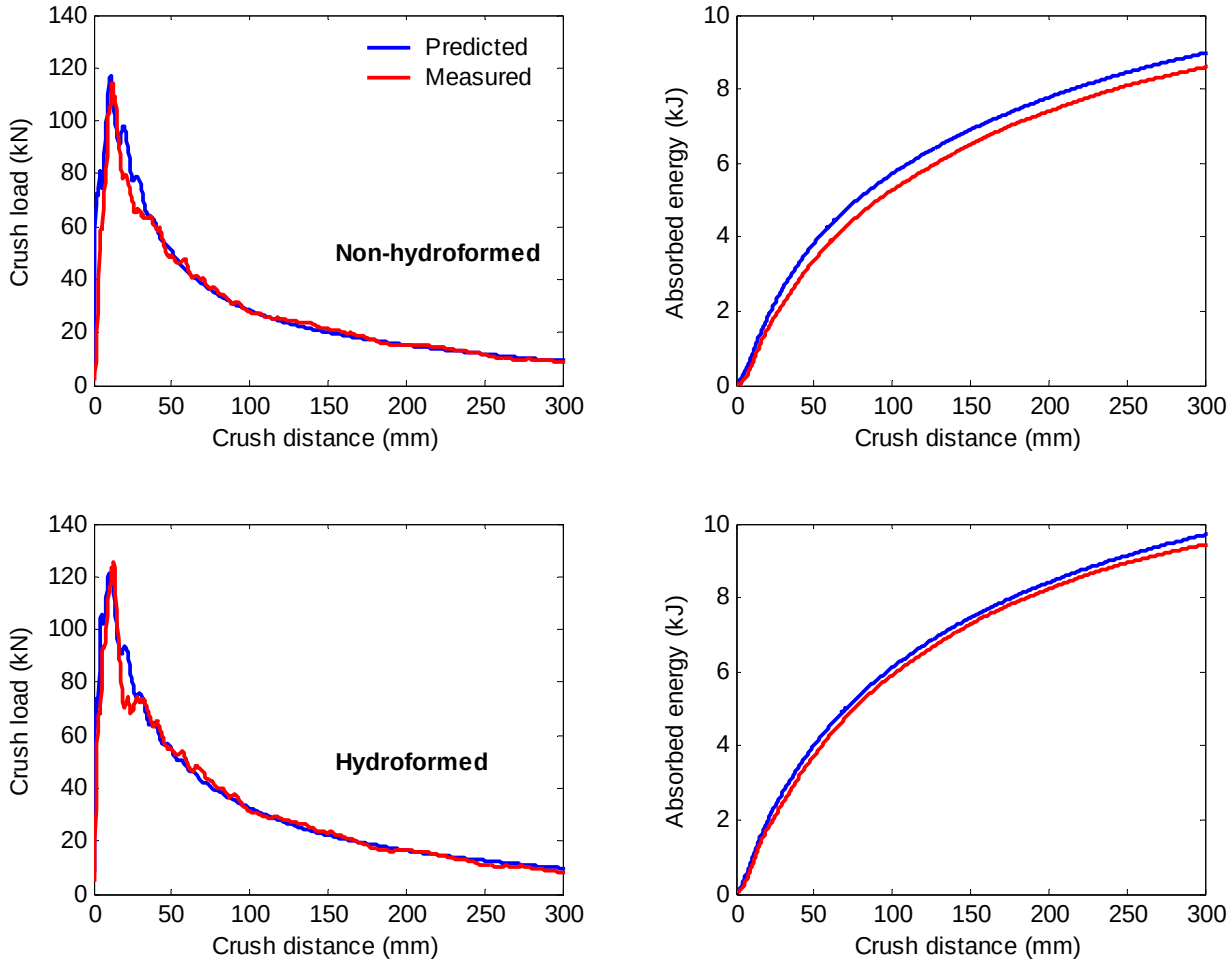

Figure 89: Predicted and measured crash results for non-hydroformed and hydroformed DP600 s-rails bent at an R/D ratio of 2.5

Table 19: Predicted and measured peak load and energy results for non-hydroformed and hydroformed DP600 s-rails bent at an R/D ratio of 2.5

	Non-hydroformed		Hydroformed	
	Measured	Predicted	Measured	Predicted
Peak load (kN)	114.2	116.6 (+2.1%)	125.2	120.8 (-3.5%)
Energy @ 300 mm (kJ)	8.58	8.96 (+4.4%)	9.43	9.69 (+2.8%)

Predicted and measured crash loads and energies for non-hydroformed and hydroformed HSLA350 1.8mm s-rails bent at an R/D ratio of 2.0 are shown in Figure 90, with peak load and energy absorption values tabulated in Table 20. The predicted loads are in excellent accord with the measured loads after 50mm of displacement, however, the peak loads are under-predicted for both the non-hydroformed and hydroformed s-rails, with the latter predictions 9.5% lower than the experimental

results. The energy absorption responses are over-predicted by 6.3% and 2.9 % for the non-hydroformed and hydroformed s-rails, respectively, displaying the previously observed trend of more accurate energy predictions for hydroformed s-rails.

Predicted and measured load and energy responses for HSLA350 1.5mm s-rails bent at an R/D ratio of 2.0 are shown in Figure 91, and the peak loads and values of absorbed energy are enumerated in Table 21. The predictions of peak load deviate from the measured values by as much as 7.4% (for the hydroformed s-rail), however, the absorbed energies are in excellent agreement with the measured values, with a maximum discrepancy of only 0.7% at a displacement of 300mm (again, for the hydroformed s-rail). For the HSLA350 1.5mm s-rails, the numerical predictions for the non-hydroformed s-rails are actually slightly more accurate that those of the hydroformed s-rails, a result that is contrary to the findings for the DP600 and HSLA350 1.8mm s-rails. This suggests that the accuracy of the numerical predictions is not governed by the cross-sectional geometry of the s-rail.

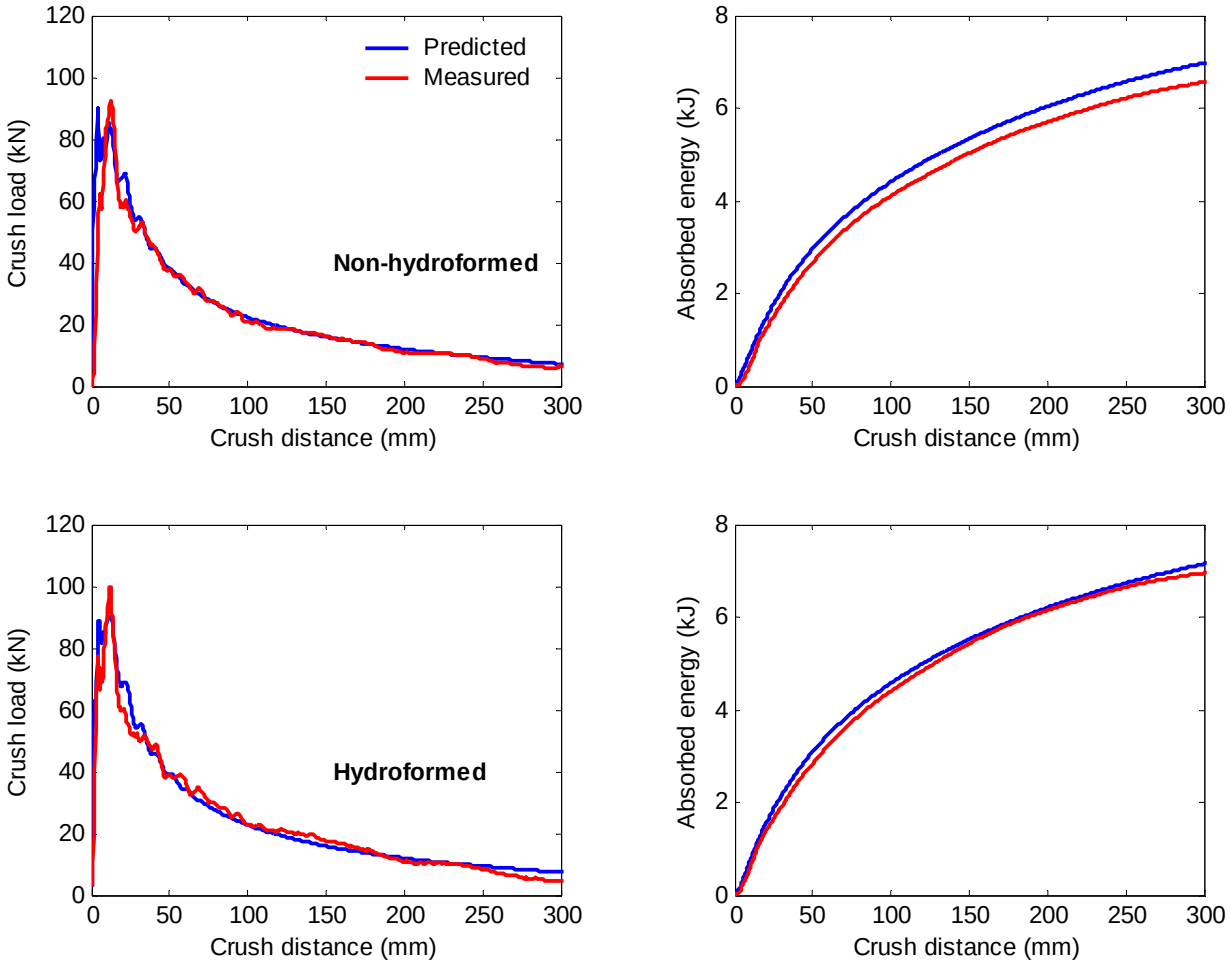

Figure 90: Predicted and measured crash results for non-hydroformed and hydroformed HSLA350 1.8mm s-rails bent at an R/D ratio of 2.0

Table 20: Predicted and measured peak load and energy results for non-hydroformed and hydroformed HSLA350 1.8mm s-rails bent at an R/D ratio of 2.0

	Non-hydroformed		Hydroformed	
	Measured	Predicted	Measured	Predicted
Peak load (kN)	92.6	89.7 (-3.1%)	99.9	90.45 (-9.5%)
Energy @ 300 mm (kJ)	6.56	6.98 (+6.3%)	6.95	7.15 (+2.9%)

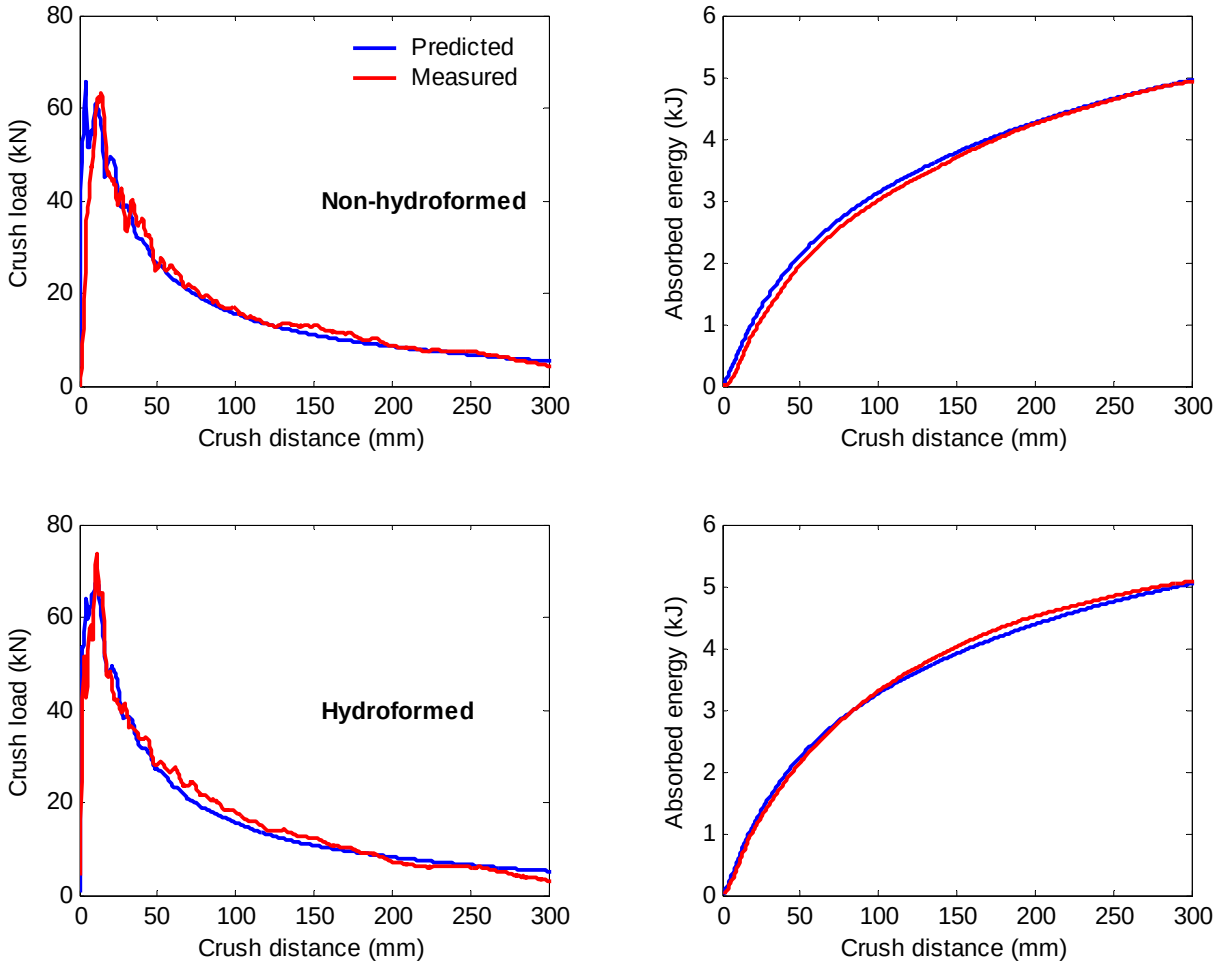

Figure 91: Predicted and measured crash results for non-hydroformed and hydroformed HSLA350 1.5mm s-rails bent at an R/D ratio of 2.0

Table 21: Predicted and measured peak load and energy results for non-hydroformed and hydroformed HSLA350 1.5mm s-rails bent at an R/D ratio of 2.0

	Non-hydroformed		Hydroformed	
	Measured	Predicted	Measured	Predicted
Peak load (kN)	63.4	65.5 (+3.3%)	73.6	68.1 (-7.4%)
Energy @ 300 mm (kJ)	4.93	4.95 (+0.4%)	5.07	5.04 (-0.7%)

Predicted and measured crash results for non-hydroformed and hydroformed DDQ s-rails are shown in Figure 92; the corresponding peak loads and values of absorbed energy at 300mm of displacement are listed in Table 22. Overall, the levels of agreement between the predicted and measured values are roughly the same as those presented for the other materials. The discrepancies between the predicted and measured peak loads and absorbed energies are approximately 6.5% (under-prediction) and 8.5% (over-prediction), respectively, for both the non-hydroformed and hydroformed s-rails.

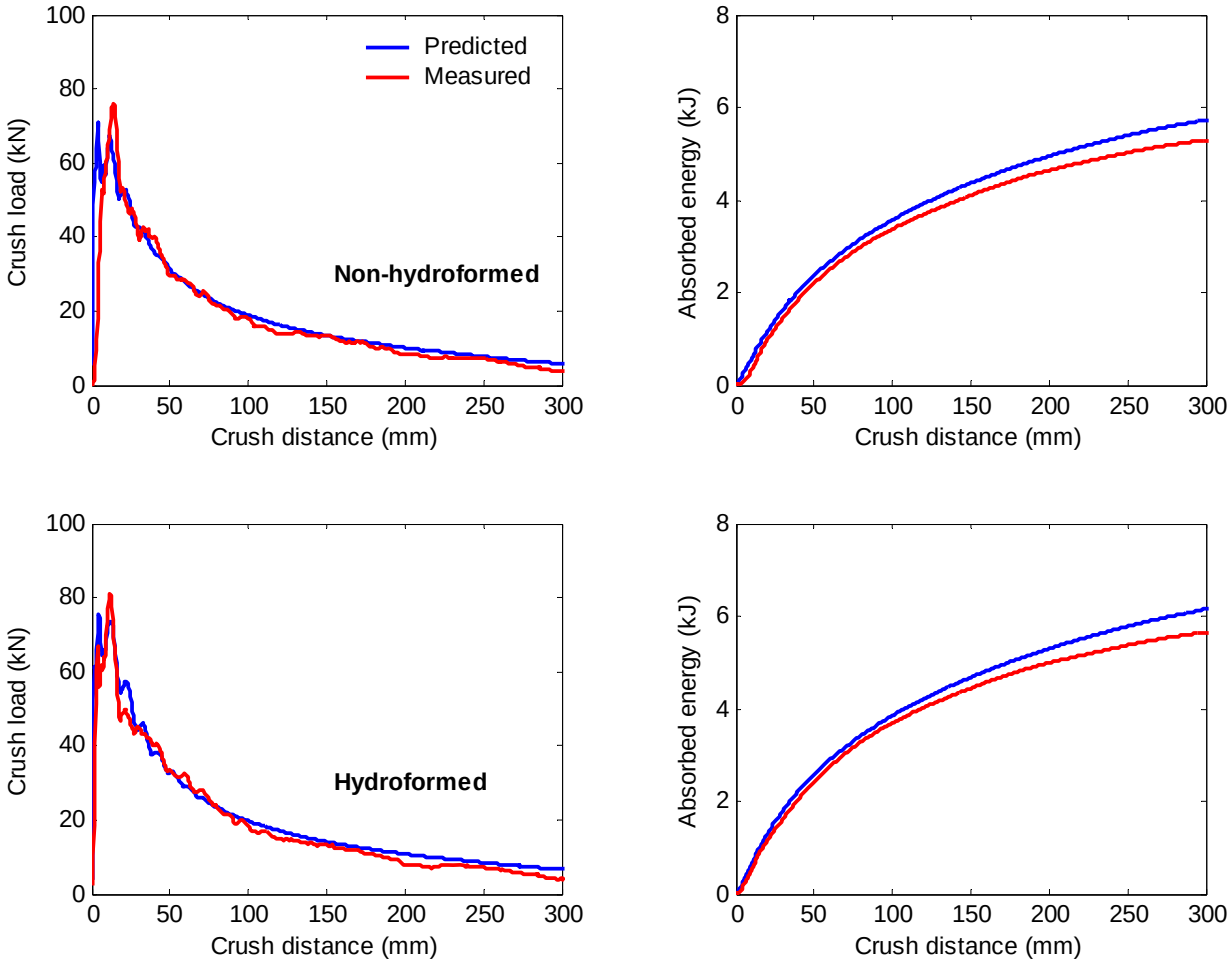

Figure 92: Predicted and measured crash results for non-hydroformed and hydroformed DDQ s-rails bent at an R/D ratio of 2.0

Table 22: Predicted and measured peak load and energy results for non-hydroformed and hydroformed DDQ s-rails bent at an R/D ratio of 2.0

	Non-hydroformed		Hydroformed	
	Measured	Predicted	Measured	Predicted
Peak load (kN)	75.8	71.0 (-6.3%)	81.2	75.6 (-6.9%)
Energy @ 300 mm (kJ)	5.29	5.73 (+8.4%)	5.65	6.15 (+8.9%)

The previously presented results serve to validate the numerical crash models. The predicted peak loads are all within 9.5% of the measured loads, while the predicted energies at 300mm of displacement are within 9.0% of the measured values. The numerical models of the HSLA350 1.5mm s-rails provide the most accurate predictions, while overall, the least accurate simulations are those for the DDQ s-rails.

The fact that the predictions for the HSLA350 1.5mm s-rails are the most accurate amongst the different materials is somewhat coincidental, since the high-rate properties of HSLA350 1.5mm were not actually tested, and the material properties measured for the HSLA350 1.8mm were used as a substitute. Examination of Figure 17 in Section 3.1 indicates that at quasi-static rates, the Johnson-Cook parameters used for the HSLA350 1.5mm material provide a material stress-strain curve that is roughly 30 MPa lower than the measured quasi-static strength of this material at strains below 30%; this serves to lower the predictions of load and energy and leads to better agreement between the predicted and measured results. It is expected that if the high-rate properties of HSLA350 1.5mm were tested and used in the numerical simulations, the corresponding predictions would be in similar accord with the measured results as the other materials. Among the three materials for which high-rate testing was performed, the Johnson-Cook fit for the DDQ deviated from the measured values by the greatest amount, which explains why the predicted crash results are the least accurate for this material.

Overall, the level of agreement between the predicted and measured results instills a high degree of confidence in the numerical models, therefore simulations will be utilized in upcoming sections to study aspects of the crash of s-rails that cannot be investigated through experiments, and for which measured results do not exist for validation.

5.3.3 Effect of constitutive models in crash simulations

The aim of this section is to determine the effects of utilizing different constitutive models on the predicted crash results and, in particular, to observe the differences between the results predicted using quasi-static versus so-called rate-sensitive high-rate material properties. Figure 93 presents numerical results obtained by using four different constitutive models, along with the measured crash

response, for a hydroformed DP600 s-rail bent at an R/D ratio of 2.0. The peak load and absorbed energy results are tabulated in Table 23; the percentage differences are shown with respect to the measured results. The different material models consist of a Johnson-Cook model (Equation 2 in Section 3.1), a modified Johnson-Cook model with a Voce-type quasi-static term (Equation 5 in Section 3.1), a Zerilli-Armstrong model (Equation 6 in Section 3.1), and a simple power-law quasi-static model (Equation 1 in Section 3.1).

The loads and energies predicted using the three high-rate material models are extremely similar, in fact, it is difficult to discern differences in the results predicted by the Johnson-Cook and modified Johnson-Cook models since they overlap with the predicted Zerilli-Armstrong results. The results predicted using the quasi-static power-law model, however, are noticeably lower than those obtained using high-rate material properties.

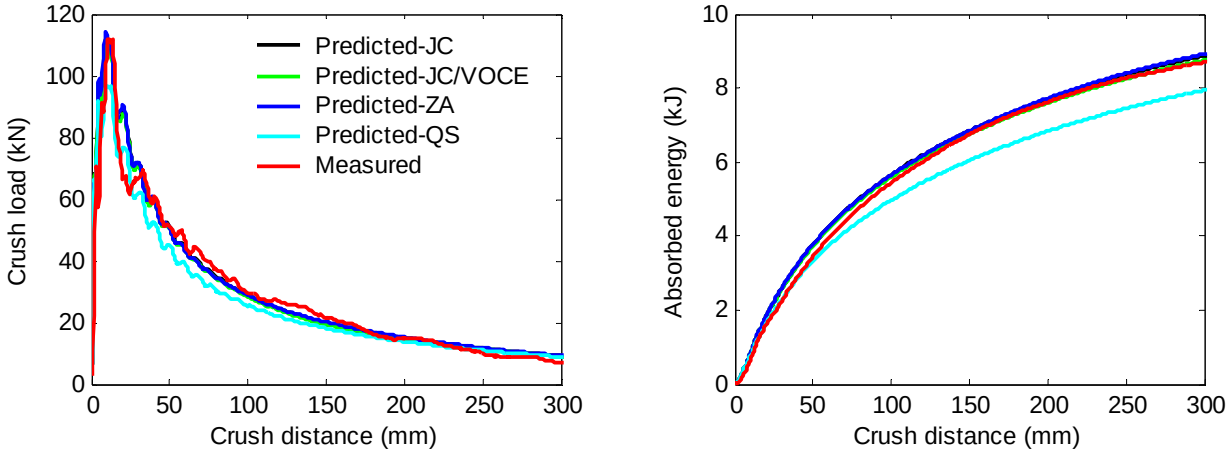

Figure 93: Crash results predicted using four different constitutive material models, and measured crash test results for hydroformed DP600 s-rails bent at an R/D ratio of 2.0 (JC = Johnson-Cook, JC/VOCE = Modified Johnson-Cook with Voce-type quasi-static term, ZA = Zerilli-Armstrong, QS = Quasi-static power law model)

Table 23: Peak load and energy results predicted using four different constitutive material models, and measured test results for hydroformed DP600 s-rails bent at an R/D ratio of 2.0

	Measured	Predicted-JC	Predicted-JC/VOCE	Predicted-ZA	Predicted-QS
Peak load (kN)	112.1	112.3 (+0.2%)	111.1 (-0.9%)	113.7 (+1.5%)	96.9 (-13.5%)
Energy @ 300 mm (kJ)	8.69	8.87 (+2.1%)	8.75 (+0.7%)	8.92 (+2.6%)	7.94 (-8.6%)

All three high-rate models provide predictions that are in close accord with the measured values. The predicted peak loads deviate from the measured results by a maximum of only 1.5%, and

the predicted energies at 300mm of displacement deviate by a maximum of 2.6%, with the Zerilli-Armstrong model providing the least accurate predictions of both measured quantities. The Johnson-Cook model is the most accurate for predicting the peak load, while the modified Johnson-Cook model provides the most accurate prediction of absorbed energy. The predicted peak load obtained using the quasi-static model is 13.5% lower than the measured value, while the predicted energy using this material model is 8.6% lower than the measured result. The maximum strain rate predicted by numerical simulations during crushing of an s-rail impacted at 4.57 m/s is roughly 210 strain/second, a value that decreases below 100 strain/second for the majority of the crash event; a plot of strain rate during the crash event is shown in Figure 94 for the element on the s-rail displaying the maximum strain rate (which occurs within one of the plastic hinge regions). Using the Johnson-Cook material model (Equation 2 in Section 3.1) and the DP600 material parameters presented in Section 3.1, it can be shown that the expected increase in flow stress caused by the elevated strain rates is roughly 7-8%. This increase in strength serves to explain why predictions based on the quasi-static material properties are approximately 10% lower than the measured results, since the quasi-static material model does not account for any increases in flow stress with strain rate.

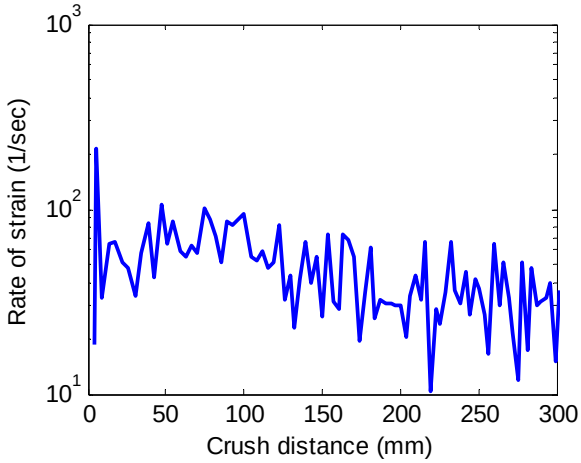

Figure 94: Rate of strain during crash for an element within a plastic hinge region

Figure 95 shows the measured results for a hydroformed HSLA350 1.8mm s-rail bent at an R/D ratio of 2.0 along with results predicted using three different constitutive models (Johnson-Cook, Zerilli-Armstrong, and quasi-static); the corresponding peak load and energy values are tabulated in Table 24. The tabulated peak load and absorbed energy results for the HSLA350 1.8mm and DP600 s-rails are also presented graphically in Figure 96. Once again, the two high-rate material models provide

nearly identical predictions, while the results predicted using the quasi-static model are appreciably lower.

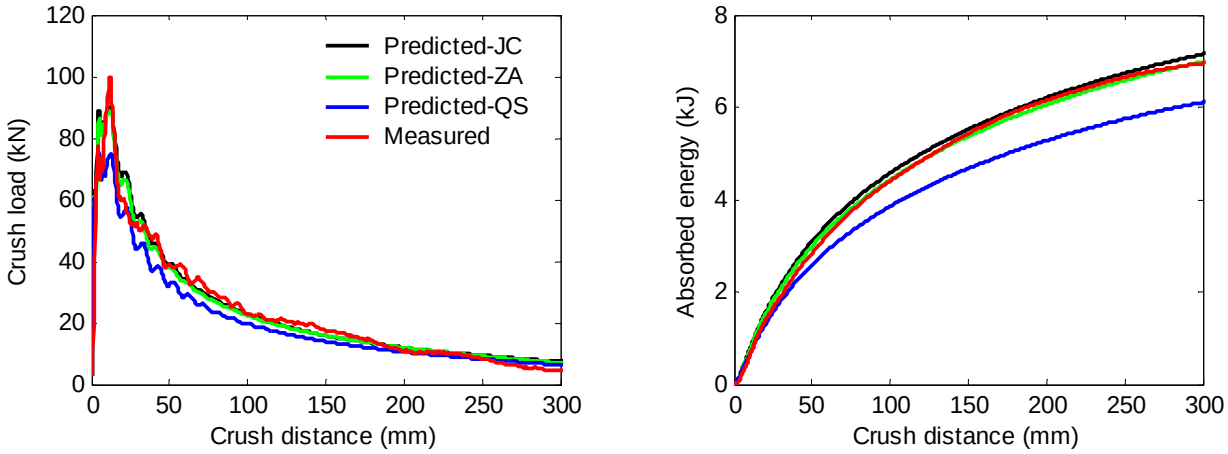

Figure 95: Crash results predicted using three different constitutive material models, and measured crash test results for hydroformed HSLA350 1.8mm s-rails bent at an R/D ratio of 2.0 (JC = Johnson-Cook, ZA = Zerilli-Armstrong, QS = Quasi-static power law model)

Table 24: Peak load and energy results predicted using three different constitutive material models, and measured test results for hydroformed HSLA350 1.8mm s-rails bent at an R/D ratio of 2.0

	Measured	Predicted-JC	Predicted-ZA	Predicted-QS
Peak load (kN)	99.9	90.5 (-9.5%)	88.9 (-11.0%)	75.9 (-24.0%)
Energy @ 300 mm (kJ)	6.95	7.15 (+2.9%)	6.98 (+0.4%)	6.10 (-12.2%)

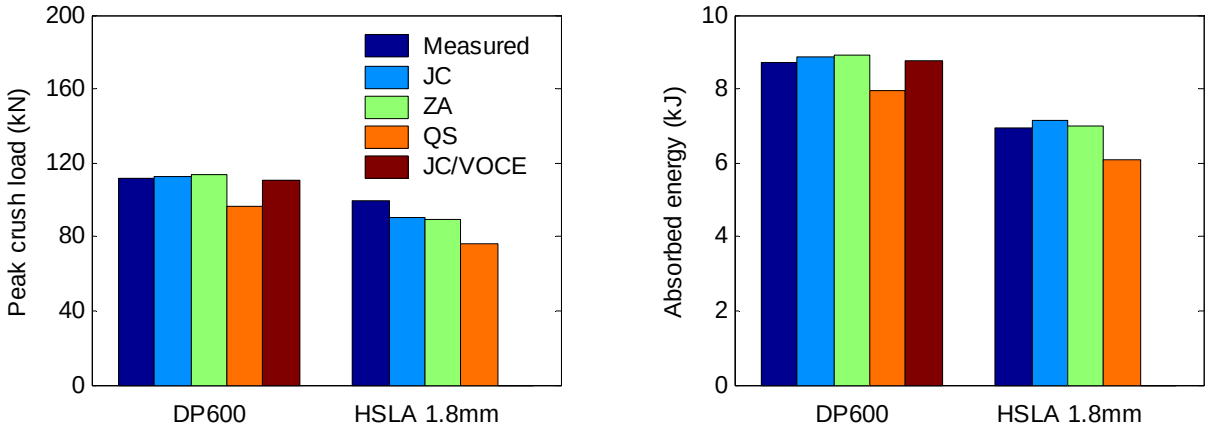

Figure 96: Peak load and energy results predicted using different constitutive material models, and measured test results for hydroformed HSLA350 1.8mm and DP600 s-rails bent at an R/D ratio of 2.0

The predictions of peak load obtained using the Johnson-Cook and Zerilli-Armstrong models are approximately 10% lower than the measured values, while the predicted values of absorbed energy are in excellent agreement with the experimental results. The peak load prediction derived using the quasi-static material model is 16% lower than the prediction using the Johnson-Cook material model, while the energy prediction is 15% lower than the Johnson-Cook prediction. Using the Johnson-Cook model parameters for the HSLA350 1.8mm material (refer to Section 3.1) and the previously quoted strain rates, it can be shown that strain rate effects increase the flow stress of the HSLA350 1.8mm material by roughly 12-14% during crash of s-rails, which explains why predictions obtained using quasi-static material properties are lower than the Johnson-Cook predictions by approximately the same amount. In summary, the consideration of strain-rate effects is important when modeling impact of strain-rate sensitive materials such as steel.

5.3.4 Effect of forming histories in crash simulations

In this section, specific components of the s-rail forming history, which include work hardening (plastic strains), residual stresses, and thickness changes, are systematically removed from the numerical crash models in order to observe their relative effects on the predicted results. Figure 97 shows the predicted crash results obtained from models considering the full forming history of a non-hydroformed DP600 s-rail bent at an R/D ratio of 2.0, and results from three numerical models in which work hardening, residual stresses, and thickness changes are progressively removed from the full forming history of the s-rail (refer to the figure caption for descriptions of the acronyms used in the figure legend). The final model in this sequence neglects all work hardening, residual stresses, and material thickness changes incurred though the bending operations. The corresponding peak load and energy predictions are listed in Table 25, along with percentage differences shown with respect to the model considering the full forming history of the s-rail. The same set of results is shown and tabulated in Figure 98 and Table 26 for a hydroformed DP600 s-rail bent at an R/D ratio of 2.0. A summary of the predicted peak load and energy results for the non-hydroformed and hydroformed DP600 s-rails is presented graphically in Figure 99.

In the case of the non-hydroformed s-rails, neglecting only the work hardening lowers the peak load and energy predictions by roughly 6.5%; through subsequent excision of residual stresses, the predicted values actually increase minutely when compared to the model neglecting only the work hardening. By also neglecting the material thickness changes, the predicted peak load and energy decrease by a further 2.5% and 1.5%, respectively. Complete omission of all three constituents of the forming history lowers the predicted peak load and energy results by roughly 8% over the predictions obtained by considering all aspects of the forming history. These results indicate that among the three

components of the forming history, material work hardening has the greatest effect on the crash response of s-rails, while residual stresses have the least significant effect. The explanation for this conclusion is that increased levels of work hardening (plastic strain) increase the flow stress of the material, thereby requiring larger loads to continue deformation of the s-rail; in contrast, residual stresses do not affect the material's flow stress. Wall thickness changes have a minimal effect on the crash results since changes on the tensile side of a bend are essentially offset by changes on the compressive side of the bend. The minimal effect of thickness exhibited in the current results is contrary to the commonly accepted wisdom – based on stamping experience – that thickness changes are significant in accurately predicting the crash response of automotive components. Clearly, thickness changes will be important in cases unlike the current component in which thinning on one side of the s-rail is compensated by thickening on the other side.

The results for the hydroformed DP600 s-rails indicate similar trends and infer similar conclusions to those of the non-hydroformed s-rails, however, the effects of the forming histories on peak load predictions are more pronounced in the case of the hydroformed s-rails. By omitting the work hardening, the peak load prediction is reduced by 17%, and additional removal of the residual stresses increases the predicted peak load by 2% over the model neglecting only the work hardening. Excision of thickness changes accounts for a 4% reduction in the predicted peak load of a hydroformed DP600 s-rail. Overall, omitting all three constituents of forming history reduces the peak load prediction for a hydroformed DP600 s-rail by 19%. The relative changes in the predicted values of absorbed energy were similar to those of non-hydroformed s-rails, with a total reduction of 8% when omitting all three components of forming history.

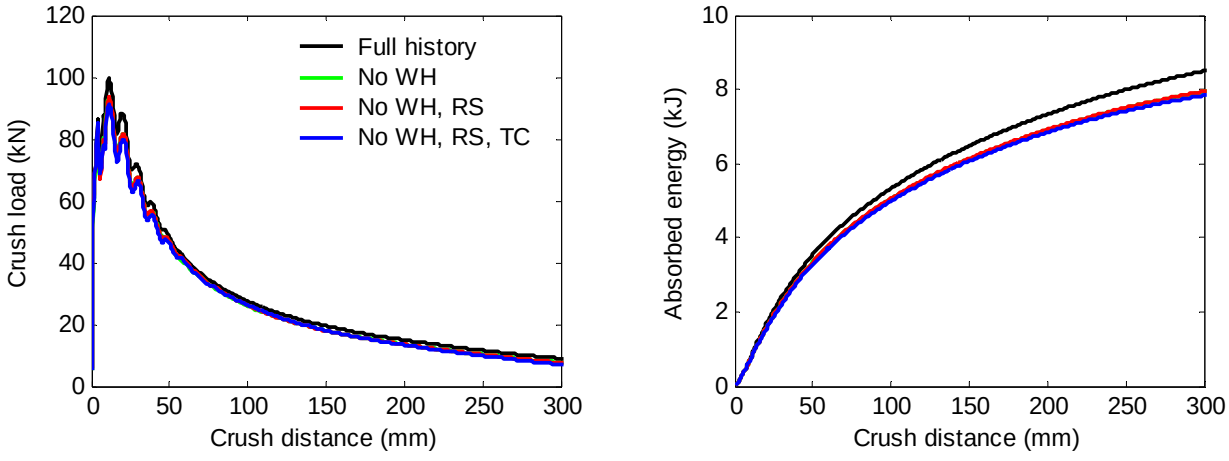

Figure 97: Predicted crash results using four varying levels of pre-forming history for non-hydroformed DP600 s-rails bent at an R/D ratio of 2.0 (WH=Work hardening, RS=Residual stresses, TC=Thickness changes)

Table 25: Predicted peak load and energy results using four varying levels of pre-forming history for non-hydroformed DP600 s-rails bent at an R/D ratio of 2.0

	Full History	No WH	No WH, RS	No WH, RS, TC
Peak load (kN)	99.8	93.2 (-6.6%)	93.6 (-6.2%)	91.3 (-8.5%)
Energy @ 300 mm (kJ)	8.49	7.94 (-6.6%)	7.95 (-6.4%)	7.83 (-7.8%)

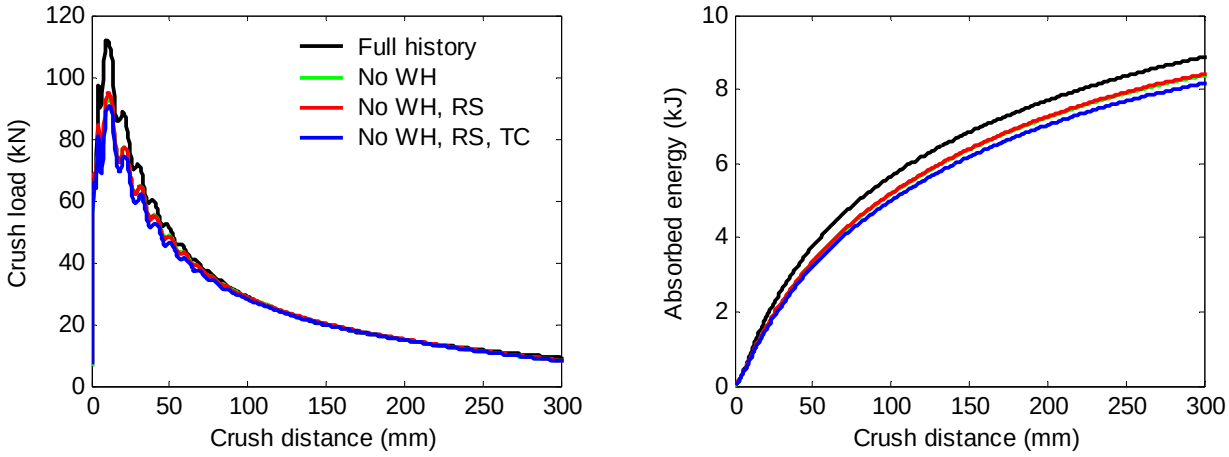

Figure 98: Predicted crash results using four varying levels of pre-forming history for hydroformed DP600 s-rails bent at an R/D ratio of 2.0 (WH=Work hardening, RS=Residual stresses, TC=Thickness changes)

Table 26: Predicted peak load and energy results using four varying levels of pre-forming history for hydroformed DP600 s-rails bent at an R/D ratio of 2.0

	Full History	No WH	No WH, RS	No WH, RS, TC
Peak load (kN)	112.3	93.1 (-17.0%)	94.7 (-15.6%)	90.7 (-19.2%)
Energy @ 300 mm (kJ)	8.87	8.37 (-5.6%)	8.40 (-5.3%)	8.16 (-8.0%)

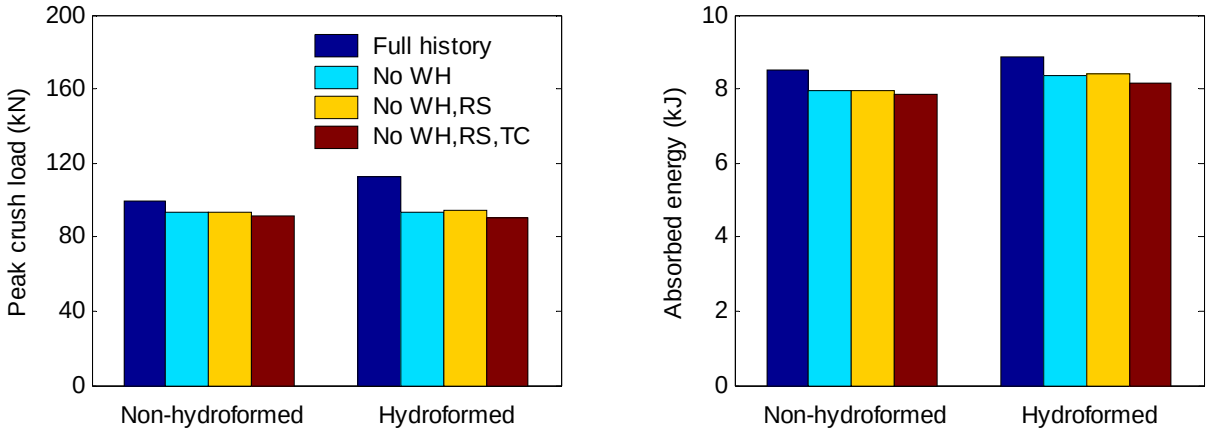

Figure 99: Predicted peak load and energy results using four varying levels of pre-forming history for non-hydroformed and hydroformed DP600 s-rails bent at an R/D ratio of 2.0

5.3.5 Effect of impact velocity on crash results

The effects of impact velocity, previously discussed in terms of the experimental results in Section 4.3.6, are examined in further detail in this section through numerical simulations. Figure 100 and Figure 101 present the predicted and measured results for HSLA350 1.8mm s-rails impacted at 6.46 and 8.06 m/s, respectively, with the corresponding peak loads and values of absorbed energy listed in Table 27 and Table 28 (percentage differences are presented with respect to the measured results). In the case of the 6.46 m/s impact velocity, the numerical model over-predicts the peak load by 19%, however, the prediction of absorbed energy is only 6.5% higher than the measured result. For the 8.06 m/s impact velocity, the numerical prediction of peak load is extremely accurate (only 0.4% higher than the measured result), while the prediction of absorbed energy at 300mm of displacement is 6.8% higher than the measured value. At the lower impact velocity, the numerical prediction of the loads is nearly identical to the measured loads beyond 50mm of displacement, while at the higher impact velocity, the predicted loads are in excellent agreement with the measured loads up to a displacement of 175mm.

Overall, the numerical predictions are in close agreement with the measured results, however, a significant discrepancy occurs between the predictions of peak load at the two different velocities; the prediction at the impact velocity of 6.46 m/s is actually 4.4% higher than the prediction at the impact velocity of 8.06 m/s, which is contrary to the trends in the measured peak loads. The cause of this anomaly was elusive, and the problem could not be rectified. Since the predictions for the impact velocity of 8.06 m/s were based on hydroformed s-rails and were quite accurate in regards to peak loads and absorbed energies, the subsequent numerical studies on the effects of impact velocity are conducted for hydroformed HSLA350 1.8mm s-rails bent at an R/D ratio of 1.5.

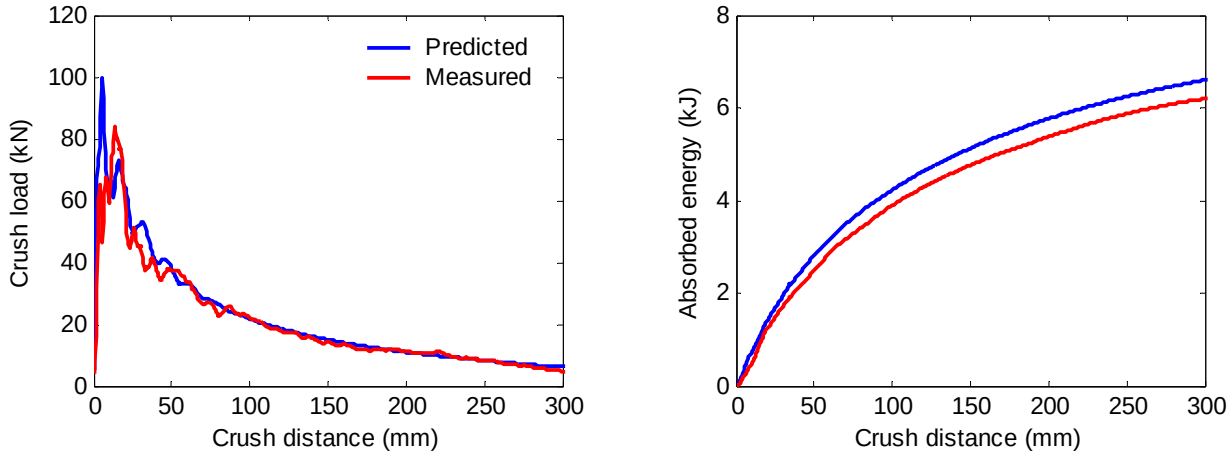

Figure 100: Predicted and measured crash results for non-hydroformed HSLA350 1.8mm s-rails bent at an R/D ratio of 1.5 and impacted at 6.46 m/s

Table 27: Predicted peak load and energy results for non-hydroformed HSLA350 1.8mm s-rails bent at an R/D ratio of 1.5 and impacted at 6.46 m/s

	Measured	Predicted
Peak load (kN)	84.0	99.9 (+19.0%)
Energy @ 300 mm (kJ)	6.19	6.60 (+6.5%)

In addition to the simulations carried out at 4.57 m/s and 8.06 m/s, hydroformed HSLA350 1.8mm s-rails are also simulated at impact velocities of 12 and 16 m/s, the results of which are shown in Figure 102 and tabulated in Table 29 (percentage differences are presented with respect to the 4.57 m/s impact velocity); these predictions are derived from simulations that account for the effects of strain-rate on material strength. The results illustrate a clear trend of increasing peak load with increasing impact velocity as illustrated in Figure 103, with a 76% increase in the peak load by increasing the velocity from 4.57 m/s to 16.00 m/s; beyond a displacement of roughly 50mm, however, the predicted loads are nearly identical for all four impact velocities. Consequently, energy absorption is not significantly affected by impact velocity as shown in Figure 103; by increasing the impact velocity from 4.57 to 16.00 m/s, the predicted energy absorption increases by only 8.1%.

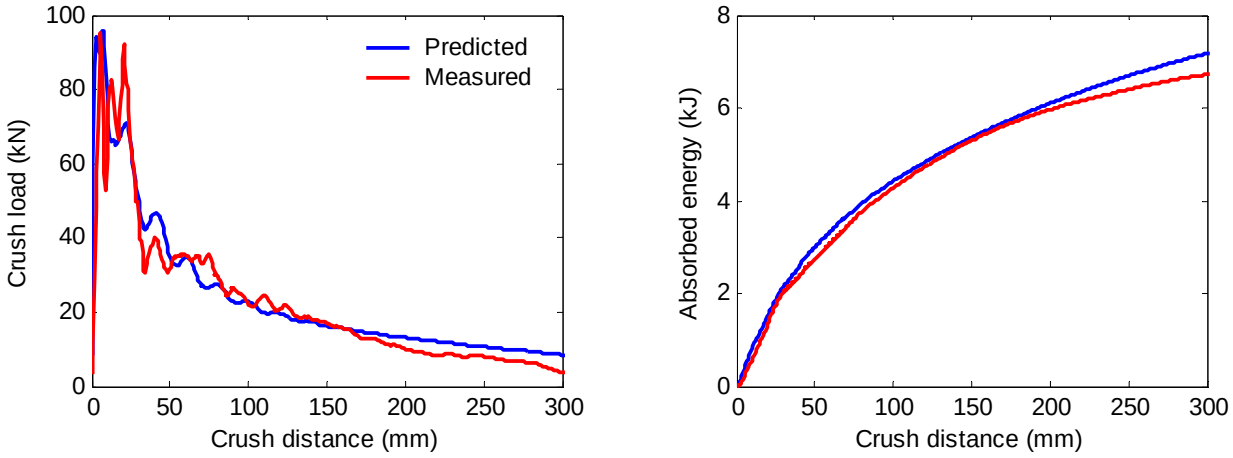

Figure 101: Predicted and measured crash results for hydroformed HSLA350 1.8mm s-rails bent at an R/D ratio of 1.5 and impacted at 8.06 m/s

Table 28: Predicted peak load and energy results for hydroformed HSLA350 1.8mm s-rails bent at an R/D ratio of 1.5 and impacted at 8.06 m/s

	Measured	Predicted
Peak load (kN)	95.4	95.7 (+0.4%)
Energy @ 300 mm (kJ)	6.72	7.17 (+6.8%)

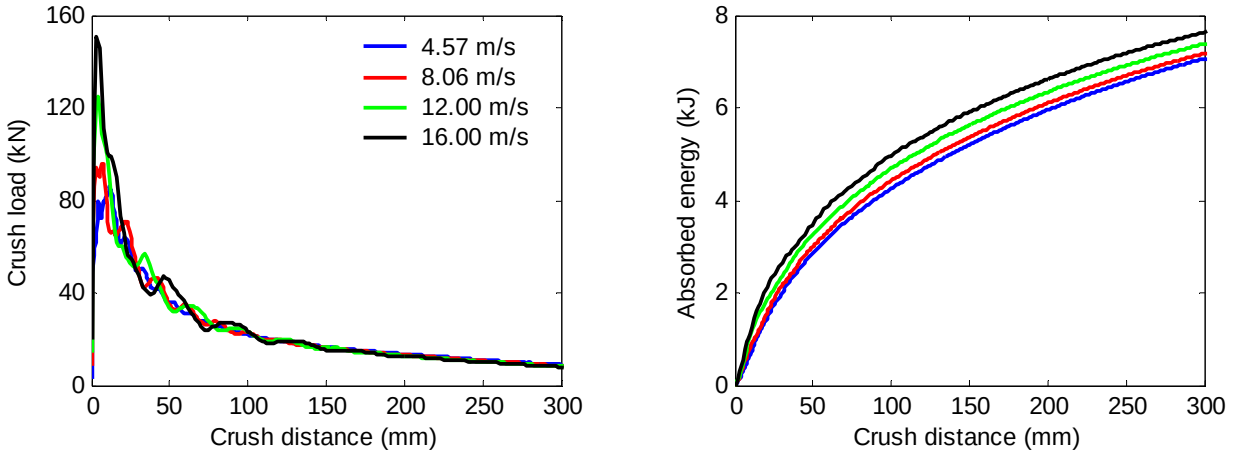

Figure 102: Crash results predicted using a Johnson-Cook strain-rate-dependent material model for hydroformed HSLA350 1.8mm s-rails bent at an R/D ratio of 1.5 and impacted at 4.57 m/s, 8.06 m/s, 12.00 m/s, and 16.00 m/s

Table 29: Peak load and energy results predicted using a Johnson-Cook strain-rate-dependent material model for hydroformed HSLA350 1.8mm s-rails bent at an R/D ratio of 1.5 and impacted at 4.57 m/s, 8.06 m/s, 12.00 m/s, and 16.00 m/s

	v=4.57 m/s	v=8.06 m/s	v=12.00 m/s	v=16.00 m/s
Peak load (kN)	85.8	95.7 (+11.6%)	125.1 (+45.8%)	150.7 (+75.6)
Energy @ 300 mm (kJ)	7.06	7.17 (+1.6%)	7.38 (+4.6%)	7.63 (8.1%)

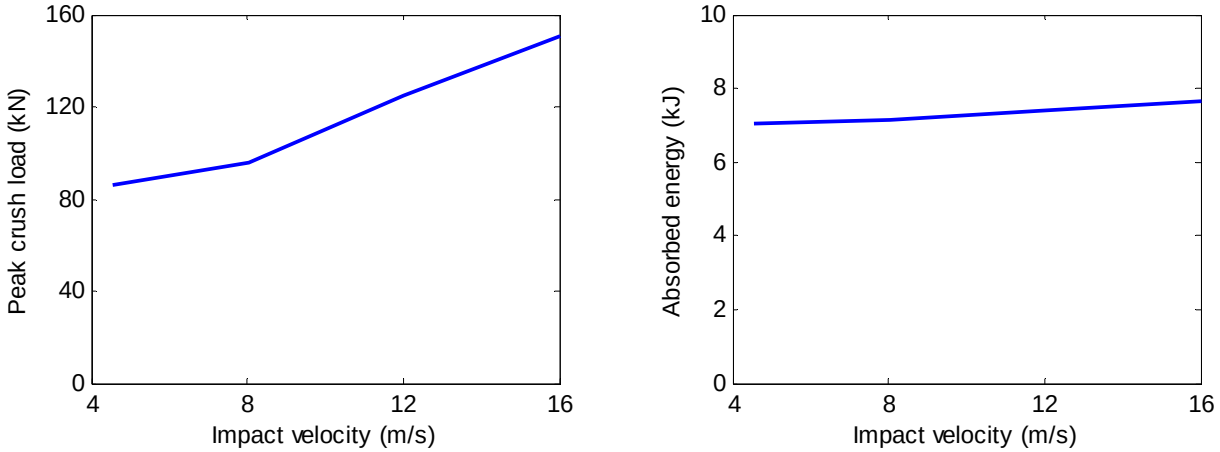

Figure 103: Predicted peak load and absorbed energy as a function of impact velocity for hydroformed HSLA350 1.8mm s-rails bent at an R/D ratio of 1.5

In order to determine whether the increases in peak load are a result of high-strain-rate effects or a result of inertial effects, simulations of impact at 4.57 and 16.00 m/s are performed using the rate-insensitive power-law material model; by doing so, strain-rate effects are easily removed from the problem. Figure 104 presents the predicted load and energy results for these simulations, while the predicted peak load and energy absorption values are listed in Table 30. The predicted peak load increases 98% by increasing the impact velocity from 4.57 to 16.00 m/s, while the energy at 300mm of displacement increases by 7.3%. Since strain-rate effects have been neglected, these results indicate that increases in the peak loads with increased impact velocity can be attributed primarily to inertial effects. This conclusion can be corroborated through examination of the strain-rates at the two velocities; at an impact velocity of 4.57 m/s, the maximum predicted strain-rate is 211 strain/second, while the maximum predicted strain-rate at the 16.00 m/s velocity is 412 strain/second. Using the Johnson-Cook material parameters for HSLA350 1.8mm from Section 3.1, it can be shown that the strain-rate-induced increases in material flow stress are 13.6% and 15.4% based on the maximum strain-rates predicted for impact at 4.57 and 16.00 m/s, respectively, which amounts to a minor difference in material strength as a result of the different impact velocities.

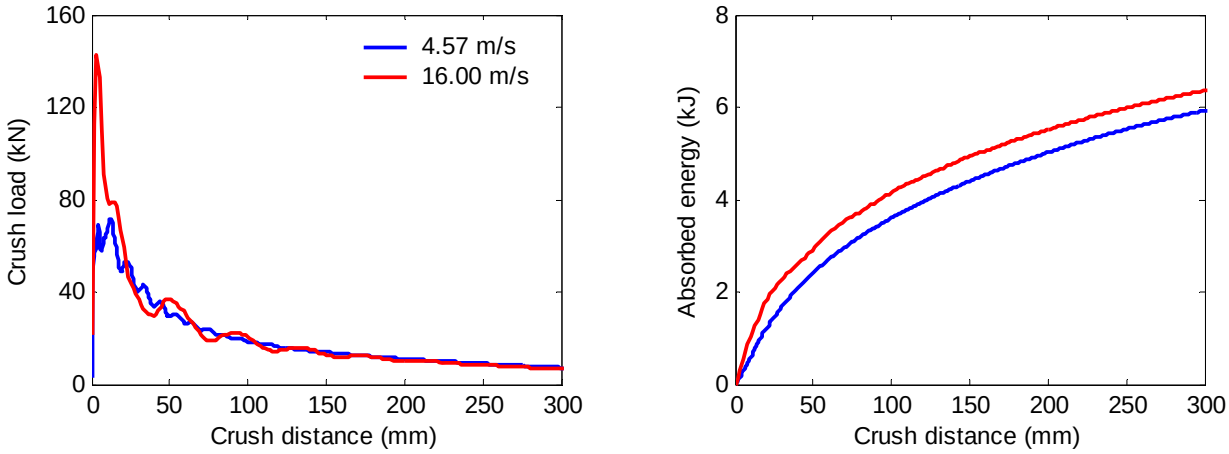

Figure 104: Crash results predicted using a strain-rate-independent material model for hydroformed HSLA350 1.8mm s-rails bent at an R/D ratio of 1.5 and impacted at 4.57 and 16.00 m/s

Table 30: Peak load and energy results predicted using a quasi-static strain-rate-independent material model for hydroformed HSLA350 1.8mm s-rails bent at an R/D ratio of 1.5 and impacted at 4.57 and 16.00 m/s

	v=4.57 m/s	v=16.00 m/s
Peak load (kN)	71.9	142.6 (+98.2%)
Energy @ 300 mm (kJ)	5.93	6.36 (+7.3%)

5.3.6 Potential for weight reduction of s-rails through material substitution

Weight reduction through material substitution – the main impetus for this research project – is addressed in this section through numerical simulations, since thinner gauges of DP600 and HSLA350 tube are not available for experimental examination. Crash simulations are performed of hydroformed s-rails bent at an R/D ratio of 2.0 and made from DDQ steel with a wall thickness of 1.86mm (the actual wall thickness of the DDQ tubes investigated in this thesis), and also with DP600 and HSLA350 steels at various wall thicknesses starting at 1.86mm then reducing to 1.70mm, and reducing incrementally by 0.1mm thereafter. The impact velocity is 4.57 m/s for all cases, and the corresponding high-rate material properties are used for all three materials. Work hardening and residual stresses caused by the forming operations are considered in all the simulations in this study, however, it is assumed that for each material, the levels of work hardening and residual stress are the same for the different tube wall thicknesses. Material thickness changes caused by the forming operations are neglected for all of the materials in this study since bending and hydroforming simulations would be required for each thickness of DP600 and HSLA350, which would be extremely time-consuming for

this type of parametric study; by neglecting the wall thickness changes for all three materials, the conclusions drawn from this study will be equally applicable to structures with full forming histories. Moreover, it has been established in Section 5.3.4 that wall thickness changes caused by forming have a minimal effect on the crash response of s-rails, therefore their omission will not be deleterious to the results of this study. The DP600 and HSLA350 material properties are assumed to be identical for the different wall thicknesses used in the parametric study.

The variance of the predicted peak load and energy absorption of hydroformed HSLA350 and DP600 s-rails as a function of tube wall thickness is illustrated in Figure 105; the dotted lines represent the peak load and energy absorption of hydroformed DDQ s-rails with a wall thickness of 1.86mm. Based on these plots, it is determined that HSLA350 and DP600 s-rails with wall thicknesses of 1.70mm and 1.50mm, respectively, will absorb roughly the same amount of energy and exhibit roughly the same peak crush loads as a DDQ s-rail made from 1.86mm wall thickness tube.

The load-displacement and energy-displacement plots for the 1.86mm DDQ, the 1.70mm HSLA350, and the 1.50mm DP600 s-rails are presented in Figure 106, with corresponding peak load and energy absorption results tabulated in Table 31 (percentage differences are shown relative to the DDQ 1.86mm s-rails). The peak loads exhibited by the HSLA350 1.70mm and DP600 1.50mm s-rails are actually higher than that of the DDQ 1.86mm s-rails by 5.3% and 6.1%, respectively. The energy absorbed by HSLA350 1.70mm s-rails is 0.8% higher than the DDQ 1.86mm s-rails, while the energy absorption of DP600 1.50mm s-rails is lower than the DDQ 1.86mm s-rails by 2.0%. The mass of the DDQ 1.86mm s-rails is 7.23kg (for two s-rails), while that of the HSLA350 1.70mm and DP600 1.50mm s-rails is 6.62 and 5.86kg, respectively, a reduction of 8.4% and 19.0% without an appreciable reduction in energy absorption.

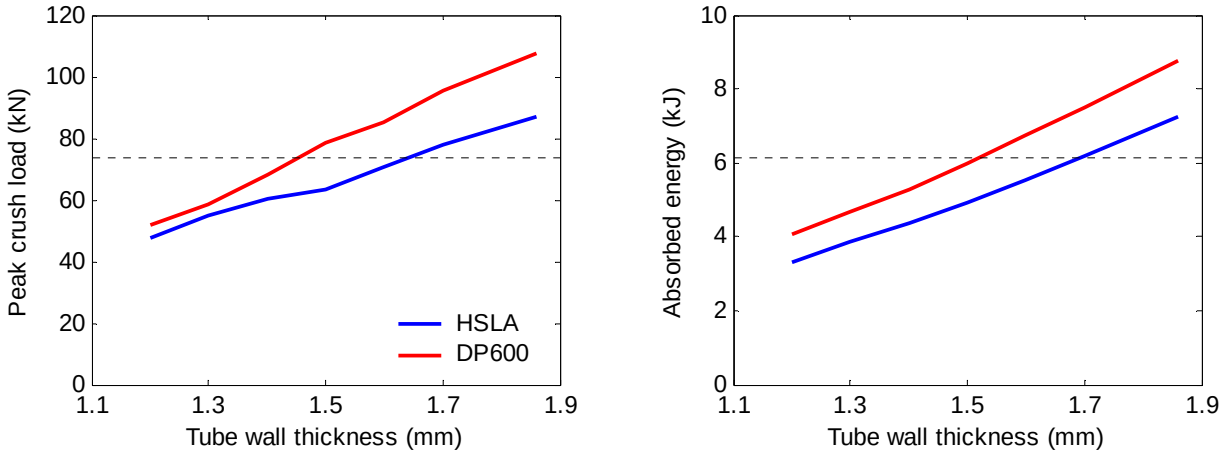

Figure 105: Predicted peak load and energy absorption as a function of material thickness for hydroformed HSLA350 and DP600 s-rails bent at an R/D ratio of 2.0 (the dotted lines represent the peak load and energy absorption of a hydroformed DDQ s-rail with a wall thickness of 1.86mm)

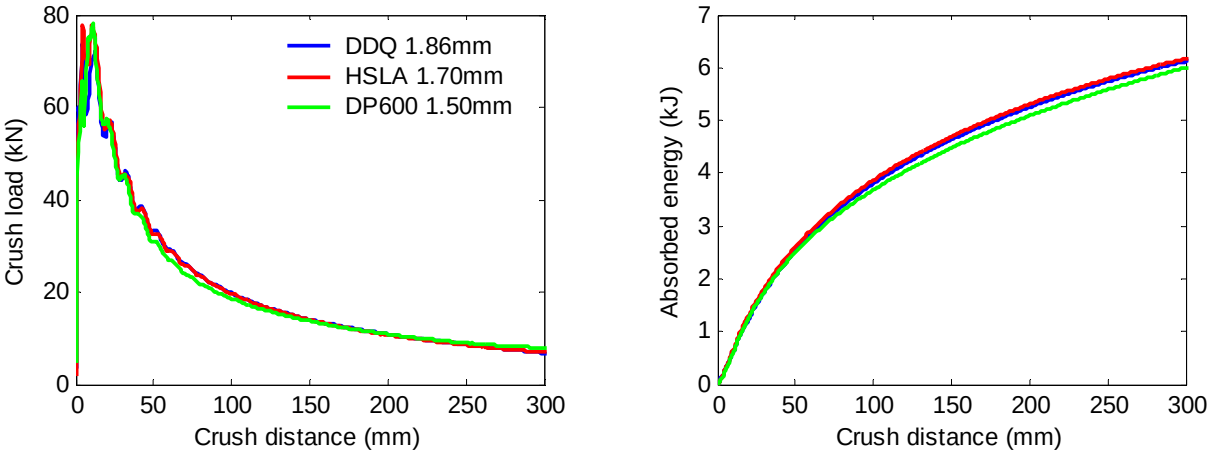

Figure 106: Predicted crash results for hydroformed DDQ 1.86mm, HSLA350 1.70mm, and DP600 1.50mm s-rails bent at an R/D ratio of 2.0

Table 31: Peak load and energy results for hydroformed DDQ 1.86mm, HSLA350 1.70mm, and DP600 1.50mm s-rails bent at an R/D ratio of 2.0

	DDQ 1.86mm	HSLA350 1.70mm	DP600 1.5mm
Peak load (kN)	73.8	77.7 (+5.3%)	78.3 (+6.1%)
Energy @ 300 mm (kJ)	6.12	6.17 (+0.8%)	6.00 (-2.0%)

Chapter 6

Discussion

6.1 Response of tubes to bending and hydroforming

Through experiments and simulations, it has been observed that the tube bending process causes material thinning on the tensile side of the bend and material thickening on the compressive side of the bend. Tensile and compressive strains are observed mainly along the longitudinal direction of the s-rails, with a smaller level of strain apparent in the circumferential direction. The degree of thinning and thickening increases with the bend severity (decreasing R/D ratio), and the measured and predicted strains are commensurate with the levels of thinning and thickening at the various bend severities. Overall, the bending loads (torque, pressure die feed load, mandrel load) increase with bend severity (decreasing R/D ratio). All of these conclusions are in accordance with the findings of Dyment (2004) and Oliveira and Worswick (2005a).

The thickness and strain distributions of the s-rails are only slightly altered by the low-pressure hydroforming process; the most noticeable change after hydroforming occurs in the circumferential bending strains at the four corners of the square cross-section. The thickness and strain distributions of hydroformed s-rails are mainly influenced by the pre-bending operation. The same results have been observed by Oliveira and Worswick (2005a) for aluminum s-rails, suggesting that these findings are independent of the type of material.

The tube bending simulations accurately predict the bending process variables at all three R/D ratios, as well as the post-bending and post-hydroforming strain and thickness distributions. The

predictions of the bending process variables are most accurate for the DP600 s-rails and least accurate for the DDQ s-rails, a trend that is mirrored in the thickness predictions after bending and hydroforming. The inaccuracy of the simulations of the DDQ s-rails is attributed to the use of potentially erroneous friction coefficients in the models, which should be addressed in future work.

Both experiments and simulations show that the bending loads increase significantly with material strength, however, material strength has virtually no effect on the thickness and strain distributions of non-hydroformed and hydroformed s-rails. Increasing the material strength encumbers the calibration stage of the low-pressure hydroforming process since high strength inhibits full forming of the corners of the cross-section; consequently, s-rails made from higher strength materials require higher calibration pressures to fully form in the corner regions. Even if the cross-sectional corners of an s-rail fully conform to the die cavity during the calibration stage, elastic springback can cause the final corner radius to be larger than the desired value, as was the case for the HSLA350 1.8mm s-rails.

The bending loads are shown to increase with material thickness, while the strains and percentage thickness distributions of non-hydroformed and hydroformed s-rails are nearly identical for the two different thicknesses examined in this study. Oliveira and Worswick (2005a) have reached similar conclusions for aluminum alloys of different thickness.

6.2 Effect of alloy selection and forming processes on crash

The numerical crash simulations provide load and energy predictions that are in close accord with the experimental results, as well as accurately predicting the deformed shapes of non-hydroformed and hydroformed s-rails after the crash scenarios. All of the predicted peak loads and absorbed energies are within 10% of the experimental results, however, this value represents a maximum discrepancy and the majority of the predicted crash results are in closer agreement with the measured values (the predictions for the DDQ s-rails are the least accurate).

Summaries of the effects of hydroforming, material strength, R/D ratio, and initial material thickness on the measured values of peak load and absorbed energy are presented in Figure 107 and Figure 108. The most influential factor on the energy absorption of s-rails is the wall thickness of the tube from which the s-rail is manufactured. By increasing the wall thickness of HSLA350 s-rails from 1.53 to 1.86mm (an increase of 22%), the energy absorption increases 47%, while the specific energy absorption (energy absorbed divided by the mass of the structure) increases 22% (a linear relationship within the range of thicknesses considered). Wierzbicki *et al.* (1983) have shown that the energy absorption of an axial crush structure is proportional to the wall thickness of the structure raised to the

power of 5/3; using this relation, it is calculated that an increase in wall thickness from 1.53mm to 1.86mm results in a 38% increase in energy absorption, as opposed to the measured increase of 47%.

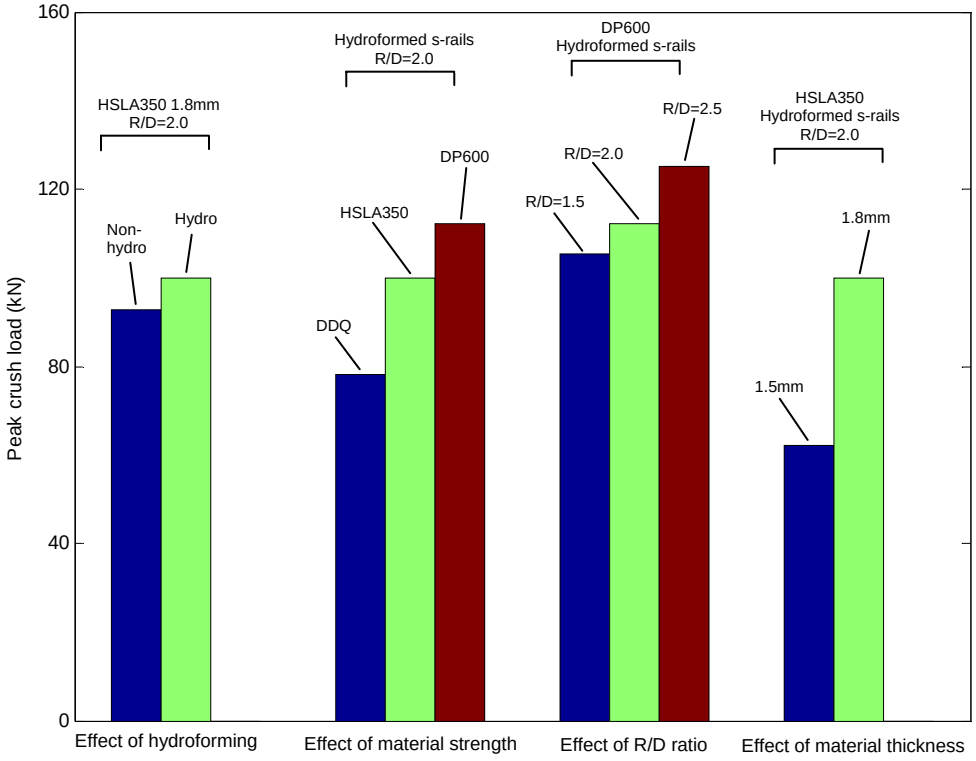

Figure 107: Summary of the effects of various material and forming parameters on the measured peak loads

Material strength is the next most influential factor on the energy absorption of s-rails. By substituting DP600 steel in place of DDQ steel of the same wall thickness (thereby increasing the flow stress of the material by 76% at a plastic strain of 20%) energy absorption increases by 64%, while using HSLA350 as the substitute material (an increase in flow stress of 30% over DDQ at a plastic strain of 20%) yields an increase of 31%. The current results are in agreement with the findings by Wierzbicki *et al.* (1983), who have shown that the energy absorption of axial crush structures is proportional to material strength. Reid (1996a) has also shown that wall thickness has a more influential role on the energy absorption of automotive members than material strength.

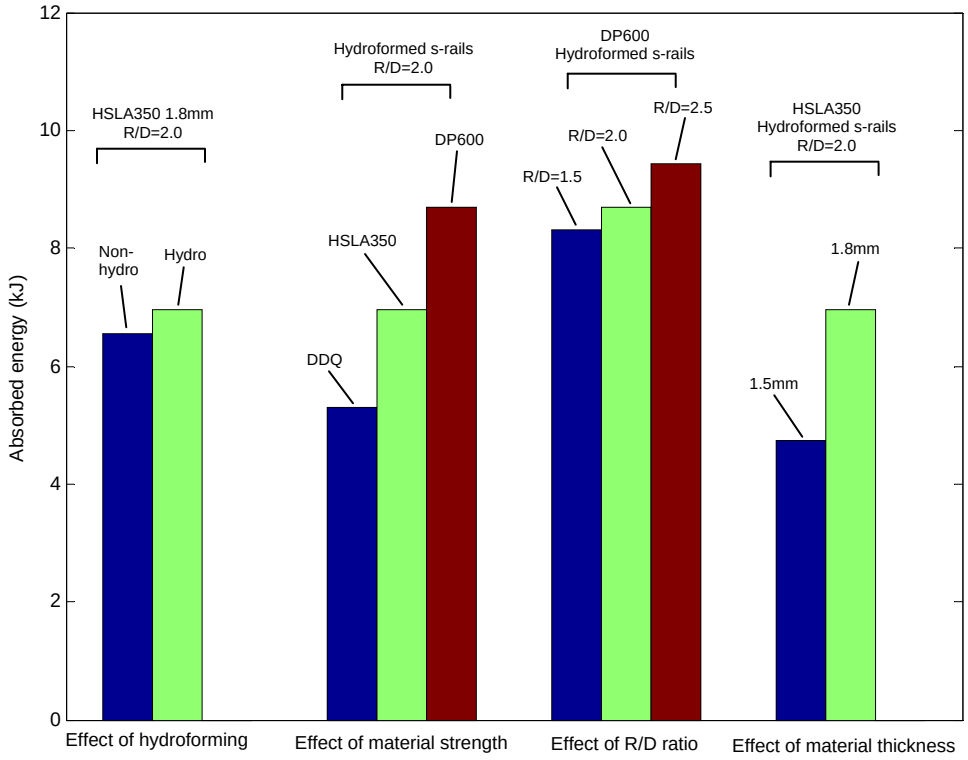

Figure 108: Summary of the effects of various material and forming parameters on the measured values of energy absorption

The reduction in the peak load and energy absorption of s-rails caused by a reduction in the tube wall thickness can be offset by substituting higher strength materials such as DP600 and HSLA350 in place of DDQ, thereby reducing the overall mass of the s-rails without sacrificing the energy absorption capabilities of a vehicle. By parametrically changing the thickness of s-rails in numerical models, it is conservatively estimated that 8.4% and 19.0% mass reductions can be achieved for hydroformed s-rails by substituting thinner gauges of HSLA350 and DP600 in place of DDQ steel while maintaining the same level of energy absorption. Although these values correspond to modest mass reductions of 0.6 kg and 1.4kg for a pair of HSLA350 and DP600 s-rails, respectively, extensive substitution of mild steel with HSLA350 and DP600 steels for components such as roof pillars, bumpers, and body panels can result in appreciable mass savings for the entire body structure of an automobile while maintaining the same level of crash performance. A similar study has been performed by Sperle *et al.* (1984) by substituting DP600 steel in place of mild steel in stamped and welded axial crush structures; a mass savings of 21% was achieved by using the DP600 steel without any loss in energy absorption. While the results quoted by Sperle *et al.* (1984) are in close agreement with those presented herein, the current study is the only one in the literature that has investigated the mass reduction of s-rail structures through the use of advanced high strength steels.

Based on comparisons of the two extreme R/D ratios, bend severity is shown to be the third most dominant feature affecting energy absorption, as shown in Figure 108; by decreasing the bend severity from an R/D ratio of 1.5 to an R/D ratio of 2.5, the energy absorption increases by 14%. Although the degree of work-hardening, which increases the crash loads, is greater for more severe bend radii, the larger moment-arms caused by the smaller bend radii offset this effect and actually reduce the crash loads and energy absorption, a result that is also observed by Oliveira and Worswick (2005b), although the magnitude of this effect is more pronounced in the present study.

Summaries of the factors affecting the predicted values of peak load and energy absorption are presented in Figure 109 and Figure 110, in which the effects of the constitutive models, varying degrees of forming history, impact velocity, and material substitution are presented alongside one-another in order to illustrate the relative influence of all these parameters on the predicted crash results. The energy absorption of steel s-rails is affected to roughly the same degree by material rate-sensitivity, work-hardening due to forming, and cross-sectional change caused by hydroforming. By using three different strain-rate sensitive material models in the numerical simulations along with a strain-rate insensitive model, it is shown that neglecting the strain-rate-induced increases in flow stress lowers the energy absorption of s-rails by 9%; these results are in accord with the findings of numerous researchers examining steel crash structures, such as Huh *et al.* (2002), Peixinho *et al.* (2003), and Tarigopula *et al.* (2006). The predicted numerical results based on a Johnson-Cook, a modified Johnson-Cook, and a Zerilli-Armstrong model are quite similar.

The effects of forming history on energy absorption are shown to be dominated by work-hardening, with minimal effects attributed to material thickness changes and residual stresses, particularly for the current low-pressure hydroformed s-rails. Forming history is also shown to have a more apparent effect on the energy absorption of hydroformed s-rails as opposed to non-hydroformed s-rails. Material thickness changes have minimal influence on the energy absorption of tubular bent and hydroformed s-rails since the effects of thinning on the tensile side of the bend are essentially offset by the effects of thickening on the compressive side of the bend. Dutton *et al.*(1999), Ryou *et al.* (2005), and Oliveira and Worswick (2005b) have all noted that residual stresses have a negligible effect on the energy absorption of automotive structures. Simultaneous omission of work-hardening, thickness changes, and residual stresses from the numerical models results in an 8% reduction in the energy absorption of s-rails.

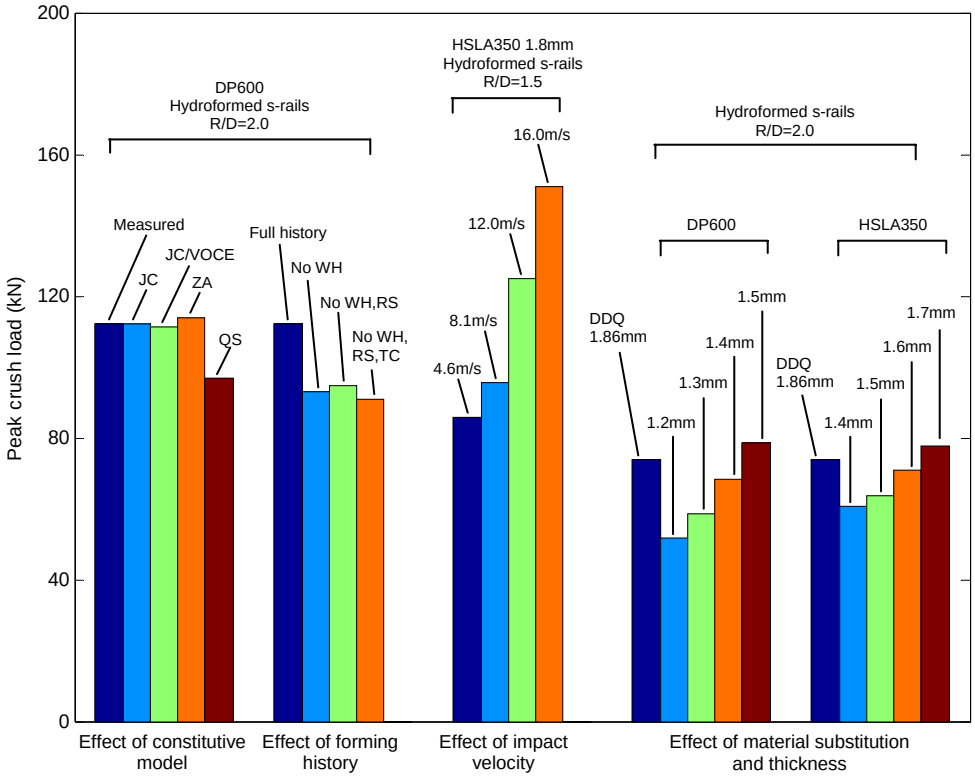

Figure 109: Summary of the effects of different material models, considering forming history, differences in impact velocity, and material substitution on the predicted peak loads

Oliveira and Worswick (2005b) have observed that hydroforming has a significant effect on the energy absorption of aluminum s-rails, with an increase in energy absorption of roughly 20% compared to non-hydroformed s-rails. The effects of hydroforming are not shown to be as significant on the energy absorption of the current steel s-rails, with a maximum increase of only 10% attributed to hydroforming. The reason for this modest increase is that the second polar-moment of inertia for the square cross-section is only 6.5% higher than the that of the non-hydroformed cross-section; furthermore, the low-pressure hydroforming process causes only minor changes in thickness and work-hardening, which serve to increase energy absorption only slightly.

The experimental and numerical studies show that impact velocity has a minor effect on the energy absorption of s-rails, however, there is a significant increase in the peak load as a result of increased velocity. By increasing the velocity from 4.57 m/s up to 16.00 m/s in the numerical models, the peak load is predicted to increase by 76%, while the energy absorption is only predicted to increase by 8%. The dramatic increase in the peak load is attributable almost entirely to inertial effects, a result that is in agreement with the findings of Tarigopula *et al.* (2006), who have shown that at increased impact velocities, inertial effects dominate the force-displacement response of DP800 axial structures.

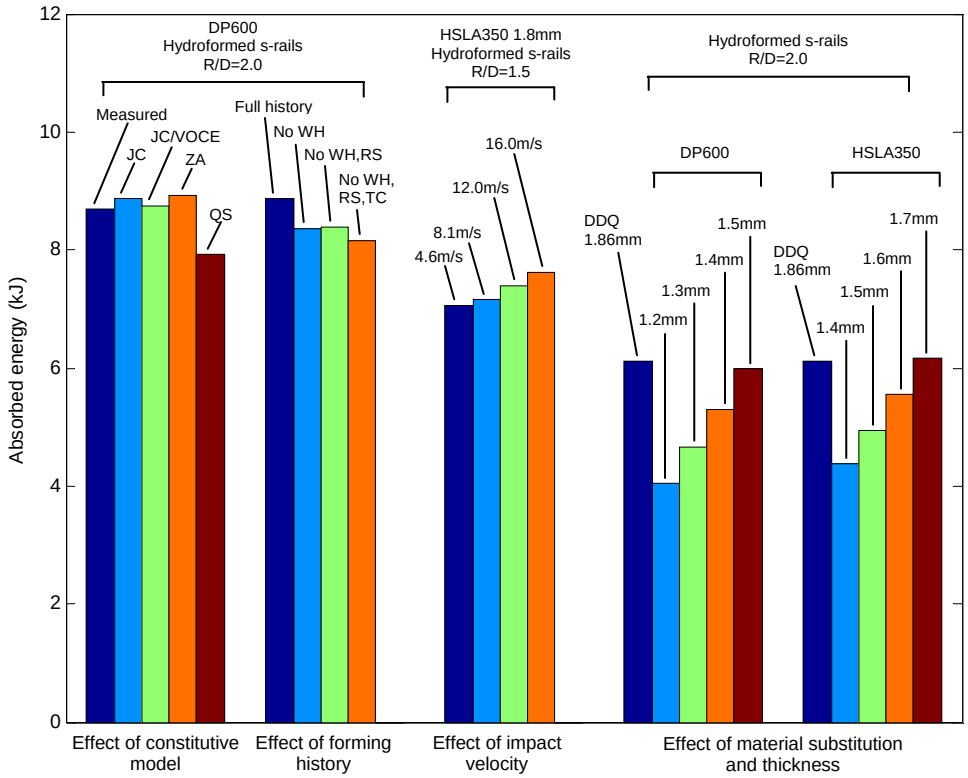

Figure 110: Summary of the effects of different material models, considering forming history, differences in impact velocity, and material substitution on the predicted values of energy absorption

Chapter 7

Conclusions and recommendations

7.1 Conclusions

The following conclusions are reached as a result of this research:

- Bending loads increase with bend severity, material strength, and tube wall thickness
- The thickness distributions of s-rails are only slightly altered by the low-pressure hydroforming process
- Material strength and tube wall thickness have little effect on the post-forming strain and percentage thickness distributions of s-rails
- Numerical simulations provide accurate predictions of bending loads, post-forming thickness and strain distributions, and crash loads
- In order to obtain accurate predictions of crash loads, work hardening and thickness changes due to forming must be considered in the numerical models, and strain-rate-sensitive constitutive models must be used when simulating the impact of steel structures
- Within the confines of the range of variables examined in this study, tube wall thickness is shown to have the greatest effect on the energy absorption of s-rails, followed in order of descending significance by material strength, bend severity, material rate sensitivity, work hardening, and cross-sectional geometry

- Impact velocity has a significant effect on the peak loads during a crash scenario due to inertial effects, however, its effect on energy absorption is minimal for the range of velocities examined in this study
- By replacing DDQ steel with thinner gauges of HSLA350 and DP600 steel, the mass of the s-rail structures considered can be reduced by 8% and 19%, respectively, without any appreciable reduction in energy absorption

7.2 Recommendations

The following is a list of investigations that should be conducted in order to improve and expand upon the current research:

- Twist compression testing of the current hot-rolled DDQ tube stock should be carried out in order to obtain more accurate friction coefficients and improve upon the forming predictions
- The current study should be extended to include materials of even higher strength, such as DP800, DP1000, and TRIP steels, since they present an opportunity for even further mass reduction
- The prospect of additional mass reduction through the use of tailor-welded-tubes and low-density foam filling of s-rails should be investigated
- Since the current study examines s-rails in isolation from other components in a vehicle, a study that investigates the interaction between s-rails and other crash members in an automobile will prove beneficial in forming a full understanding of crash phenomena
- An extension of the current research should also include the examination of cross-sections with a wide range of bending stiffness (ie., non-square cross-sections), since greater energy absorption can be achieved by increasing the bending resistance of s-rail structures

REFERENCES

Abe, K., Nishigaki, H., Ishiyama, S., Ohta, M., Takagi, M., Matsukawa, F., Mizuno, M., 1990. Collapse of thin-walled curved beam with closed-hat section - Part 2: Simulation by plane plastic hinge model. SAE Transactions. 99 (6), 616-624.

Abramowicz, W., 2003. Thin-walled structures as impact energy absorbers. Thin-Walled Structures. 41 (2/3), 91-107.

Abramowicz, W., Jones, N., 1984. Dynamic axial crushing of square tubes. International Journal of Impact Engineering. 2 (2), 179-208.

Ahmetoglu, M., Altan, T., 2000. Tube hydroforming: State-of-the-art and future trends. Journal of Materials Processing Technology. 98 (1), 25-33.

Al-Qureshi, H.A., 1999. Elastic-plastic analysis of tube bending. International Journal of Machine Tools & Manufacture. 39 (1), 87-104.

Alexander, J.M., 1960. An approximate analysis of the collapse of thin cylindrical shells under axial load. Quarterly Journal of Mechanics and Applied Mathematics. 13 (1), 10-15.

Asnafi, N., Nilsson, T., Lassl, G., 2003. Tubular hydroforming of automotive side members with extruded aluminium profiles. Journal of Materials Processing Technology. 142 (1), 93-101.

Bardelcik, A., Worswick, M.J., 2005a. The effect of element formulation on the prediction of boost effects in numerical tube bending. In: Proceedings of Numisheet 2005 Conference, Detroit, MI, USA.

Bardelcik, A., Worswick, M.J., 2005b. Evaluation of load control end-feed in hydroforming of pre-bent DP600 steel tube using the extended stress-based forming limit curve (XSFLC) failure criterion. Journal of Computational and Applied Mechanics, submitted for review.

Brown, J.C., Tidbury, G.H., 1983. Investigation of the collapse of thin-walled rectangular beams in biaxial bending. International Journal of Mechanical Sciences. 25 (9/10), 733-746.

Butterworth, S., 1930. On the theory of filter amplifiers. Wireless Engineer. 7, 536-541.

Cowper, G.R., Symonds, P.S., 1957. Strain-hardening and strain-rate effects in the impact loading of cantilever beams. Technical report No. 28, Division of Applied Mechanics, Brown University, Providence, RI, USA.

Dohmann, F. and Hartl, C., 1997. Tube hydroforming - research and practical application. Journal of Materials Processing Technology. 71 (1), 174-186.

Dohmann, F. and Hartl, C., 2004. Hydroforming-applications of coherent FE-simulations to the development of products and processes. Journal of Materials Processing Technology. 150 (1/2), 18-24.

Dutton, T., Iregbu, S., Sturt, R., Kellicut, A., Cowell, B., Kavikondala, K., 1999. The effect of forming on the crashworthiness of vehicles with hydroformed frame siderails. In: Proceedings of SAE World Congress 1999. SAE paper No. 1999-01-3208.

Dwyer, N., Worswick, M.J., Gholipour, J., Xia, C., Khodayari, G., 2002. Pre-Bending and subsequent hydroforming of tube: Simulation and experiment. In: Proceedings of Numisheet 2002 Conference, 447-452.

Dyment, J.N., 2004. Effect of the bending process on hydroformability of steel tubes. Masters thesis, Department of Mechanical Engineering, University of Waterloo, Waterloo, ON, Canada.

Dyment, J.N., Worswick, M.J., Normani, F., Oliveira, D.A., Khodayari, G., 2003. Effect of endfeed on the strains and thickness during bending and on the subsequent hydroformability of steel tubes. In: Proceedings of International Body Engineering Conference 2003, 717-722.

Gantner, P., Bauer, H., Harrison, D.K., De Silva, A.K.M., 2004. FEA - Simulations of Bending Processes with LS-Dyna. In: Proceedings of 8th International LS-Dyna Users Conference, Troy, MI, USA.

Gao, L., Strano, M., 2004. FEM analysis of tube pre-bending and hydroforming. Journal of Materials Processing Technology. 151 (1/2/3), 294-297.

Geoffroy, J.L., Cambien, I., Jouet, A., 1993. Contribution of high strength steels to the absorption of impact energy. Metallurgia Italiana. 85 (6), 377-382.

Gholipour, J., Worswick, M.J., Oliveira, D.A., Khodayari, G., 2004. Severity of bend and its effect on the subsequent hydroforming process for aluminum alloy tube. In: Proceedings of Numiform 2004 Conference, Columbus, OH, USA, 1089-1094.

Hallquist, J.O., 2003. LS-Dyna – Keyword Users Manual, version 970. Livermore Software Technology Corporation.

Hsu, S.S., Jones, N., 2004. Quasi-static and dynamic axial crushing of thin-walled circular stainless steel, mild steel and aluminum alloy tubes. International Journal of Crashworthiness. 9 (2), 195-217.

Huh, H., Kang, W.J., 2002. Crash-worthiness assessment of thin-walled structures with the high-strength steel sheet. International Journal of Vehicle Design. 30 (1/2), 1-21.

Huh, H., Lim, J.H., Song, J.H., Lee, K.S., Lee, Y.W., Han, S.S., 2003. Crashworthiness assessment of side impact of an auto-body with 60-TRIP steel for side members. International Journal of Automotive Technology. 4 (3), 149-156.

Inoue, K., Mellor, P.B., 1979. Radial-draw bending of stainless steel tube. Journal of Mechanical Working Technology. 3, 151-166.

Johnson, G.R., Cook, W.H., 1983. A constitutive model and data for metals subjected to large strains, high strain rates and high temperatures. In: Proceddings of 7th International Symposium on Ballistics, Hague, Netherlands.

Jones, N., 1998. Some recent developments and future trends in thin-walled sections for structural crashworthiness. Thin-Walled Structures. 32 (1/2/3), 231-233.

Jones, N., 2003. Several phenomena in structural impact and structural crashworthiness. European Journal of Mechanics. 22 (5), 693-707.

Kaufman, M., Gaines, D., Kundrick, K., Liu, S.D., 1998. SAE Special Publications. 1321, 119-122.

Kecman, D., 1983. Bending collapse of rectangular and square section tubes. International Journal of Mechanical Sciences. 25 (9/10), 623-636.

Kellicut, A., Cowell, K., Kavikondala, K., Dutton, T., Iregbu, S., Sturt, R., 1999. Application of the results of forming simulation in crash models. In: Proceedings of Numisheet 1999 Conference, Besancon, France, 509–514.

Kim, H.S., Wierzbicki, T., 2000. Numerical and analytical study on deep biaxial bending collapse of thin-walled beams. International Journal of Mechanical Sciences. 42 (10), 1947-1970.

Kim, H.S., Wierzbicki, T., 2001a. Crush behavior of thin-walled prismatic columns under combined bending and compression. Computers and Structures. 79 (15), 1417-1432.

Kim, H.S., Wierzbicki, T., 2001b. Effect of the cross-sectional shape of hat-type cross-sections on crash resistance of an "S"-frame. Thin-Walled Structures. 39 (7), 535-554.

Kim, H.S., Wierzbicki, T., 2004. Closed-form solution for crushing response of three-dimensional thin-walled "S" frames with rectangular cross-sections. International Journal of Impact Engineering. 30 (1), 87-112.

Koç, M., Altan, T., 2001. Overall review of the tube hydroforming (THF) technology. Journal of Materials Processing Technology. 108 (3), 384-393.

Kulukuru, S., Aue-u-lan, Y., Altan, T., 2002. Determination of flow stress of tubes for hydroforming. Technical report, The Engineering Research Center for Net Shape Manufacturing.

Langrand, B., Geoffroy, P., Petitniot, J.L., Fabis, J., Markiewicz, E., Drazetic, P., 1999. Identification technique of constitutive model parameters for crashworthiness modeling. Aerospace Science and Technology. 4, 215-227.

Lee, E.H., Symonds P.S., 1952. Large plastic deformations of beams under transverse impact. Journal of applied Mechanics. 19 (3), 308-314.

Levy, B.S., Van Tyne, C.J., Stringfield, J.M., 2004. Characterizing steel tube for hydroforming applications. Journal of Materials Processing Technology. 150 (3), 280-289.

Li, Y., Lin, Z., Jiang, A., Chen, G., 2003. Use of high strength steel sheet for lightweight and crashworthy car body. Materials and Design. 24 (3), 177-182.

Mayer, R., 2004. Theoretical effects of hydroforming on crashworthiness of straight sections. ASME Applied Mechanics Division. 255, 591-603.

Mayer, R., 2006a. GM R&D AHSS form and crash impact testing. Internal presentation.

Mayer, R., 2006b. Personal communication.

Meyers, M.A., 1994. Dynamic behavior of materials. John Wiley & Sons, Inc.

Mohanty, O.N., Gope, N., 2004. Advanced steels for the auto body: Developments at Tata steels. Transactions of the Indian Institute of Metals. 57 (4), 367-380.

Morphy, G., 2001. Pressure-sequence and high-pressure hydroforming. Tube and Pipe Journal. 128-135.

Moudlin, P.J., Davidson, R.F., Henninger R.J., 1990. Implementation and assessment of the mechanical-threshold-stress model using the EPIC2 and PINION computer codes. Technical report, Los Alamos National Laboratory.

Ni, C.M., 1976. Impact response of curved box beam-columns with large global and local deformations. In: Proceedings of 14th Structures, Structural Dynamics, and Materials Conference, King of Prussia, PA, USA. AIAA paper No. 73-401.

Normani, F., 2004. Analytical modelling of tube bending and hydroforming. Masters thesis, Department of Mechanical Engineering, University of Waterloo, Waterloo, ON, Canada.

Oliveira, D.A., Worswick, M.J., 2005a. Tube bending and hydroforming of aluminum alloy s-rails. Internal technical report for General Motors of Canada and the Aluminum Technology Center.

Oliveira, D.A., Worswick, M.J., 2005b. Interaction between forming and crashworthiness of aluminum alloy tubes – Crash response of aluminum alloy s-rails. Internal technical report for General Motors of Canada and the Aluminum Technology Center.

Oliveira, D.A., Worswick, M.J., Grantab, R., 2005. Effect of lubricant in mandrel-rotary draw tube bending of steel and aluminum. Canadian Metallurgical Quarterly. 44 (1), 71-78.

Oliveira, D.A., Worswick, M.J., Grantab, R., Williams, B.W., Mayer, R., 2006. Effect of forming process variables on the crashworthiness of aluminum alloy tubes. International Journal of Impact Engineering. 32 (5), 826-846.

Paulsen, F., Welo, T., 1996. Application of numerical simulation in the bending of aluminum-alloy profiles. Journal of Materials Processing Technology. 58 (2/3), 274-285.

Peixinho, N., Jones, N., Pinho, A., 2003. Experimental and numerical study in axial crushing of thin walled sections made of high-strength steels. Journal De Physique. 110, 717-722.

Reid, J.D., 1996a. Towards the understanding of material property influence on automotive crash structures. Thin-Walled Structures. 24 (4), 285-313.

Reid, J.D., 1996b. Crashworthiness of automotive steel midrails: Thickness and material sensitivity. Thin-Walled Structures. 26 (2), 83-103.

Ryou, H., Chung, K., Yoon, J.W., Han, C.S., Youn, J.R., Kang, T.J., 2005. Incorporation of sheet-forming effects in crash simulations using ideal forming theory and hybrid membrane and shell method. Transactions of the ASME - Journal of Manufacturing Science and Engineering. 127 (1), 182-192.

Samek, L., De Cooman, B.C., Van Slycken, J., Verleysen, P., Degrieck, J., 2004. Physical metallurgy of multi-phase steel for improved passenger car crash-worthiness. Steel Research International. 75 (11), 716-723.

Schneider, F., Jones, N., 2004. Impact of thin-walled high-strength steel structural sections. Journal of Automobile Engineering. 218 (2), 131-158.

Shkolnikov, M.B., 2004. Strain Rates in Crashworthiness. In: Proceedings of 8th International LS-Dyna Users Conference, Troy, MI, USA.

Simha, C.H.M., Gholipour, J., Bardelcik, A., Worswick, M.J., 2005. Prediction of necking in tubular hydroforming using an extended stress-based forming limit curve. Transactions of the ASME - Journal of Engineering Materials and Technology, submitted for review.

Simha, C.H.M., 2006. Personal communication.

Singh, H., 2003. Fundamentals of Hydroforming. Society of Manufacturing Engineers.

Sperle, J.O., Lundh, H., 1984. Strength and crash resistance of structural members in high strength dual phase steel sheet. Scandinavian Journal of Metallurgy. 13 (6), 343-351.

Stoughton, T.B., 2000. General forming limit criterion for sheet metal forming. International Journal of Mechanical Sciences. 42 (1), 1-17.

Tang, N.C., 2000. Plastic-deformation analysis in tube bending. International Journal of Pressure Vessels and Piping. 77 (12), 751-759.

Tarigopula, V., Langseth, M., Hopperstad, O.S., Clausen, A.H., 2006. Axial crushing of thin-walled high-strength steel sections. International Journal of Impact Engineering. 32 (5), 847-882.

Thompson, A.C., 2006. High strain rate characterization of AHSS. Masters thesis, Department of Mechanical Engineering, University of Waterloo, Waterloo, ON, Canada.

Trana, K., 2002. Finite element simulation of the tube hydroforming process - Bending, preforming and hydroforming. Journal of Materials Processing Technology. 127 (3), 401-408.

Voce, E., 1948. The relationship between stress and strain for homogeneous deformation. Journal of the institute of metals. 74 (11), 537-562.

Welo, T., Paulsen, F., Brobak, T.J., 1994. The behaviour of thin-walled, aluminum alloy profiles in rotary draw bending - A comparison between numerical and experimental results. Journal of Materials Processing Technology. 45, 173-180.

Wierzbicki, T., Abramowicz, W., 1983. On the crushing mechanics of thin-walled structures. Transactions the ASME - Journal of Applied Mechanics. 50 (4), 727-734.

Williams, B.W., Oliveira, D.A., Worswick, M.J., Mayer, R., 2005. Crashworthiness of high and low pressure hydroformed straight section aluminum tubes. In: Proceedings of SAE World Congress 2005. SAE paper No. 2005-01-0095.

Wu, L., Yu, Y., 1996. Computer simulations of forming automotive structural parts by hydroforming process. In: Proceedings of Numisheet 1996 Conference.

Yang, J.B., Jeon, B.H., Oh, S.I., 2001. The tube bending technology of a hydroforming process for an automotive part. Journal of Materials Processing Technology. 111 (1/2/3), 175-181.

Zerilli, F.J., Armstrong, R.W., 1987. Dislocation-mechanics-based constitutive relations for material dynamics calculations. Journal of Applied Physics. 61 (5), 1816-1825.

Zhan, M., Yang, H., Jiang, Z.Q., Zhao, Z.S., Lin, Y., 2002. A study on a 3D FE simulation method of the NC bending process of thin-walled tube. Journal of Materials Processing Technology. 129 (1/2/3), 273-276.

Zhang, Y., Lai, X., Zhu, P., Wang, W., 2006. Lightweight design of automobile component using high strength steel based on dent resistance. Materials and Design. 27 (1), 64-68.

Zheng, L., Wierzbicki T., 2004. Quasi-static crushing of s-shaped aluminum front rail. International Journal of Crashworthiness. 9 (2), 155-173.